

**University of Alberta**

Measuring Wall Forces in a Slurry Pipeline

by

Suheil El-Sayed

A thesis submitted to the Faculty of Graduate Studies and Research  
in partial fulfillment of the requirements for the degree of

Master of Science  
in  
Engineering Management

Department of Mechanical Engineering

©Suheil El-Sayed  
Fall 2010  
Edmonton, Alberta

Permission is hereby granted to the University of Alberta Libraries to reproduce single copies of this thesis and to lend or sell such copies for private, scholarly or scientific research purposes only. Where the thesis is converted to, or otherwise made available in digital form, the University of Alberta will advise potential users of the thesis of these terms.

The author reserves all other publication and other rights in association with the copyright in the thesis and, except as herein before provided, neither the thesis nor any substantial portion thereof may be printed or otherwise reproduced in any material form whatsoever without the author's prior written permission.

## **Examining Committee**

Dr. Michael Lipsett, Mechanical Engineering

Dr. Amit Kumar, Mechanical Engineering

Dr. Sean Sanders, Chemical and Materials Engineering

## Abstract

Slurry transport is a key material handling technology in a number of industries. Reliability of slurry transport pipelines is a major ongoing problem for operating companies due to unexpected piping failures, even when conservative maintenance strategies are employed. To date, no accurate model has been developed to predict wear rates in slurry transport pipelines, although previous studies have shown that important variables include flow rate, slurry density, and particle size distribution.

This work investigates erosion wear mechanisms causing inner pipe wall wear due to sand slurry flow in a horizontal section of pipe under steady state conditions. A corresponding lumped-parameter erosion wear model is presented based on simplification of the physics of oilsands slurry flow. An apparatus was designed and developed to measure the forces acting on the pipe inner wall to monitor forces related to erosion in a laboratory-scale sand slurry loop, and preliminary results are presented with recommendations for future work.

## Acknowledgements

I want to thank my supervisor Professor Michael Lipsett for his assistance, guidance, and valuable input in this research project. I also want to thank Mr. Justin Duhaime, Mr. Dan Wolfe and Dr. Khaled Obaia from Syncrude Canada Ltd for helping in setting up the experiment.

I will always be indebted to my parents for their unconditional support, financial help, and encouragement. I would also like to thank Ramzi Chehimi, Nasser, Hachem and Sally El-Sayed for their support.

I thank Syncrude Canada Ltd., the Natural Sciences and Engineering Research Council of Canada, and Alberta Research Council for funding of this research project.

I truly wish that this work is a starting point for new developments and knowledge to improve oil sands hydrotransport pipeline reliability and performance.

# TABLE OF CONTENTS

<b><u>1</u></b>	<b><u>INTRODUCTION</u></b>	<b>1</b>
1.1.	OILSANDS	1
1.2.	OIL SANDS HYDROTRANSPORT	2
1.3.	OILSANDS HYDROTRANSPORT PIPELINE RELIABILITY	3
1.4.	PROBLEM DEFINITION	4
1.5.	SOLUTION OBJECTIVES	6
1.6.	SOLUTION METHODOLOGY	7
1.7.	THESIS OUTLINE	8
<b><u>2</u></b>	<b><u>LITERATURE REVIEW</u></b>	<b>9</b>
2.1.	HETEROGENEOUS SLURRY FLOW	9
2.2.	HETEROGENEOUS SLURRY FLOW PRESSURE DROP PREDICTIONS USING TWO-LAYER MODEL	11
2.3.	WEAR MECHANISMS AFFECTING SLURRY PIPELINES	16
2.4.	WEAR PROFILE IN OILSANDS HYDROTRANSPORT PIPELINES	19
2.5.	WEAR PROFILE IN SAND SLURRY PIPELINES	21
2.6.	EROSION WEAR MATERIAL RANKING TESTS	23
2.7.	MODELING AND SIMULATION	27
2.8.	WEAR MODELING IN SLURRY PIPELINE	28
2.9.	MEASUREMENT OF PIPE STRESS IN SINGLE PHASE FLOW	33
2.10.	FLOATING ELEMENT SENSOR	34
<b><u>3</u></b>	<b><u>SAND SLURRY EROSION WEAR MODEL DEVELOPMENT</u></b>	<b>37</b>
3.1.	OILSANDS FLOW MODELING AND SIMULATION	37
3.2.	SAND SLURRY EROSION WEAR MODEL	38
3.3.	MODEL VALIDATION ISSUES	45
3.4.	EXPERIMENTAL SYSTEM AND TESTING METHODOLOGY	51
3.5.	FLOATING ELEMENT COMPONENTS DESCRIPTION	52

3.6. HYDROSTATIC TEST	68
3.7. CALIBRATION	68
<b><u>4 FLOATING ELEMENT OUTPUT MEASUREMENTS AND INTERPRETATIONS</u></b>	<b><u>72</u></b>
4.1. PRELIMINARY TEST SETUP	72
4.2. COMMISSIONING	75
4.3. PRELIMINARY TEST PROCEDURE	78
4.3.1. TEST #1	78
4.3.2. TEST #2	79
4.3.3. TEST #3	79
4.4. PRELIMINARY TESTING RESULTS	83
4.4.1. OBSERVATIONS AND SUMMARY OF RESULTS	83
4.4.2. COMPARISON WITH THEORETICAL RESULTS	90
4.4.3. REPEATABILITY RESULTS	95
4.4.4. SIGNAL PROCESSING	96
4.5. FUTURE DESIGN MODIFICATIONS	101
4.6. CONSIDERATIONS FOR MONITORING WEAR	103
4.7. CONSIDERATIONS FOR SCALE-UP TO LARGER PIPING SYSTEMS	104
<b><u>5 CONCLUSIONS AND RECOMMENDATIONS FOR FUTURE WORK</u></b>	<b><u>107</u></b>
5.1. CONCLUSIONS	107
5.2. RECOMMENDATIONS FOR FUTURE WORK	108
<b><u>BIBLIOGRAPHY</u></b>	<b><u>114</u></b>
<b><u>APPENDIX</u></b>	<b><u>118</u></b>

# List of Tables

Table 1. Floating element sensor calibration results .....	70
Table 2. Tests Summary .....	83
Table 3. Floating element sensor shear bridge post test calibration results .....	95

# List of Figures

Figure 1. Concentration profile and particle distribution at different heterogeneous slurry flow regimes .....	10
Figure 2. Two-layer model concentration and velocity profiles .....	13
Figure 3. Two-layer model schematic .....	13
Figure 4. Wear profile in a straight oilsands hydrotransport pipeline section .....	20
Figure 5. Physical system model of oilsands slurry pipeline section .....	37
Figure 6. Simplified physical model of sand slurry pipeline section .....	40
Figure 7. Simplified physical model of sand slurry pipeline section.....	41
Figure 8. Simplified wear damage model of sand slurry pipeline section .....	42
Figure 9. Simplified physical model of sand slurry pipeline section for fully suspended flow .....	45
Figure 10. Parametric representation of sand slurry flow and erosion damage for fully suspended flow .....	46
Figure 11. Parametric representation of sand slurry flow and erosion damage due to sliding bed .....	49
Figure 12. A simplified schematic illustration of the ASTM G65 test. ....	49
Figure 13. Overview of the floating element sensor assembly .....	52
Figure 14. Cross section view of the floating element sensor assembly .....	53
Figure 15. Photo of the floating element assembly.....	54
Figure 16. Alignment of wear sample with pipe wall.....	55
Figure 17. Photo of wear sample holder assembly.....	57
Figure 18. Flush water supply connection to the floating element assembly .....	59
Figure 19. A cross-sectional view of the clear section and floating element pipe assembly .....	60
Figure 20. Photo of clear section .....	61
Figure 21. Illustration of the strain gauge setup of the floating element sensor .....	62

Figure 22. Side view of axial bridge strain gauge configuration .....	63
Figure 23. Front view of axial bridge strain gauge configuration .....	64
Figure 24. Friction bridge strain gauge configuration .....	66
Figure 25. Diagram showing forces applied to wear sample surface during calibration ..	70
Figure 26. Syncrude slurry loop process diagram (not to scale) .....	73
Figure 27. Photo of Syncrude research slurry loop main components .....	75
Figure 28. Photo of floating element assembly and clear section at Syncrude Research	76
Figure 29. Needle valve flow curves for corresponding back pressure in psig.....	82
Figure 30. Plot of measured water friction force versus bulk velocity.....	84
Figure 31. Plot of measured water axial force versus bulk velocity .....	85
Figure 32. Plot of measured slurry friction force versus bulk velocity.....	87
Figure 33. Plot of measured slurry axial force versus bulk velocity .....	88
Figure 34. Measured discharge pressure versus velocity .....	90
Figure 35. Theoretical and measured water friction force versus flow rate .....	91
Figure 36. Theoretical and measured slurry friction force versus flow rate .....	92
Figure 37. Friction force versus time during repeatability test #2 .....	95
Figure 38. Axial force versus time during repeatability test #2 .....	96
Figure 39. A photo of the frequency test setup .....	98
Figure 40. Friction bridge power spectral density for slurry flow at 190 USGPM at t = 40 to 46 sec.....	99
Figure 41. Sample axial bridge power spectral density plot for both slurry and water flows at 190 USGPM and 207 USGPM respectively .....	100
Figure 42. Sample friction bridge power spectral density plot for both slurry and water flows at 190 USGPM and 207 USGPM respectively .....	101
Figure 43. Recommended floating wear sample geometry .....	111

# 1 Introduction

The importance and contribution of oilsands to the Canadian economy especially in the province of Alberta is substantial. Investments made in the oilsands industry impact other industry sectors, and it is projected that 42,000 full time positions between the year 2000 and 2020 will be created due to oilsands activity [1]. It is also estimated that \$91 billion were invested in the oilsands industry from the years 1999 to 2009 [1].

Pipeline transport of ore and tailings is a key process step in surface-based oilsands operations. Oilsands hydrotransport pipelines have ongoing reliability challenges, where reliability of a system or component is defined as “the ability of an item (product, system, etc.) to operate under designated operating conditions for a designated period of time or number of cycles” [2]. Premature failures of pipelines result in lower production rates, increased downtime, and can put personnel and the environment at risk. One of the main problems that significantly affect and reduce hydrotransport pipeline reliability is inner wall wear due to oilsands slurry flow.

## 1.1. Oilsands

Oilsands are a mixture of bitumen, silica sand, water and clay. Oilsands are abundant in northern Alberta mainly in the Fort McMurray area and contain between 1% and 20% bitumen depending on the ore body quality [3]. Alberta oilsands are one of the world’s largest oil reserves with proven reserves of 170.4 billion barrels of crude bitumen [1]. Bitumen found in the oilsands matrix is highly viscous, with viscosity at around  $10^6$  mPa.s at 10 °C [4]. Alberta oilsands have great economic potential especially since

estimates today show that Alberta ranks second to Saudi Arabia in proven oil reserves [1].

Oilsands reserves can be divided into two categories: shallow reserves and deep reserves. Shallow oilsands reserves comprise only 20% of the total oilsands reserves, and they are present approximately 100m below the earth surface [5]. Oilsands deposits much deeper than 100m below earth surface are considered deep oilsands deposits (too deep for economical surface mining) [5].

One technique for extracting bitumen from surface deposits employs shovels and trucks to mine the oilsands deposit [6]. Large scale shovels such as the P&H 4100 series especially designed to mine large quantities about 115 tons of oilsands per load are used to load large off-road haul trucks with up to 400 tonne, which carry ore from the mining point to a crusher, where the oilsands are blended, crushed, and mixed with treated water [7].

## 1.2. Oil Sands Hydrotransport

Oilsands mining operations in Alberta are considered Canada's largest mining operations and a typical oilsands mining operation has around 90 km of slurry pipelines [7]. About 6000 to 10,000 tonnes of oilsands are mined per hour at Syncrude's Aurora mine [7]. Large off-road haul trucks transport the mined oilsands for crushing, after which the oil sand is mixed with hot water and aerated in order to help bitumen escape the oilsands matrix [7]. The resulting slurry is then transported via large pipelines over 700mm in diameter to the extraction plant [7]. At Syncrude's Aurora mine, the hydrotransport pipeline length is approximately 5 km [4]

During the transportation of oilsands-water slurry from the mine to the extraction plant via hydrotransport pipelines, preliminary conditioning of the slurry takes place and a fraction of bitumen escapes the oilsands matrix [7]. Transported oilsands slurries are fairly concentrated (above 35% solids by volume) with the sand particle size diameter ranging from 0.18 mm to 0.3 mm transported at velocities above the deposition velocity, which is between 3 m/s and 5.5 m/s for typical process conditions [4].

In the extraction facility, the oilsands slurry enters a primary separation vessel (PSV) where bitumen froth floats to the top and sand settles to the bottom of the vessel [8]. In the middle of the PSV, a mixture of water, fine sand, and bitumen exists as middlings, which goes through an additional separation step [8]. The bitumen froth extracted then goes through deaeration and froth treatment with diluents added to aid in removing water and solids. The bitumen goes through diluent recovery to remove hydrocarbon solvent used in froth treatment. Dry bitumen product is then upgraded to a light, synthetic crude oil suitable for downstream refining.

### 1.3. Oilsands Hydrotransport Pipeline Reliability

Wear of a component reduces its reliability and eventually leads to failure. The expected component lifetime should be estimated and maintenance tasks should be scheduled such that the probability of unexpected failures is reduced, when the consequences of unexpected failures would be significant and thus warrant attention.

To date, conservative maintenance strategies are employed by operating oil companies in order to reduce downtime due to unexpected pipeline failure. Lack of understanding of the specific wear mechanisms causing wear (thereby affecting slurry pipeline reliability) is another reason for

employing a conservative maintenance strategy [9]. Failure mechanisms in oilsands slurry lines are complex, and not simply due to abrasive wear [10]. As a result, hydrotransport pipeline operating costs are increased substantially due to premature retirement of pipeline sections. Despite the conservative maintenance strategies employed, unexpected pipeline failures still occur [9]. Condition-based maintenance techniques are not used directly to monitor pipeline wear and assess pipeline integrity [11]. Instead, the condition of hydrotransport pipelines is reviewed mainly based on experience. Condition-based maintenance decisions can ensure that system reliability is maintained at a high level, and employing flow monitoring and pipeline wear monitoring techniques help engineers to better schedule maintenance activities. Preventative and condition based maintenance strategies not only decrease maintenance costs but also ensure high pipeline reliability, provided that the condition is monitored appropriately and maintenance actions are done before failure occurs.

For this reason a model to predict pipeline wear rates based on operating conditions would be highly beneficial for an operating company. A wear model would reduce the requirement for pipeline inspections, allow improved maintenance planning, and lead to utilizing the piping system more effectively, and as a result reduce maintenance costs.

#### 1.4. Problem Definition

Proper scheduling of maintenance activities, an important function of a successful maintenance program, reduces operating costs and increases work efficiency [12]. In order to properly schedule pipeline maintenance tasks such as pipe replacement or rotation, knowledge of the expected condition and wear profile of the pipeline is needed especially at high wear rate locations. Ideally, maintenance is done just before the end of

component life. The lack of pipeline wear knowledge results in excessively conservative scheduling of maintenance tasks, because to prevent failures a short expected life is used when the component life has uncertainty. Scheduling maintenance tasks conservatively results in increased operating costs and lowers pipe utilization. On the other hand, delaying of critical maintenance tasks increases the occurrence of unexpected failures.

Maintenance activities such as pipe rotation and replacement are performed early before failure is expected based on previous operating experience; however, oilsands hydrotransport pipelines operating conditions are highly variable. As mining companies increase oilsands flow rates pumped via hydrotransport pipelines, pipeline wear rates vary correspondingly. As a result, equipment maintenance schedule must be updated continually to reflect new operating conditions.

Unfortunately, there is no accurate way to predict the wear profile in hydrotransport pipeline. Wear prediction in a hydrotransport pipeline is generally performed using a linear correlation based on the number of operating hours and maximum expected wear in the pipe based on previous experience [7]. Damage wear rates are found to differ depending on their location in the pipeline [4]. For example, pipe bends experience between 2 to 5 times higher damage rates than a straight pipe located away from a bend [4]. Also, the nature of the damage is different depending on operating conditions and ore quality [4].

Reactive maintenance for critical components is more expensive than preventive maintenance due to increased response time and increased labor costs. Therefore, it is important for a maintenance engineer to develop a model to predict the useful lifetime of critical components such as a hydrotransport pipeline in the case of oilsands mining industry. On

the other hand, wear mechanisms acting in a hydrotransport pipeline are very complex since erosion, corrosion, and erosion/corrosion all take place.

Existing ASTM type wear tests have been used to rank materials resistance to wear due to slurry flow. The disadvantages of using the existing ASTM wear ranking tests are that they simulate different wear processes than those experienced by the pipe wall due to slurry flow. Moreover, the contribution of corrosion and the combined erosion-corrosion are included in the total wear rate experienced by the wear specimen. The existing tests are not suitable for erosion wear prediction. On the other hand, some of these tests can be modified to simulate erosion wear mechanisms due to slurry flow.

## 1.5. Solution Objectives

At Syncrude's Aurora mine, hydrotransport pipelines are 737 mm in diameter and transport about 10,000 tonnes of oilsands per hour in each line [4]. Replication of site operating conditions using the same oilsands slurry mixture in a 737 mm diameter pipeline under controlled laboratory conditions is not possible due to cost and space limitations. Moreover, oilsands slurry mixture particle size distribution and bitumen content is highly variable depending on the ore body quality and mining location. This variability is exacerbated by the presence of oversized particles (also known as lumps).

Due to the complexity of wear experienced by oilsands hydrotransport pipelines, the scope of this study is limited to studying the effects of erosion wear due to sand slurry flow in a straight section of pipe under steady-state operating conditions and neglecting corrosion and erosion-

corrosion effects. Early simplification of the problem definition is necessary to be able to validate the results obtained. Once the results are validated for a simplified case, an oilsand erosion model can be developed and tested in future studies with more realistic conditions. This study is a first step towards developing a realistic oilsands hydrotransport wear model that will include the contribution of corrosion and erosion/corrosion wear mechanisms.

One objective of this thesis work is to introduce a simplified erosion wear parametric model based on the physics of sand slurry flow in a straight section of pipe at steady-state conditions. In this parametric representation, the erosion wear contribution of impact and abrasion wear mechanisms is differentiated around the pipe circumference. Another objective of this work is to develop an apparatus to measure the forces experienced by pipe inner wall during fully suspended heterogeneous slurry flow.

## 1.6. Solution Methodology

This work employs a sand slurry physics-based flow model for slurry flow at steady state conditions in a straight section of pipe, modified for describing wear. A parametric erosion wear model was then formulated to help improve the understanding of the relationship between flow conditions and erosion wear rates. Forces on the wall due to particle interactions were noted to be important for understanding the damage mechanism. A measurement device was developed based on a floating element to measure the forces on the wall of a pipe. Laboratory scale tests were conducted using the apparatus developed to measure forces experienced by inner pipe wall due to fully suspended sand slurry flow in a section of a two-inch pipe loop at Syncrude's research facility.

The intent was to use a measurement technique to measure forces during slurry flow with sliding bed, although testing was not done under these conditions due to limitations on the range of operation of the loop.

Measuring forces experienced by the pipe wall during slurry flow is one step toward the specification of the parameters of the presented parametric erosion wear model, to understand better the nature of forces causing damage in a slurry pipe.

## 1.7. Thesis Outline

In Chapter 2, a review of the literature and an understanding of the state of the art in the area of slurry pipeline wear prediction are presented in addition to the limitations of the current understandings and studies. Chapter 3 describes a parametric wear model developed for sands slurry pipeline wear and the experimental system that was designed to characterize part of the wear model. Chapter 4 includes a description of the test plan and results with interpretations. Finally, Chapter 5 concludes the findings of this thesis work and gives some recommendations for future work.

## 2 Literature Review

Two types of slurry flow can exist in a straight section of pipe: homogeneous slurry and heterogeneous slurry. Homogeneous slurry flow exists when the solid particles are small and almost always flocculated with strong colloidal forces between the solid particles [13]. Heterogeneous slurry flow occurs when the solid particles are large and sink to the bottom of a container filled with the carrier fluid due to the particles' own weight [13].

Several flow regimes can exist in a horizontal section of pipe with heterogeneous slurry flow depending on the slurry concentration, particle size distribution, volume flow rate, carrier fluid density, and volume concentration of fines in the flow [14]. The two-layer model is a semi-mechanistic model used to predict pressure drop of heterogeneous slurry flow in a horizontal section of pipe at steady-state conditions [13].

### 2.1. Heterogeneous Slurry Flow

Heterogeneous slurries are defined as settling slurries, as they have a tendency to settle to the bottom of the pipe under no flow condition [15]. Homogeneous or non-settling slurries can be treated as pseudo fluids or non-Newtonian fluids. Some non-Newtonian flow models have been developed, such as the Bingham model, which calculate wall shear stress for particular slurry properties and mixture velocities [14]. Solid particles in heterogeneous slurries are not equally distributed within the slurry flow and a continuum model cannot be produced to describe the slurry as a pseudo-fluid with rheological characteristics such as viscosity and yield stress [13].

Depending on the mixture flow velocity, several flow regimes can exist in heterogeneous slurry flow as shown in Figure 1. Deposition velocity can be defined as the velocity above which accumulation of particles along the bottom of the pipe is prevented [13]. No flow or plugged pipe condition can occur if the mixture flow velocity is below the deposition velocity [13]. As the mixture velocity is increased, the flow regime changes from flow with a stationary bed to flow with a moving bed and then to fully suspended flow regime [13]. In a moving bed flow regime, the slurry velocity is higher than the deposition velocity. The velocity is high enough to cause the bed layer in the bottom of the pipe to move and slide against the pipe wall; but the velocity is not high enough to suspend all of the solid particles present in the flow [13]. As the velocity of the slurry flow increases, more slurry particles become suspended by carrier fluid turbulence. In all of the flow regimes mentioned, an asymmetric concentration and particle velocity profile exists in the pipe flow [13]. As the slurry bulk velocity is increased even further, all particles become fully suspended by carrier fluid turbulence and as a result a homogeneous flow regime develops [13]. In a homogeneous flow regime, a symmetric particle concentration and velocity profile exists [13].

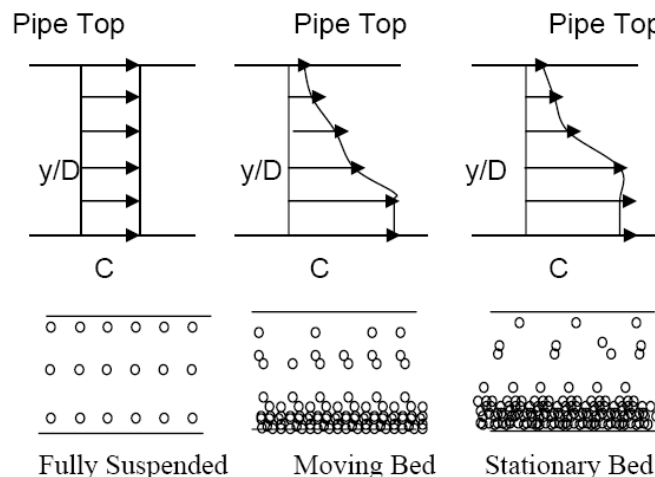


**Figure 1. Concentration profile and particle distribution at different heterogeneous slurry flow regimes [13]**

As the mixture velocity is increased, the pressure drop in a straight section of pipe also increases. Since heterogeneous slurries are found in many industrial applications, a big interest has arisen to be able to predict pressure drops in heterogeneous slurry pipelines [13].

## 2.2. Heterogeneous Slurry Flow Pressure Drop Predictions Using Two-Layer Model

The first attempt to produce a mechanistic flow model to predict pressure drop of heterogeneous slurry flows was presented as early as 1955 by D.M. Newitt [16]. Gillies et al. also added improvements to the earlier version of the mechanistic heterogeneous slurry model developed by K.C. Wilson in 1970 and 1972 [16]. In the earlier version of Wilson's model, the model consisted of two layers in which the top layer consisted of the carrier fluid only and the bottom layer was made up of particles sliding against the pipe wall [16].

In general, a fraction of the particles in the slurry contributes to the contact load due to particles sliding against the pipe wall, and the other fraction is carried by fluid turbulence and only contributes to kinematic friction. K.C. Wilson used this model to predict the deposition velocities of slurries [16]. A nomographic chart was produced by K.C. Wilson in 1979 which was used to predict the settling velocity of heterogeneous slurries [13]. This chart was considered to be accurate at slurry flow temperatures below 30C [16].

Additional improvements to the two-layer model were made by Gillies and Shook [17]. In the improved two-layer model, the carrier fluid consists of the liquid medium plus fine particles such as clays of diameter size smaller than 74 microns, because these particles are non-settling in water [17].

Particles of diameters over 74 microns in size are considered coarse because they contribute to friction losses through mechanisms that are not fluid-like. In the improved two-layer model, the total in situ concentration by volume ( $C_r$ ) is equal to the total solid particle volume fraction divided by the total volume of the pipe [17]. The viscosity of the fluid, which is made of the carrier fluid (water and fines), can be easily measured using a viscometer.

According to the improved two-layer model, friction losses due to slurry flow in a straight section of pipe are caused by kinematic friction and Coulombic friction [10]. Kinematic friction is friction between the carrier fluid and the pipe wall plus an additional friction component due to suspended solid particles [17]. Kinematic friction also includes a term to account for the near wall tempering effect known as near wall lift [17]. The near wall effect reduces the friction between solid particles above a certain size due to the presence of a thin viscous sub-layer developed near the pipe wall [17]. The tempering effect of the near wall lift is increased with increasing particle diameter and increasing carrier fluid velocity [10].

Coulombic friction results from the particles unsupported by carrier fluid turbulence and supported by the inner pipe wall [10]. These particles are the heavier solid particles in the mixture, and a fraction of the particles immersed weight is directly supported by the pipe wall [10].

In the top layer, particles are fully suspended by mixing turbulence and as a result kinematic friction exists only [17]. In the bottom layer, a fraction of the particles is fully suspended by turbulence and the remaining fraction of particles is supported through contact by pipe wall [17]. As a result, both kinematic and Coulombic friction exist in the bottom layer. An idealized concentration and velocity profile used to develop the two-layer model is shown in Figure 2.

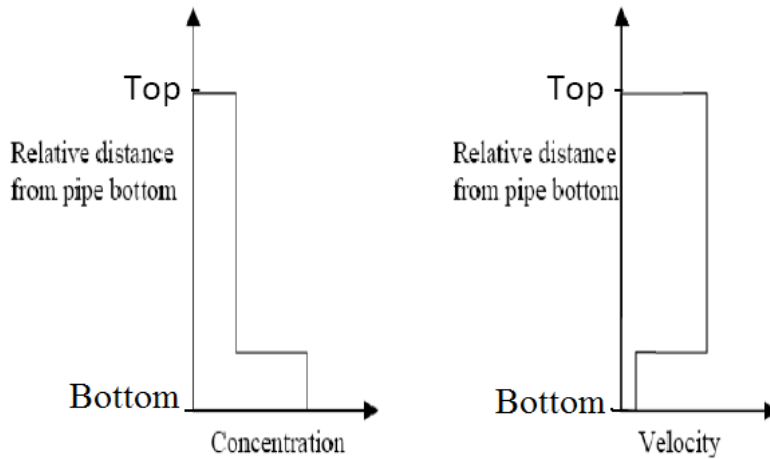


**Figure 2. Two-layer model concentration and velocity profiles [17]**

Flow rate, energy balance and concentration equations have been formulated based on the two-layer model and which can be solved simultaneously to predict the pressure loss due to slurry flow in a horizontal straight section of pipe [16].

The following equations have been formulated for steady state heterogeneous flow in a pipe of constant diameter based on the improved two-layer model:

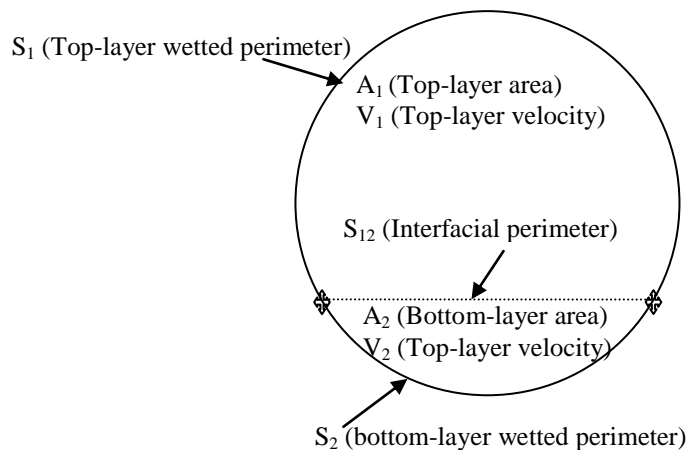


**Figure 3. Two-layer model schematic [17]**

The top layer force balance equation is

$$\frac{dP}{dz} + \rho_1 g \frac{dh}{dz} + \frac{\tau_{1k} S_1 + \tau_{12} S_{12}}{A_1} = 0; \quad (1)$$

The bottom layer force balance equation is

$$\frac{dP}{dz} + \rho_2 g \frac{dh}{dz} + \frac{\tau_{2k} S_2 - \tau_{12} S_{12} + \int \tau_{2c} dS_2}{A_2} = 0; \quad (2)$$

The mixture flow rate equation is

$$AV = A_1 V_1 + A_2 V_2; \quad (3)$$

The solids flow rate equation is

$$C_{vd} AV = V_1 A_1 V_1 + C_2 A_2 V_2; \quad (4)$$

The total solids concentration equation is

$$C_r A = C_1 A_1 + C_2 A_2; \quad (5)$$

The contact load solid concentration equation is

$$C_c A = (C_2 - C_1) A_2; \quad (6)$$

where,

$C_r$  is the resident solids concentration

$C_c$  is the contact solids concentration

$C_{vd}$  is the delivered solids concentration

$\tau_{2k}$  is the bottom layer kinematic stress term

$\tau_{1k}$  is the top layer kinematic stress term

$\tau_{12}$  is the interfacial stress term between the top layer and the bottom layer

$\int \tau_{2c} dS_2$  is the Coulombic friction term and can be evaluated by integrating the normal stress along  $S_2$

The assumptions in this formulation are the following [16, 17]:

- Steady state slurry flow conditions such as pressure, temperature, particle size distribution and flow rate
- Suspending medium is a Newtonian fluid
- Particles are evenly shaped with narrow size distribution
- Horizontal pipe flow in which local slip between particles and fluid does not occur
- Coulombic friction is not affected by near wall lift
- Constant pipe diameter
- Turbulent flow
- Constant friction factor used for calculating Coulombic friction.

The above equations can be solved by specifying the bulk slurry velocity, pipe cross-sectional area, and in-situ concentration. A value of the bottom layer concentration can be determined from the concentration profile. The concentration at different horizontal positions in the pipe can be measured using a nuclear densitometer. Assuming that the concentration is constant at each horizontal position within the pipe, a concentration profile can be constructed and the insitu concentration calculated [18]. The contact load concentration can be determined from the in-situ concentration by knowing the terminal velocity of the sand and velocity profile using a proposed equation developed by Gillies, Shook and, Xu [19].

The two-layer model equations provided are too complicated to solve by hand; but, a computer program can be used to solve these equations iteratively. At high solids concentrations, particle-particle interactions become even more significant and pressure drop in the pipe increases

substantially. Damage mechanisms such as bed sliding abrasion and random particle impact with pipe inner wall will still exist in the pipe. On the other hand, the contribution of each of the wear mechanisms to the pipe erosion wear will be affected. The significance of Coulombic friction increases, because more unsuspended particles will exist in the flow. Coulombic friction may hinder the affect of kinematic friction in the bottom layer of flow due to increased thickness of the moving bed.

### 2.3. Wear Mechanisms affecting Slurry Pipelines

Wear in slurry pipelines is a complex and complicated process as it is extremely difficult to isolate the wear processes occurring in a slurry pipeline. The main cause of wear in slurry applications is due to erosion by solids. Metal loss due to corrosion plays a minor role, especially in a fresh water slurry application [10].

On the other hand, the combined corrosion-erosion synergy is also important and can be more critical than the individual wear contribution due to erosion or corrosion, since slurry particles erode the inner pipe wall exposing new pipe material to corrosion [10]. The corrosion process is accelerated due to the presence of the fresh surface. It is important to be able to quantify the individual contribution of erosion, corrosion, and corrosion-erosion to the overall wear rate in the slurry pipe [10]. It is difficult to isolate the contribution of corrosion from the overall wear in the slurry pipe due to the presence of erosion wear, which is usually more dominant and severe [10].

Fewer experiments have been conducted for understanding erosion in slurry pipe flow compared to heterogeneous slurry pressure drop predictions in pipe due to the slow nature of the erosion process and the

cost of collecting wear data [20]. As a result, some companies have started to collect erosion or wear data; however, the accuracy of the data collected is to be questioned depending on the method used in collecting the data, the frequency of data collection, and the recording of flow conditions as the measurements are taken [20].

For dense slurries, the particle-particle interaction is significant and affects the slurry flow profile. The first mechanism affecting dense slurry flow pipe erosion is referred to as sliding erosion and the second mechanism is particle impact erosion. Particles randomly impact on the pipe wall due to turbulence and due to particle-particle interaction, causing cutting [20]. Particle impact erosion is caused by impact of solid particles at angles with the walls of the pipe. Erosion of the pipe starts to occur if the impact energy transferred to the wall is above a critical value [21]. For mild steel, two forms of impact erosion occur: deformation and cutting [10]. The dominance of one erosion mechanism over the other is dependent on the angle of impact.

Erosion of the material is an accumulative process where cutting and deformation occurs over a period of time. The length of this period of time is dependent on the shape of the particle, pipe material characteristics, density of particles, concentration of particles, hardness of the particles, size of particles, mean angle of impact, and the mean velocity of impacting particles [10]. In a straight section of pipe, turbulence causes the slurry particles to move out of the flow streamlines and randomly impact on the pipe inner wall. This flow process occurs more often if the geometry of the pipe is not straight such as in the case of an elbow. Wear caused by particle impact erosion is in general discontinuous and looks like frost [10].

Another cause of erosion is sliding abrasion, which occurs mainly at the bottom of the pipe due to the normal weight of the particles [20]. Abrasion

occurs due to bed immersed weight and as a result part of the pipe erodes when the bed slides over the pipe.

Unsuspected particles supported by the pipe inner wall at the bottom section of the pipe cause sliding erosion of the pipe wall. Heavier solid particles that cannot be fully suspended by carrier fluid turbulence create a moving bed in the bottom of the pipe. The weight of the particles in the bed flow is carried directly by the pipe material. As the particles move or slide along the bottom of the pipe, erosion of pipe material occurs due to particle-wall interaction. This erosion mechanism is dominant in slurry pipelines especially at high coarse particle concentrations. This phenomenon only occurs in the lower portion of the pipe circumference. Wear caused by this phenomenon is continuous and looks like sand dunes [10].

Solid particles exiting the flow stream in straight horizontal pipe slurry flow randomly impact on the pipe wall at angles, causing cutting or fatigue of the pipe material due to impact at high velocities, or the repetitive impact of particles at the same location, respectively [10]. Fatigue occurs in brittle material, while cutting occurs in ductile material [10]. Impact erosion is highest at impact angles around 30 degrees for mild steel [20]. Erosion measurements can be made using several techniques, mainly weight loss measurement and thickness measurement. Weight loss measurement can be done using a very accurate balance while thickness measurement can be done using calibrated UT devices or nuclear devices (for better resolution) or even profilometers or micrometers [20].

Factors affecting slurry erosion in horizontal flow include [20]:

1. velocity
2. concentration
3. viscosity

4. particle size and shape
5. pipe material microstructure and characteristics

According to experimental evidence, particles larger than the viscous sublayer thickness experience a repelling force away from the pipe wall when the velocity is high [22], which results in lower pipe friction [19]. The effect of the near wall lift force is related to the size and shape of the near wall velocity profile [22]. Near wall lift causes the particles to elevate away from the pipe inner walls, and it also prevents or reduces the impact energy transferred by particles hitting the pipe inner wall [17]. In some cases of heterogeneous slurry flow with particle size larger than the viscous sublayer thickness and at higher flow velocities, the pressure drop was found to be lower than water flow at the same flow conditions [22]. However, this effect becomes negligible as the particle concentration increases and also as the velocity of the flow is lowered [17].

#### 2.4. Wear Profile in Oilsands Hydrotransport Pipelines

Pipeline wear measurement collected from Syncrude Aurora's Oil sand hydrotransport and coarse tailings pipeline between February 2005 and September 2006 were presented by Schaan et al. in [4]. Pipe wear measurements were taken at 600 locations on oilsands and coarse tailings pipeline of diameters equal to 0.737m by ultrasonic B-scan device at several locations around the pipe circumference, as part of Syncrude's Aurora mine monitoring program. The results for wear measured are for a straight horizontal section HT-B transporting oilsands at bulk flow velocity of 4.5 m/s, density of  $1550 \text{ kg/m}^3$  and temperature of 40C. The uneven wear profile along pipe circumference collected from Syncrude wear monitoring data was presented in the paper. Wear rate in mm/1000hr measured around the circumference of the pipe was plotted against the

circumferential pipe position in cm. The transported oilsands had a bitumen content between 11 and 12% and average fines content between 21 and 26%.

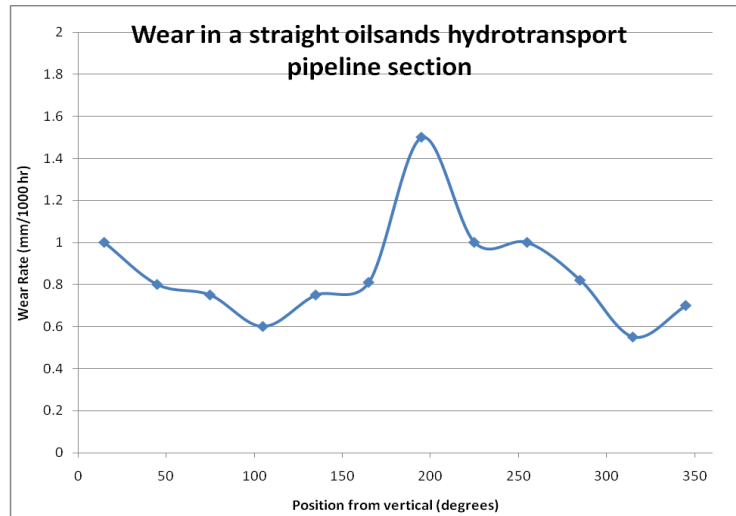


**Figure 4. Wear profile in a straight oilsands hydrotransport pipeline section [4]**

The wear profile presented in a straight section of pipe was highest at the bottom of the pipe, with wear rate just above 1.5 mm/1000 hrs as shown in Figure 4 [4]. The wear rate general trend was decreasing from the top of the pipe (0 degrees), reaching a minimum at 110 and 310 degrees and then increasing to reach a maximum close to the bottom of the pipe (200 degrees). Several factors affect the oilsands hydrotransport pipeline wear profile in a straight horizontal section of pipe such as particle size distribution, concentration, flow velocity, and suspending medium properties. The slurry bed concentration was seen as a key parameter in oilsands pipeline wear [4]. As a result, more wear occurred close to the bottom of the pipe due to the bottom bed friction with the pipe as expected by Schaan, Cook and Sanders [4]. Since the severe wear is at the bottom of the pipe, it is customary to rotate the hydrotransport pipe in service in order to maximize its useful life.

In some cases, the transition point on the pipe inner wall between the top layer and bottom layer of the oilsands hydrotransport slurry flow is the most severe wear location. The likely reason is that this location is subject to all the erosion wear mechanisms present in oilsands hydrotransport flow in addition to corrosion and combined erosion/corrosion wear mechanisms.

## 2.5. Wear Profile in Sand Slurry Pipelines

A test loop was constructed by Roco and Addie to test erosion wear modeling techniques in a controlled laboratory environment [21]. Sand slurry was tested at average slurry concentrations of 10% by volume in a 200 mm diameter loop with sand particle diameter of 0.25 mm. The sand erosion wear rate profile was compared to the predicted rate along the pipe circumference. The model is based on computer simulations to predict the velocity and concentration profile of the slurry flow inside the pipe and around the pipe circumference.

The maximum experimental wear in the constructed pipe loop occurred at the bottom of the pipe (0 degrees). The region of maximum actual wear also occurred around the maximum point of wear in the bottom section of the pipe between 270 degrees and 90 degrees. There is a discrepancy between the predicted and experimental wear rates in the upper section of the pipe especially between 90 and 270 degrees. The discrepancy may be due to underestimating the concentration of particles in the upper half of the pipe. There is also a small discrepancy between the actual location of the maximum wear and the predicted maximum wear location. Since the insitu concentration of sand slurry tested is only at 10% volume and average slurry velocity is high (around 7.92 m/s), random impact of

particles with the pipe wall is likely more dominant along the circumference of the pipe except at the very bottom of the pipe where sliding abrasion of solid particles with the pipe wall can exist.

Another study was performed by Gupta et al. [23] on the uneven erosion wear rate of a heterogeneous sand slurry in a brass slurry test loop. The uneven wear was measured along pipe circumference at fixed positions. The slurry average velocity was varied from 1.95 to 2.75 m/s. A wide size distribution of sand particles obtained from copper mine tailings stream were used (47% below 0.075 mm) in average in situ concentrations of 17.23 % up to 34.5% by weight [23]. A correlation for predicting erosion rate for brass was then found as a function of the slurry overall velocity, particle weighted mean diameter, and the slurry concentration by weight as shown in Equation 7 below.

$$W = 0.21 * 10^{-8} V^{2.1} d_{WM}^{0.273} C_w^{0.502}, \quad (7)$$

where

$W$  = wear in mm per year

$V$  = flow velocity in m/s

$d_{WM}$  = weighted mean particle diameter

$C_w$  = concentration of solid particles by weight

Although a correlation for predicting pipeline wear was developed, the effect of each wear mechanism on pipeline wear was not isolated. This equation can only be used to predict erosion wear rates in brass under the tested conditions. Moreover, the above correlation does not provide insight to the wear mechanisms contributing to erosion.

The maximum experimental wear in the constructed pipe loop occurred at the bottom of the pipe. The average slurry velocities are low at 1.95 m/s and 2.75 m/s; and the tested average concentrations are relatively high

between 17.23% and 34.5% by weight [23]. As a result, sliding abrasion wear between the unsuspended solid particles and the pipe wall may be dominant in the lower region of the pipe circumference. While random impact of sand particles with the pipe wall is dominant in the upper region of the pipe, it can be easily seen in the results that the erosion wear contribution of sliding abrasion at the bottom of the pipe is more significant than that of random particle impact at the top of the pipe. This is probably due to the higher concentration of particles in the lower region which slide against the pipe wall at lower velocities and hence can cause more erosion damage.

## 2.6. Erosion Wear Material Ranking Tests

Erosion occurs when there is motion of fluid against the wearing material. Since some fluids corrode material, corrosion contributes as well to the erosion of the material and increases wear rate at the start of the wear process [24]. There are several standard erosion tests used to rank the erosion resistance of the target material against several flow types such as solid particle erosion, falling sand erosion, gas jet erosion, slurry erosion, cavitation, and fluid impingement tests [24].

In solid particle erosion test, solid particles are shot at target material such as in sandblasting of pipe, and the repeated impacts of the solid particles against the target material causes material loss and results in erosion [24]. In falling sand, sand particles are sent free falling down a chute and hit a target material, causing erosion to occur [24]. In addition, several setups have been designed to test the target material resistance to cavitation erosion due to presence of air bubbles in the fluid [24]. Impingement tests are designed to test the resistance of the target material to erosion due to fluid flow at high velocities in bends and vessels [24]. Erosion tests

described in this paragraph cannot be used to simulate erosion wear caused by slurry flow in a straight section of pipe at steady state conditions. Some of these tests, such as solid particle erosion test and falling sand test, do not simulate erosion wear due to sliding abrasion or random impact of particles with the pipe inner wall during slurry flow in a straight section of pipe at steady state conditions. The other tests, such as fluid impingement test and cavitation test, are designed to simulate erosion wear by a single phase fluid. The flow physics in these tests are different than those experienced by slurry pipelines.

On the other hand, slurry erosion tests may be used or modified to simulate erosion wear mechanisms occurring due to slurry flow of interest. Slurry erosion tests are divided into several categories [24]:

1. Miller test
2. Wet Sand/Rubber Wheel Abrasion test
3. Wet Sand Carbide Wheel Abrasion test
4. Propeller test
5. Slurry Pot test
6. Ball Cratering Test
7. Orifice Enlargement test
8. Erosion/Corrosion test

The Miller test is the most common material erosion resistance ranking test which simulates abrasion wear due to slurry flow in a reciprocating pump [24]. A flat coupon of the tested material is placed on a reciprocating arm which moves back and forth rubbing against a flat rubber surface submerged in the intended sand slurry with known concentration and particle size distribution [24]. The number of revolutions per minute of the reciprocating arm can be increased to accelerate erosion wear in the test coupon. This test is limited because it was designed to simulate abrasion

wear in a reciprocating pump due to the reciprocating movement of the test specimen against the rubber surface.

The wet sand/rubber wheel abrasion test (ASTM G-105) is used to simulate abrasion wear due to slurry flow. The test setup consists of a rubber wheel turning at a constant speed and constantly rubbing against a test specimen of the target material submerged in sand slurry with known concentration and particle size distribution [24]. The test specimen is forced against the rubber wheel by applying a known force using dead weights [24]. In this test, the amount of force applied to keep the test specimen in contact with the rubber wheel can be varied along the speed of rotation of the rubber wheel. The wet sand carbide wheel abrasion test is identical to the wet sand rubber wheel test except that the rubber wheel is replaced with a carbide wheel. The limitation of both of these tests is that the slurry corrodes the target material. As a result, the contribution of corrosion to total wear of the specimen needs to be isolated from erosion wear due to the rubbing of the wheel with the test specimen. Another limitation of this test is that sand particles in the slurry need to be suspended in order to keep the slurry concentration consistent. In order to limit corrosion wear from occurring, corrosion inhibition must be employed by adding a corrosion inhibitor to the slurry or by protecting the test specimen with cathodic protection. On the other hand, dry sand rubber wheel abrasion test (ASTM G65) can be utilized. ASTM G65 uses the same setup but with dry sand allowed to fall freely between the rubber wheel and the test specimen [24]. Repeatability can be quite good, making this a popular wear testing protocol.

The ball cratering test is an abrasion test similar to the wet sand rubber wheel test except that a rotating steel ball forces the sand slurry against the test specimen instead of a rubber wheel [24]. The limitations of this

test are also due to corrosion and inconsistency of the slurry concentration during testing [24].

The propeller test as the name signifies consists of a propeller submerged either partially or fully in slurry with known characteristics such as concentration and particle size concentration [24]. This test is designed to simulate wear in rotating pumps and as a result should not be utilized in simulating wear due to slurry flow in a straight section of pipe.

The slurry pot test (ASTM G119) is designed to simulate wear due to erosion/corrosion [24]. Slurry pot test consists of a rotating propeller placed inside the pot which forces the slurry against electrically isolated test specimens placed on the inner wall of the pot [24]. Similarly, the corrosion/erosion test is designed to simulate wear due to erosion/corrosion in slurry for extended test duration approximately 30 days [24]. Both of these tests cannot be used to simulate erosion wear mechanisms due to the test setup design.

The orifice enlargement test is a simple test in which slurry is circulated in a pipe loop and the erosion wear rate of an orifice plate made of the target material is observed over time [24]. This test is a qualitative and comparative test in which several target materials can be tested and their resistance to erosion caused by a specific slurry of interest [24]. Since the physics of slurry flow across an orifice are different from slurry flow in a straight section of pipe, this test cannot be used to simulate abrasion erosion or random impact of particles in a straight section of pipe with slurry flow.

## 2.7. Modeling and Simulation

Many engineering problems too complicated to be solved analytically, and as a result modeling and simulation are needed to reduce the complexity of engineering problems. Modeling gives engineers the means to represent various systems, the interactions between several components or elements within a system and the ability to simulate these interactions over a specified period of time [25]. Modeling and simulation also help engineers to better understand the interactions between different elements in a system [25].

There are two means of modeling physical systems: continuous and lumped parameter. In a continuous system model, differential equations representing the continuous system are derived [25]. The differential equations are then approximated by algebraic equations in order to be able to arrive at a solution. As a result, the accuracy of the solution depends on the level of approximation made in the solution stage. On the other hand, in a lumped parameter model, the physical system is simplified [25]. As a result, a set of algebraic or differential equations can be formulated and then solved directly. The accuracy of the solution significantly depends on the model developed and the level of simplification made to the actual system physics [25]. If the system physics are oversimplified, the solution is inaccurate no matter what solution methodology is used [25].

In a lumped parameter model, the physical system is modeled using elements of known properties. Each element has a node variable flowing through it and a loop variable acting across the element. The node variable and the loop variable are related to each other by a predetermined constitutive relationship [25]. Finite-element analysis can be used to simulate wear and erosion processes. Such simulations can be

used to simulate wear mechanisms occurring due to the different wear and erosion mechanisms [24].

## 2.8. Wear Modeling in Slurry Pipeline

Some empirical models have been published in the literature to predict erosion wear due to slurry flow in many applications and at different concentrations.

Pipe wear estimation in oil and gas wells is an issue in many producing wells in order to avoid premature failure of pipe due to erosion in sand producing wells. Conservative flow production velocities reduce profitability and increase production costs. It is beneficial to develop a wear prediction model which can be used to regulate flow velocities to optimum levels without sacrificing production pipe reliability. An empirical model for predicting the erosion wear rate in sand producing gas/liquid well production pipelines at very low sand concentrations was presented by Salama [26]. The model was tested against measured wear rates presented by others for particle sizes of 0.150, 0.200, 0.250 and 0.300 mm. This empirical correlation was achieved after many tests were conducted, and the resulting equation is as follows:

$$ER = \frac{1 * W * V_m^2 * d}{Sm * \rho_m * D^2} , \quad (8)$$

where

$ER$  = erosion rate (mm/yr)

$W$  = sand production rate (kg/day)

$V_m$  = mixture velocity in (m/s)

$d$  = particle size (mm)

$D$  = pipe inside diameter (mm)

$S_m$  = geometry factor (equals 5.5 for pipe bends)

After conducting many experiments, it was concluded that erosion rate is dependant on several factors [26]:

1. Flow Properties (Flow rate, composition, density, viscosity)
2. Sand Characteristics (concentration, impact velocity, impact angle, number of particles hitting the surface, shape/sharpness, hardness, size distribution, density),
3. Component Geometry (Bend, straight pipe)
4. Material Properties (hardness, microstructure)

As we can see from the above model, the relationship between the erosion rate and the operation variables is a power relationship. The limitation for the above equation is due to the empirical nature of the equation. This equation is only applicable for very low concentrations of sand flow in oil/gas producing wells within the tested experiment range. Moreover, this relationship does not provide insight to the wear mechanisms causing erosion such as random impact and frictional erosion.

On the other hand, some researchers have used an energy approach with the aid of computer simulations to help predict wear rates in sand slurry pipelines. The development and increased power of computers have encouraged scientists to simulate pipe flows of particles at lower concentrations.

Erosion wear mechanisms were divided by Rocco and Addie into three main categories: directional impact, random collisions and Coulombic friction [21]. An energy approach was used to calculate the erosion wear

based on the solids velocity and the concentration distribution close to the pipe inner walls. In each wear mechanism, the particle-wall interaction was verified using small devices or small lab tests. A test loop was also constructed to test the model under controlled laboratory conditions. Finite element and finite volume methods were used to simulate the two phase flow in a pipeline or pump numerically in order to calculate the velocities and concentration in the vicinity of the pipe inner wall [21].

The experiments were carried out for particles of sizes smaller than 0.5 mm and at concentration of 10% by volume. Although low concentrations of sand were used, some useful equations were derived:

Wear rate due to random impact is described by

$$\Delta s'_k = \varphi_k [V_{s,tg} (\tau_{DS} - \tau_{DS_0})], \quad (9)$$

and wear rate due to friction is

$$\Delta s'_{fr} = \varphi_{fr} [V_{s,tg} (\tau_{SL} - \tau_{SL_0})] \quad (10)$$

where,

$\tau_{DS}$  is the dispersive stress

$\tau_{DS_0}$  is the incipient dispersive stress

$\tau_{SL}$  is the stress due to non suspended particles

$\tau_{SL_0}$  is the incipient stress due to non suspended particles

$V_{s,tg}$  is the tangential solid velocity

$\varphi$  is the proportionality wear constant

The significance of that work comes from the mechanistic approach used to arrive at a wear predictive model for each of the wear mechanism contributing to erosion in a pipeline. Similarly, computational fluid dynamics (CFD) simulations were used to predict wear in a straight pipe

section and an elbow section by Wood and Jones [27]. A test loop was constructed of stainless steel to validate the wear prediction model (sand particle diameter = 1mm and flow concentration of 10% by volume and mean velocity of 3 m/s). Erosion prediction in slurry pipeline components is very difficult due to the complexity of slurry flow and the inhomogeneity of the pipe material.

Erosion models are still not mature and there is room for a lot of improvement in order to arrive at better models [28]. In order to be able to predict erosion wear rates in a slurry loop, particle trajectories should be modeled appropriately. A CFD program was developed to compute particle trajectories and particle velocity near pipe inner wall [27]. By knowing the particle trajectories, the number of particle impacts can then be calculated [27].

The experimental loop consisted of a closed loop 78 mm pipe, slurry pump, pipe, elbow, and stirring tank. Flow was circulated within the loop and it was assumed that particle digestion and breakage influence the aggressiveness and the eroding efficiency of the sand. As a result, the sand was changed every run in order to ensure it properly represents actual flow conditions and its abrasiveness is not compromised [27].

Wear measurement on the slurry loop used was done with a micrometer and also with an ultrasonic testing device (UT). It was found that the estimates used with the micrometer were in better agreement with the predicted wear estimates than those measured using UT. While non destructive UT measurements were made during the tests were running, destructive testing of the pipe or bend was required for micrometer measurements to be performed. Contrary to the understanding that maximum wear in a slurry pipeline occurs at the bottom of the pipe only, this paper showed that maximum wear can also be located at the top and

at the interface between the two layers (two-layer model), depending on the flow characteristics [28].

Particle flow pattern can be determined using Electrical Resistance Tomography (ERT) technology. This technique was used by Wood, Jones, Ganeshalingam, and Miles and electrodes were used to determine regions of equal concentration utilizing the induction characteristic of a nonconductive bead slurry flow [28]. Concentration profiles for flows close to and above deposition velocities (0.5m/s, 1m/s and 2m/s) were constructed [28].

Cutting wear occurs at low angle impingement of particles with the pipe wall as in the case for impact of particles in the lower layer of the slurry flow and it is more common in ductile materials such as mild commercial carbon steels [28]. On the other hand, deformation erosion due to solid particles occurs at high impact angles and it is more common in brittle materials such as ceramics. An equation used to predict wear rates which combines both cutting and deformation wear effects was used. The results from CFD simulation gave the near wall velocities, impact angles of particles, and the concentration profiles at different locations around the pipe circumference. Erosion prediction was made based on Hashish and Bitter combined erosion models based on cutting and deformation erosion [28].

Micro cutting was found to be the dominant wear mechanism in slurry flow in straight ducts as expected by Wood et al. [28]. It was also found that CFD wear predictions were inline with the micrometer measurements but not with the UT measurements. UT measurements were not accurate due to the scatter in the data. Again, the main relevant finding for the current work is that cutting is the main wear erosion in slurry flow through a pipe.

## 2.9. Measurement of Pipe Stress in Single Phase Flow

The amount of energy imparted by the flow on the pipe wall is directly proportional to the wall shear stress value, as presented by Roco and Addie [21]:

$$E = (V * \tau_w) \quad (11)$$

where

$V$  is the tangential local velocity component, and

$\tau_w$  is the pipe wall shear stress value.

Therefore, wall shear stress measurement is needed for quantifying the contribution of wear mechanisms on the inner pipe wall. Most of the literature available on wall shear stress measurement applies to single phase flow with a few articles on non-Newtonian slurries such as paste and powder.

There are several factors to be considered when a measurement technique is to be chosen for measuring wall shear stress [29]. These factors include [29]:

1. the contribution of wall effects on the measurement technique
2. the Effect of high mean shear on the measurement
3. ensuring the flow is fully developed
4. strict resolution requirement for near wall measurement
5. the effect of pressure gradient across the measurement apparatus.

Several techniques have been developed for measuring wall shear stress in single phase flows [30]:

1. time resolved methods such as floating element sensor
2. methods for finding the time averaged wall shear stress such as oil film interferometry and preston tube methods
3. mean profile based methods such as Von Karmen integral, Clauser plot, and mean wall gradient methods

Oil film Interferometry was not used, because this method requires access to the oil film which impossible in pipe slurry flow. The continuum approach is utilized in the remaining shear stress measurement techniques mentioned above. This approach can not be applied in heterogeneous slurry flow because of the distinct behavior of slurries which include discontinuities in the flow due to the presence of solid particles.

## 2.10. Floating element sensor

A floating element sensor is the simplest sensor used in measuring wall stress due to its simple working principle [30]. The sensor has a floating surface which moves due to the friction force between the moving fluid and the surface. The floating surface is held with a set of springs in parallel forming a parallelogram linkage. The friction force is quantified by measuring the amount of force required to keep the floating element in position or by calculating the force required to bend the cantilever supports holding the floating element.

The friction force can also be inferred from strain gauge measurements on the springs holding the floating element [30]. By calibrating the strain

gauge, a relationship between friction force versus strain can be established and used in subsequent experiments to calculate the amount of stress imparted on the floating element due to the slurry flow. The main advantage of the floating element sensor is that there are no assumptions about the fluid properties and surface characteristics. The floating element utilizes direct measurements of the instantaneous average stress experienced over the area of the element [30].

There are several disadvantages for the floating element sensor which sprout from sensor's mechanical nature [30]:

1. the floating element has to be large enough necessary for the ensuring an accurate measurement of the friction force;
2. the gap between the floating element and the flow pipe creates disturbances in the flow;
3. the floating element has to be perfectly aligned with the inner pipe wall for accurate wall stress measurements;
4. there are other factors that may contribute to errors in this measurement technique which are temperature changes, heat transfer, pressure gradient forces, leaks, and fluctuation of the normal forces; and
5. the floating element surface area should not be too large because the pressure gradient acting on the element will greatly affect its accuracy.

The floating element sensor must also be easily accessible for inspection and recalibration if required. Despite the difficulties encountered with using a floating element sensor for wall shear stress measurement, no previous knowledge of the flow is needed, which can be considered an advantage. The development of micro electro-

mechanical systems floating element sensors will likely increase the accuracy and frequency of this measurement technique [30].

### 3 Sand Slurry Erosion Wear Model Development

#### 3.1. Oilsands Flow Modeling and Simulation

A simple lumped-parameter model of the physics of flow of oilsands slurry in a straight pipeline section was formulated by Lipsett based on the improved two-layer model [7]. This oilsands slurry flow model assumes horizontal pipeline oilsands flow at steady-state conditions with no transient conditions occurring during the flow [7]. The flow processes were assumed to occur sequentially and independently [7].

The oilsands flow was divided into two layers: a top layer and a bottom layer based on the improved two-layer model. The oilsands slurry flow model is represented graphically as shown below in Figure 5.

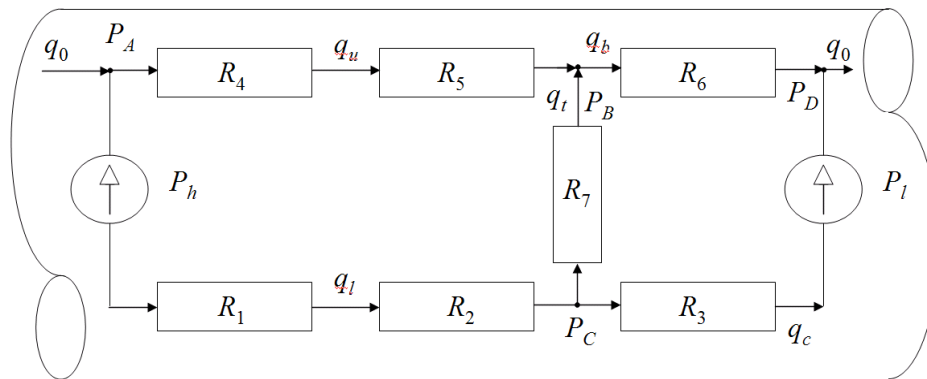


**Figure 5. Physical system model of oilsands slurry pipeline section [7]**

In the upper layer, three flow processes occur. The first flow process is upper layer friction represented by flow component  $R_4$  followed by top layer mixing represented by flow component  $R_5$ . Finally, top layer bitumen conditioning flow process is represented by flow component  $R_6$ .

In the bottom bed layer, three flow processes also occur. There is bottom layer friction, followed by bottom layer particle digestion, and finally bottom layer mixing represented by flow components  $R_1$ ,  $R_2$ , and  $R_3$  respectively. As larger lumps of oilsands present in the bottom layer break apart during transportation, smaller particles such as clays are released in the flow which move to the top layer due to carrier fluid turbulence. A fraction of the bitumen present in the bottom bed layer gets liberated from the oilsands matrix during transportation. The liberated bitumen moves due to carrier fluid turbulence to the upper layer. Both of these flow processes are represented by flow component  $R_7$  in the heterogeneous oilsands flow model.

There exists a slight pressure difference between the top layer and the bottom layer which was taken care of in the model by  $P_h$  and  $P_l$  upstream and downstream of the horizontal pipe section respectively. The pressure difference is due to the difference in concentration and velocity profile of the upper layer and the bottom layer as indicated by the two-layer model.

### 3.2. Sand Slurry Erosion Wear Model

In order to arrive at a solution to the oilsands pipelines wear problem, it is important to understand the erosion wear mechanisms affecting oilsands slurry pipelines. As a first step in investigating erosion wear mechanism affecting oilsands hydrotransport pipeline reliability and integrity, it is beneficial to simplify the problem and gain a solid understanding of the wear mechanisms that occur. It is also important to quantify the contribution of each of the wear mechanisms to the overall erosion wear.

It was decided to simplify the physics of the flow and reduce the number of flow processes by eliminating the bitumen conditioning and particle digestion flow processes from the physical flow model. Replacing oilsands with sand and studying wear mechanisms affecting sand slurry pipelines is a good starting point. The difference between erosion wear mechanisms affecting sand slurry pipelines and oilsands hydrotransport pipelines is primarily due to the presence of bitumen and oversized particles in hydrotransport pipelines.

Erosion wear mechanisms acting on a straight section of sand slurry pipeline are similar to erosion wear mechanisms acting in an oilsands slurry pipeline, which are mainly due to random impact of sand particles with the pipe inner wall, friction between the suspended slurry flow with the pipe wall, and sliding of the slurry bed against the pipe inner wall. Random impact of sand particles with the pipe inner wall is caused by carrier fluid turbulence. In oilsands hydrotransport pipelines, the contributions of bitumen conditioning and particle digestion flow processes to overall wear complicate the problem, because it is difficult to account for the individual contribution to wear rate caused by each of these flow processes.

In the simplified sand slurry flow model the resistance coefficient representing the top-layer conditioning ( $R_6$ ) is excluded, because sand slurry flow does not contain bitumen [9]. Similarly, the friction resistance coefficient representing shifting of bitumen droplets and clay particles from the bottom layer to the top layer ( $R_7$ ) can be removed [9]. At the beginning of the flow model development, it was assumed that the sand particle size distribution remains constant during the test period and as a result resistance coefficient representing the pressure drop due to particle size digestion ( $R_2$ ) can be safely neglected [9]. This assumption can be

validated after each wear test by measuring particle size distribution of a sample of sand tested [9].

The simplified sand slurry flow model in a straight section of pipe can be represented as shown in Figure 6 [9].

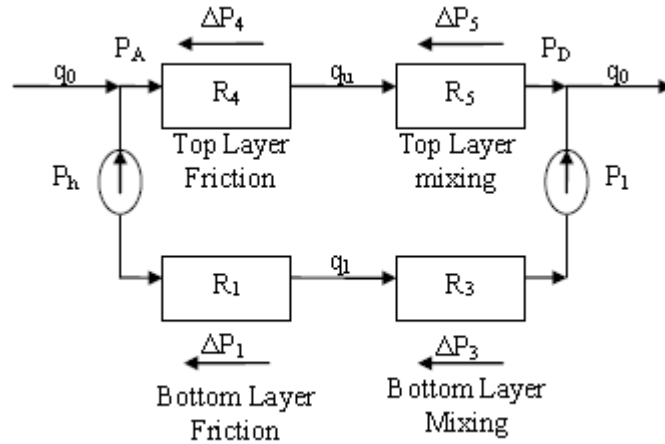


**Figure 6. Simplified physical model of sand slurry pipeline section [9]**

Dense sand slurry flow is naturally divided into two layers: a top layer and a bottom layer. Solid particles are fully suspended in the top-layer due to carrier fluid turbulence. As a result, top layer pressure drop can be mainly attributed to top layer kinematic friction with the inner pipe wall and top layer mixing [17].

On the other hand, a fraction of the bottom-layer solid particles are fully suspended by bottom layer carrier fluid turbulence and the remaining fraction of solid particles is simply supported by the pipe inner wall [17]. The fraction of particles supported by the pipe inner wall forms a moving bed in the bottom layer of the sand slurry flow. As a result, bottom layer pressure drop can be mainly attributed to kinematic friction, mixing of bottom layer, and Coulombic friction [17]. In order to differentiate the

contribution of kinematic friction from the contribution of Coulombic friction in the bottom layer, resistance coefficient  $R_7$  is split into two subcomponent coefficients  $R_{11}$  and  $R_{12}$  as shown in Figure 7.  $R_{11}$  represents kinematic friction flow process and  $R_{12}$  represents Coulombic friction flow process in the bottom layer [9].

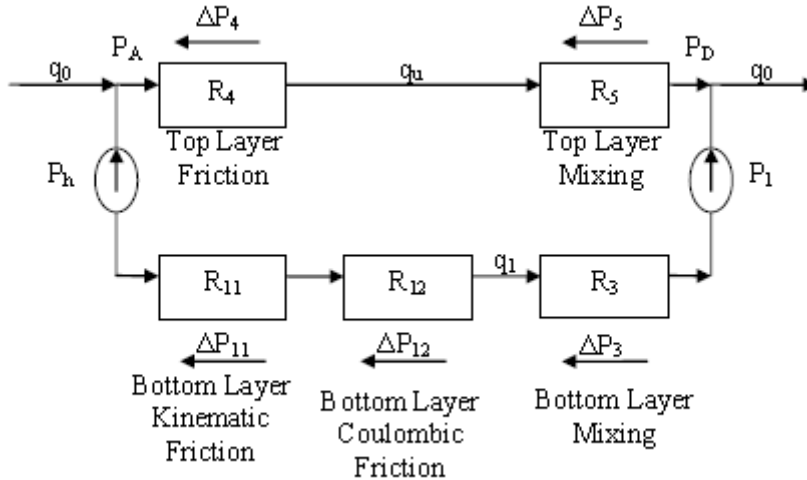


**Figure 7. Simplified physical model of sand slurry pipeline section**

From the sand slurry flow model, it is easy to realize that the slurry flow kinetic energy is lost due to two main flow processes. The first flow resistance is caused by friction of slurry mixture against the pipe wall [9]. A fraction of the energy consumed by slurry friction with the inner pipe wall in both top and bottom layers is transformed into heat, some of which causes the temperature of the slurry and the pipe to rise, with remaining heat dissipated. The remaining fraction of the energy contributes to pipe wall damage [9].

The second flow resistance is due to the mixing of the slurry. Slurry mixing is required to keep a fraction of particles suspended which lowers pipe erosion wear rates. A fraction of the mixing energy is lost due to upper and bottom layer mixing which keeps sand particles suspended [9]. The

remaining fraction of the mixing energy causes a number of particles to exit the flow streamlines and impact the pipe inner wall at low angles [27]. A fraction of the energy transmitted through impact causes pipe inner wall wear [9].

The energy that contributes to pipe inner wear erosion damage can be represented in the flow model by introducing coefficients that relate velocity to wear [9]. The modified physical model becomes a wear model, provided that the contribution of each of the wear mechanism is represented [9].

As a result, wear coefficients representing the contribution of each of the erosion wear mechanisms to the total system erosion wear rates can be used to formulate a sand slurry erosion wear model as shown in Figure 8 [9].

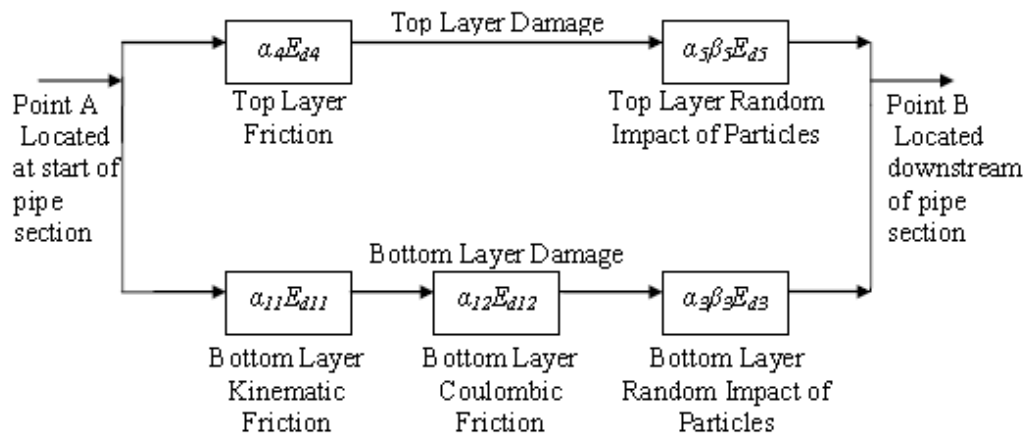


**Figure 8. Simplified wear damage model of sand slurry pipeline section [9]**

In the above wear model,  $\alpha_1$  is the wear coefficient due to bottom layer kinematic friction. Likewise,  $\alpha_{12}$  is the wear coefficient due to bottom layer Coulombic friction. Similarly,  $\alpha_3$  is the wear coefficient due to particle

impact with pipe inner wall in the lower layer;  $\alpha_4$  is the wear coefficient due to top layer kinematic friction in the top layer; and  $\alpha_5$  is the wear coefficient due to particle impact with pipe inner wall in the upper layer.

On the other hand,  $\beta_3$  is the energy fraction causing particles to exit flow streamlines and impact pipe inner wall in the lower layer. Likewise,  $\beta_5$  is the energy fraction causing particles to exit flow streamlines and impact pipe inner wall in the upper layer.

Roco et al. presented a general equation which can be used to determine the wear contribution of each of the wear components [21]. The general form of the erosion wear prediction equation is given by:

$$\Delta s' = \alpha * (E_t - E_o) \quad (12)$$

Equation 12 can be expanded further as:

$$\Delta s' = \alpha * [V * (\tau - \tau_o)] \quad (13)$$

and can be also expressed as:

$$\Delta s' = \alpha * (E_d) \quad (14)$$

where

$\Delta s'$  is the wear rate by the corresponding wear mechanism in units of (mm/hr);

$E_d$  is the rate of energy transfer to the pipe wall contributing to damage in units of (energy per unit area/time);

$E_t$  is the total rate of energy transfer to the pipe wall in units of (energy per unit area/time);

$E_o$  is the threshold energy rate for incipient wear above which damage starts to accumulate (energy per unit area/time);  
 $\tau$  is the stress caused by the wear component on the pipe wall in units (force/area);  
 $\tau_o$  is the threshold stress for incipient wear caused by the wear component on the pipe wall in units of (force/area);  
 $V$  is the local tangential velocity component for each wear mechanism in units of (displacement/time);and  
 $\alpha$  is the wear coefficient of each wear component in units of ((thickness)/(energy per unit area)).

At the top layer of the slurry pipeline flow, two wear components contribute to the erosive wear of the pipe. The first component is friction between the slurry mixture, composed of the solid particles and the suspending medium, and the pipe wall. The second component contributing to the pipe wear is the random impact of particles with the pipe wall due mainly to particle-particle interaction and also due to turbulence causing the particles to exit the flow stream line and hit the pipe internal wall.

By knowing the local velocity corresponding to each wear component and the shear stress, more complex wear prediction equations can be developed to better predict the erosion wear rate due to each wear mechanism. Meanwhile, Equation 13 can be used as preliminary wear prediction equation, and this equation indicates the need for wall stress measurement in order to relate wear rate to the wear processes causing damage separate from the flow processes.

As a result, there is a need to develop a device to be used to measure stress experienced by the pipe wall during slurry tests to determine the pipe wall stress and the threshold stress for incipient wear. The wall force measurement together with the pipe wall thickness removed during fully

suspended heterogeneous slurry flow in a straight section of pipe can be used to find the corresponding wear coefficient. This measurement technique can be later used to measure forces during slurry flow with sliding bed.

### 3.3. Model Validation Issues

In order to validate the proposed model it is necessary to evaluate the parameters  $R$ ,  $\alpha$ ,  $\beta$ , and  $E_d$  for each of the erosion wear mechanisms. It is also required to isolate each of the wear mechanisms in order to calculate the corresponding parameters of interest. Isolation of the kinematic friction and random impact of particles from the Coulombic friction can be achieved in a fully suspended heterogeneous slurry flow by increasing the flow velocity. In a fully suspended flow condition, a symmetric concentration and velocity profile exists in the pipe where Coulombic friction flow process can be eliminated. The resulting flow consists of one layer of fully suspended slurry flow. The kinematic friction and random impact of particles can be lumped together in order to validate the flow model shown in Figure 9.

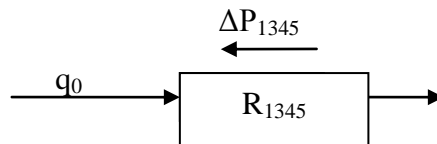


**Figure 9. Simplified physical model of sand slurry pipeline section for fully suspended flow**

The resistance coefficient  $R_{1345}$  corresponding to the kinematic friction and random impact of particles due to slurry mixing in the fully suspended slurry flow can be determined for a variety of flow conditions by measuring

the pressure drop across a laboratory test section in a slurry loop. By controlling the slurry flow rate, the in situ particle concentration, density of particles, carrier fluid viscosity, and particle size distribution, a variety of near wall particle velocities and concentrations around the pipe circumference can be achieved. A set of  $R_{1345}$  values can be determined for a range of flow conditions. At this stage, it is important to prevent damage accumulation from occurring in the pipe by covering the pipe with an abrasive resisting overlay. Care must be taken in choosing the right overlay material which has the same roughness as the pipe itself. This will ensure that no energy is lost due to pipe wall erosion wear damage process.

Erosion damage in a fully suspended heterogeneous slurry flow condition causes additional pressure drop in the piping system above a threshold point which can be represented as shown in Figure 10 [31].

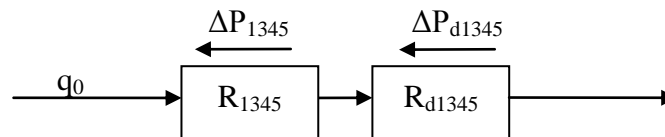


**Figure 10. Parametric representation of sand slurry flow and erosion damage for fully suspended flow**

The damage caused is a function of the pressure drop and the flow rate which is also a function of velocity and concentration [31]. The threshold energy for incipient pipe wear can be estimated for a variety of flow conditions by coating the pipe wall with a thin layer of paint. As the paint layer starts to get damaged, the threshold point for incipient wear can be determined. Another potential method to determine the threshold energy for incipient wear is by recording acoustic emissions in the vicinity of the pipe [32]. The acoustic emission method needs to be tested in a slurry application and the unique signature frequency at which damage occurs

should be identified. The amplitude of the damage signature frequency may correlate well with the threshold stress for incipient wear.

The total energy dissipated in the system can be expressed as:

$$\frac{\Delta P_{t1345}^2}{2R_{t1345}} = \frac{\Delta P_{1345}^2}{2R_{1345}} + \frac{\Delta P_{d1345}^2}{2R_{d1345}} \quad (15)$$

$$U_{total} = \frac{\Delta P_{t1345}^2}{2R_{t1345}} \quad (16)$$

$$U_{threshold} = \frac{\Delta P_{1345}^2}{2R_{1345}} \quad (17)$$

$$U_{damage} = \frac{\Delta P_{d1345}^2}{2R_{d1345}} \quad (18)$$

where

$U_{total}$  is the total energy dissipated in the system,

$U_{damage}$  is the energy fraction contributing to damage in the system,

$\Delta P_{t1345}$  is the total pressure drop in the system in Pa,

$\Delta P_{1345}$  is the pressure drop in the system due to slurry flow in Pa,

$\Delta P_{d1345}$  is the additional pressure drop in the system due to erosion damage in Pa,

$R_{t1345}$  is the resistance coefficient representing total pressure drop in the system,

$R_{1345}$  is the resistance coefficient representing pressure drop in the system due to slurry flow, and

$R_{d1345}$  is the resistance coefficient representing erosion damage

The energy contributing to damage can therefore be expressed as:

$$U_{d1345} = \frac{\Delta P_{t1345}^2}{2R_{t1345}} - \frac{\Delta P_{1345}^2}{2R_{1345}} \quad (19)$$

The damage mechanism is related to damage of the pipe wall by a wear coefficient; and the damage rate can be expressed as:

$$\Delta s' = \alpha_{1345} E_{d1345} = \alpha_{1345} (U_{d1345} / area) = \alpha_{1345} \left[ \left( \frac{\Delta P_{t1345}^2}{2R_{t1345}} - \frac{\Delta P_{1345}^2}{2R_{1345}} \right) / area \right] \quad (20)$$

$$\Delta s' = \alpha_{1345} * [V * (\tau_{1345} - \tau_{o1345})] \quad (21)$$

By measuring the total pressure drop in the pipe section, velocity, and concentration at the same flow conditions used to find  $R_{1345}$  values,  $R_{i1345}$  values can be determined. The total energy in the system and the threshold energy for incipient wear can then be computed using Equation 16.

Also, by measuring the pipe erosion damage rate using an ultrasonic thickness measurement device, and the local stress experienced by the pipe wall, and the threshold stress for incipient wear, the erosion wear coefficient  $\alpha_{1345}$  can be determined using Equation 21.

Once the threshold for incipient wear,  $\alpha_{1345}$  values,  $R_{1345}$  values, and  $R_{t1345}$  values for a wide range of flow conditions are determined, the contribution of kinematic friction to erosion pipe wear in the bottom layer of heterogeneous sand slurry flow can be determined. Similarly, erosion damage in heterogeneous slurry flow due to Coulombic friction causes additional pressure drop in the piping system which can be represented as shown in Figure 11. Since kinematic friction, Coulombic friction, and random impact of particle due to bottom slurry mixing do not occur sequentially, isolation of Coulombic friction contribution to pipe erosion damage is difficult.

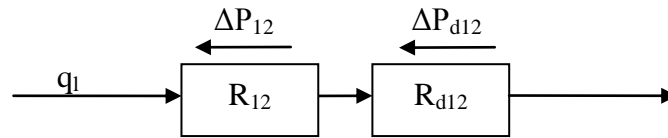


**Figure 11. Parametric representation of sand slurry flow and erosion damage due to sliding bed**

In order to determine  $\alpha_{12}$ , an ASTM G65 rubber wheel test can be used or any other similar wear test that can emulate process conditions. Other test options include the oscillating table test [21] and the wet sand rubber wheel test [24]. The ASTM G65 test [24] is an industry standard wear test since it yields fairly repeatable results, and the wear mechanism resembles the sliding abrasion wear due to particles suspended by pipe wall despite being a dry test in air. The apparatus is illustrated in Figure 12. It is critical to mention here that the solid particle distribution used in the test must resemble the pipe flow conditions. Otherwise, the calculated wear coefficient does not resemble the true resistance of the pipe material to the slurry flow.

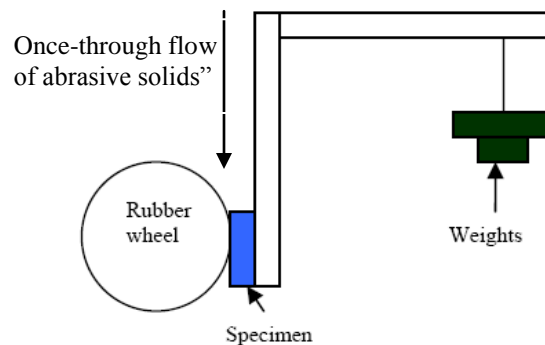


**Figure 12. A simplified schematic illustration of the ASTM G65 test.**

By knowing the suspended arm weight, the sliding friction shear stress can be calculated by multiplying the normal force by a dynamic friction factor (usually assumed to be 0.5 for sand particles). The velocity of the flowing sand particles can be assumed to be equal to the velocity at the tip of the rubber wheel. Therefore, the wear coefficient for sliding wear in the bottom layer can be calculated for the slurry/material combination since the wear rate experienced by the specimen can be measured directly. As previously mentioned, the threshold conditions for incipient pipe wear can be estimated by coating the wear sample with a sacrificial thin layer of paint or possibly by acoustic emission monitoring. Once determined, a curve of the wear coefficients calculated at different particle velocities can be constructed and used to predict wear in the bottom layer of the pipe due to particle sliding abrasion.

To predict wear due to sliding bed abrasion, wall stress measurements need to be performed around the circumference of pipe. The contribution of kinematic friction to damage around the circumference of the pipe by knowing  $\alpha_{1345}$  values,  $R_{1345}$  values, and  $R_{t1345}$  values obtained in the fully suspended flow tests. The velocity and concentration profile across the pipe wall should be also developed in order to isolate the contribution of kinematic friction to pipe wall damage. To understand local wall effects, additional flow monitoring and visualization techniques are required to measure the near wall velocity and concentrations of suspended particles and sliding bed. Advanced flow visualization techniques may include a high speed camera or an in-flow borescope.

The threshold stress for incipient wear due to Coulombic friction wear mechanism can be determined by measuring the stress required to start wear in the small scale lab tests. Once the stress, threshold stress for incipient wear, particle sliding velocity, and wear coefficient are determined, a model for erosion due to Coulombic forces can be validated

and used for predicting erosion wear rates around the circumference of the pipe during heterogeneous slurry flow.

### 3.4. Experimental System and Testing Methodology

Wall shear stress measurements are required to find the parameters of the sand slurry erosion wear model for fully suspended heterogeneous slurry flow in a straight section of pipe. These measurements are also required to predict the contribution of each of the wear mechanisms involved.

A floating-element sensor assembly was designed and constructed as a spool section in order to measure the force exerted by the slurry on the pipe inner wall during fully suspended heterogeneous slurry pipe flow. As discussed earlier in the literature review section, a floating element sensor is a simple apparatus to measure the friction force between the moving slurry and the pipe wall. The measured friction force can be later converted to wall stress.

The sensor has a floating wear sample which moves due to friction between the moving slurry and the top surface of the floating wear sample. The floating element assembly is shown in Figure 13, Figure 14 and Figure 15.

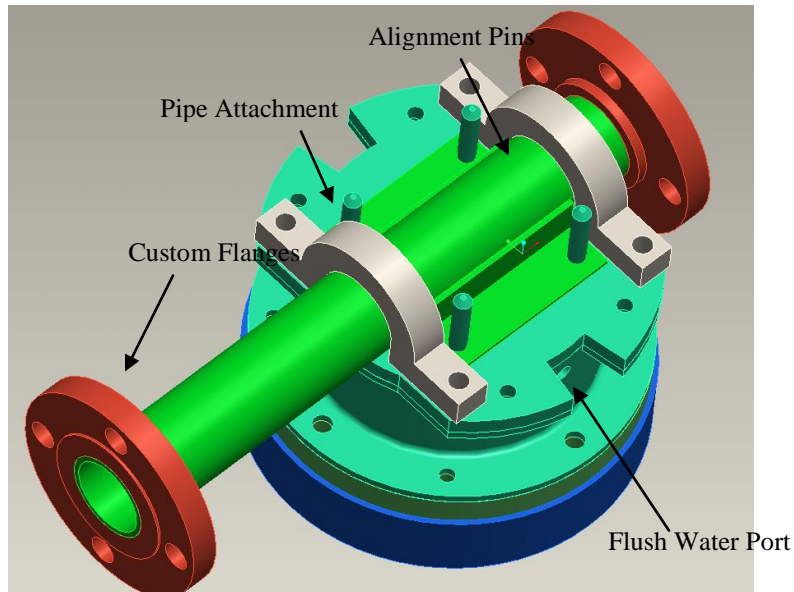


**Figure 13. Overview of the floating element sensor assembly**

### 3.5. Floating Element Components Description

The floating element assembly consists of the following components as illustrated in Figure 14:

1. Wear Sample
2. Wear Sample Holder
3. Cantilever Element
4. Base Plate
5. Cantilever Support
6. Base Ring
7. Outer Shell Top
8. Outer Shell
9. Splash Guard
10. Bottom Lid
11. Pipe
12. Pipe Attachments

- 13. Alignment Pins
- 14. Custom Flanges
- 15. Guard

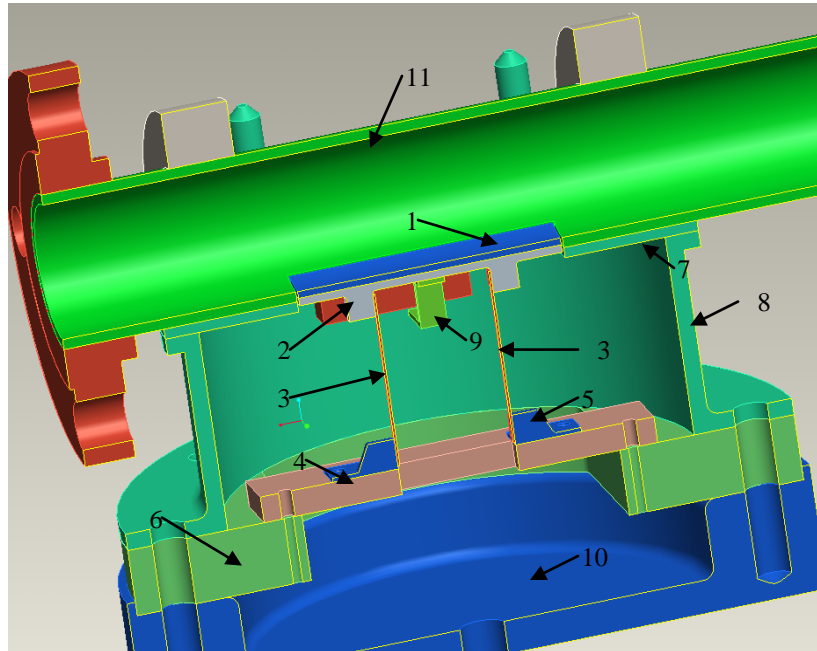


**Figure 14. Cross section view of the floating element sensor assembly**

The wear sample (101.6 mm L x 25.4 mm W) labeled component #1 and located at the top of the floating element assembly is in direct contact with the slurry flow. In the testing stage, the construction material of component #1 can be varied as desired. Different construction materials such as abrasion resistant steel can be tested and compared to the reference material. The current construction material is SA-106 grade B chosen identical to pipe material in order to maintain the same friction factor between the sample and the flowing slurry.

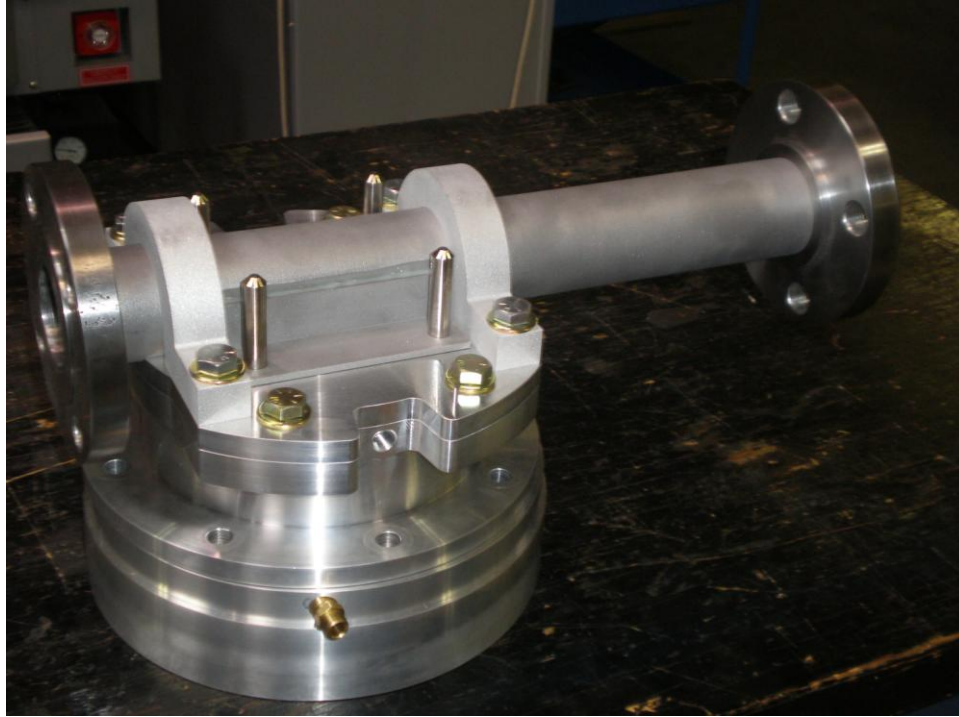


**Figure 15. Photo of the floating element assembly**

Component #1 was bonded to the wear sample holder using a very strong epoxy adhesive designed to withstand wet and severe environments. The reason for gluing these two components together is to avoid distorting the wear sample during the machining process. Component #1 was machined out of the same pipe used in the assembly using Electrical Discharge Machining (EDM), an advanced machining technique which uses electricity for precise machining. It was utilized in the construction of the wear sample to machine the wear sample out of the same pipe used in the assembly. As a result, component #1 has the same microstructure as the rest of the pipe. This technique eliminates alignment issues of the wear sample with the pipe inner wall since the wear sample is taken from the pipe used in the assembly and hence they have the same inner radius variation. A photograph of the floating element wear sample alignment is shown in Figure 16.

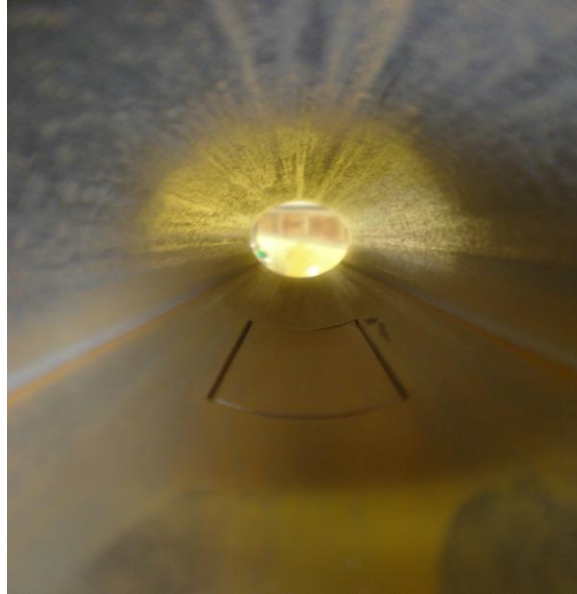


**Figure 16. Alignment of wear sample with pipe wall**

The gap size between the floating wear sample and the pipe wall was chosen primarily to prevent plugging of the gap with flowing sand particles. Plugging of the gap with sand will prevent the cantilever supports from deflection due to the flow and results in error in the output measurements. In addition, the gap size has to be big enough to allow for sufficient deflection of the cantilever supports at a variety of slurry flow conditions. Coulombic stress calculations were performed based on the two-layer model for the worst case flow condition. The in situ concentration of the flow was assumed to be 35% by volume and the particle mean diameter was assumed to be 500  $\mu\text{m}$ . It was also assumed that the angle between the bottom-top layer transition and the centerline of the pipe is 60 degrees and the friction factor between the sliding sand particles and the pipe wall is equal to 0.5. The calculated Coulombic force was 0.3 N. Kinematic stress calculations were performed for fully suspended flow at solid particle in situ concentration of 35% by volume and at 6 m/s flow velocity and the corresponding kinematic friction was calculated to be approximately 0.3 N, close to the calculated Coulombic force case.

A safety factor of 2 was applied to the calculated force value and the corresponding deflection was 0.75 mm based on Equation 22 for calculating the maximum deflection of a cantilever beam. As a result, the gap size was chosen as 0.75 mm between the floating wear sample, which prevents plugging of the gap with sand particles and allows for testing under various slurry flow conditions.

$$Deflection_{\max} = \frac{FL^3}{3EI} \quad (22)$$

where

$F$  is the shear force (N),

$E$  is the Young's modulus for Aluminum = 70,000 MPa, and

$I$  is the second moment of inertia for the cantilever support =  
(depth\*thickness<sup>3</sup>)/12 = 0.25 mm<sup>4</sup>

Component #2, the wear sample holder, provides support to the wear sample. Holes drilled at the bottom side of the wear sample holder provide connection with the cantilever element. A guard attached to component #2 was designed to keep component #1 and #2 within the floating element assembly in case of cantilever element failure.

Two cantilever elements, labeled components #3, were bolted to the bottom of the wear sample holder. The presence of the gap between the pipe and the wear sample allows the cantilever elements to deflect due to the slurry friction. Two full Wheatstone bridges were bonded on the cantilever elements lower ends to measure the strain induced by the friction and axial forces. The strain gauges were carefully positioned away from any stress concentrations locations to ensure linearity of output readings. The cantilever element is slotted at both ends which allows for movement of the element slightly vertically up or down for alignment purposes.

Similarly, the cantilever supports were tagged components #5. These two components provide support to the cantilever elements. Component #5 is slotted to allow for room to move the cantilever element sideways horizontally left or right slightly for alignment. The base plate, marked component #4, is also slotted to allow for movement of the wear sample horizontally inwards or outwards slightly for alignment purposes. A photo of the wear sample holder assembly is shown in Figure 17.

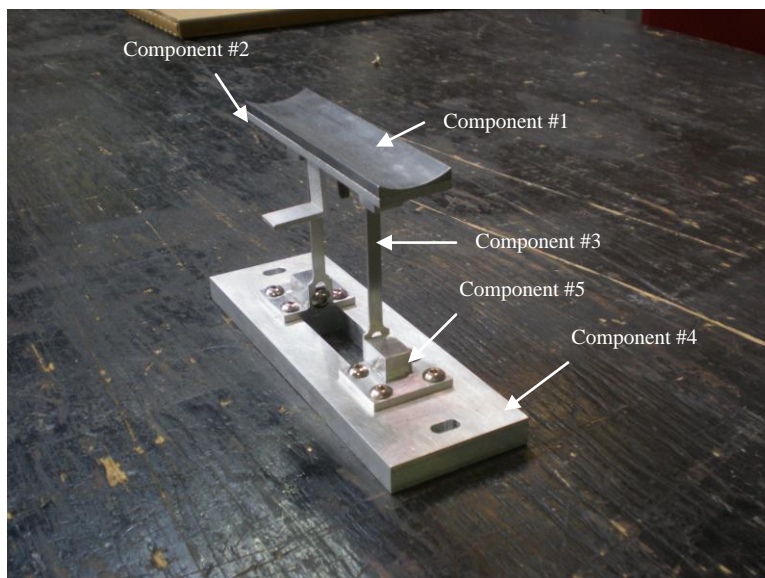


**Figure 17. Photo of wear sample holder assembly**

Full Wheatstone bridge strain gauge combinations were used in order to compensate for temperature changes during the test and to increase the sensitivity of the measurement. A relationship between the amount of friction force and the measured strain was established by calibrating the floating strain gauges in a controlled environment prior to installation.

The base ring or component #6 was included in the assembly to be able to take the bottom lid off without having to disassemble the rest of the components. This option allows for easier internal inspection of the

assembly without having to realign the critical components such as the wear sample with the pipe inner wall. The electrical wires from the strain gauges were passed through a 3/8" NPT connection drilled into the side of the base ring. The electrical connection was sealed with epoxy to prevent leakage of water through this connection.

The outer shell, labeled component #8, was designed to withstand the pressure inside the assembly. The design pressure of the assembly was chosen as 207 psi as it is the maximum pressure the laboratory piping system may experience during testing. The chosen shell thickness was 6.35 mm bigger than the minimum required shell thickness of 0.62 mm giving a safety factor of 5 and a corrosion allowance of 3.175 mm. Sample calculations of the minimum required shell thickness are included in Appendix. Two 3/8" NPT connections were drilled on the sides of component #8 for flush water connection. Flush water is needed to ensure that no sand particles get trapped in the gap between the wear sample and the pipe by maintaining a small positive differential pressure between the flush water and the slurry flow. The force-strain relationship can be corrected for the additional stresses and strains caused by the introduction of flushing water in the assembly.

On the inside of the outer shell, two splash guards marked as component #9 were attached to cover the flush water connections. The reason for installing splash guards was to prevent water from impinging directly on the cantilever elements. A photograph of the process connection of the flush water supply is shown in Figure 18.

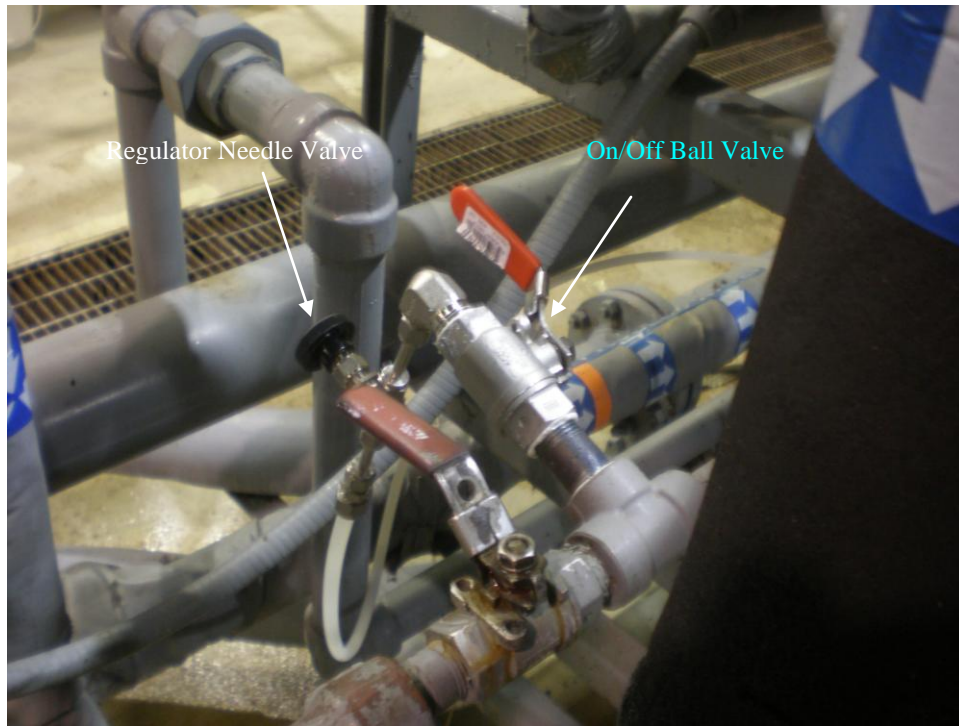


**Figure 18. Flush water supply connection to the floating element assembly**

The bottom lid, tagged component #10, can be easily removed without the need to remove the assembly from the pipe or any other components within the assembly. This allows for easy internal inspection of the assembly components and for cleaning. A 3/8" NPT connection was drilled at the bottom side of component #10 for draining the system.

Two clear pipe sections have been designed and constructed at the University of Alberta to view the slurry flow as it moves within the pipe. The first section is 1016 mm in length approximately 20 times the pipe inner diameter. This clear section was placed upstream of the floating element assembly in order to view the effect that the floating element has on the upstream flow. The second section length was chosen to be 508 mm, approximately 10 times the pipe inner diameter. This section was

placed downstream of the floating element assembly in order to view the effect that the floating element has on the downstream flow.

The flanges on the floating element pipe were specially designed to reduce the disturbance in the flow due to the presence of a gasket protruding into the flow, as is the case of weld neck and slip on flanges used in the oil and gas industry. The mating flanges on the clear section were also designed to match the flanges on either ends of the floating element. A slip-on flange with an o-ring elastomer gasket design on both inlet and outlet flanges was chosen to reduce flow disturbance, as shown in Figure 19.

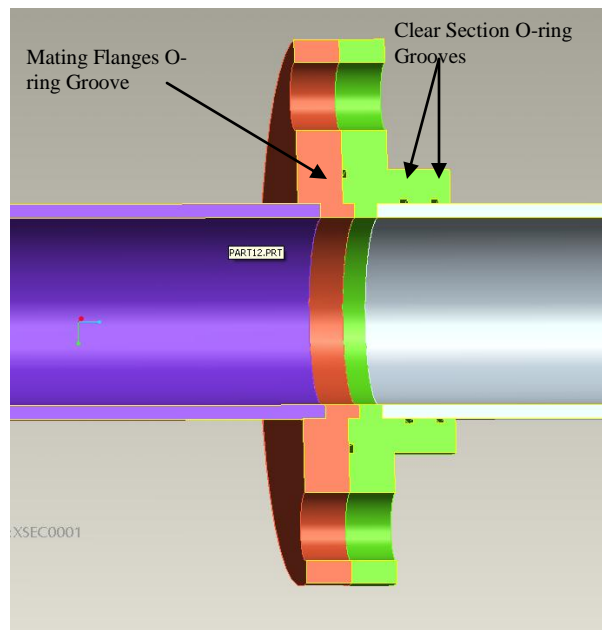


**Figure 19. A cross-sectional view of the clear section and floating element pipe assembly**

The clear section slip-on flange is removable, which allows for the replacement of the clear section if it gets scratched due to sand slurry flow. In order to prevent leakage between the clear section slip on flange

and PVC pipe, two o-rings were placed in between the pipe and the slip on flange. Similarly, an o-ring was placed between the floating element assembly slip on flange and the clear section slip on flange in order to prevent leakage between the faces of the flanges. All o-rings were designed to withstand a pressure of 375 psi, and the o-ring grooves were machined based on o-ring manufacturer specifications as shown in Appendix. Long threaded studs connecting the two slip on flanges on each clear section were used to prevent the flanges and the clear PVC pipe from separating as shown in Figure 20.



**Figure 20. Photo of clear section**

Since the maximum operating pressure inside the floating element chamber was estimated to be around 50 psi, a special anaerobic RTV sealant was used to seal between the floating element assembly pipe and shell.

The construction material for the internal components was chosen to be aluminum because of its light weight and resistance to corrosion. On the other hand, the two custom pipe flanges, the pipe, and the wear sample were constructed out of carbon steel.

Two full Wheatstone bridges installed on the cantilever supports of the floating element sensor provide strain measurements as shown in Figure 21.

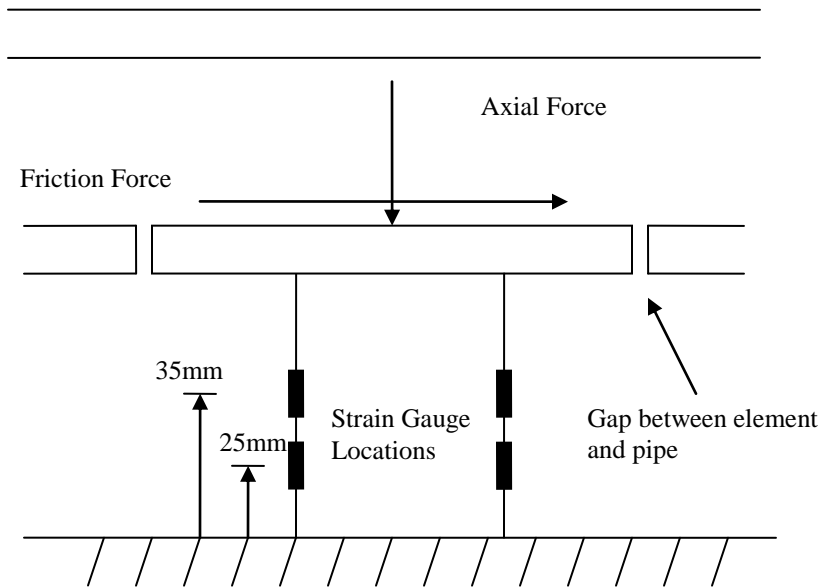


**Figure 21. Illustration of the strain gauge setup of the floating element sensor**

The stress-strain relationships in the x, y and z a direction for isotropic material can be calculated as follows based on Hooke's Law:

$$\varepsilon_x = \frac{\sigma_x}{E} - \nu \frac{\sigma_y}{E} - \nu \frac{\sigma_z}{E} + \varepsilon_{Temperature} \quad (23)$$

$$\varepsilon_y = \frac{\sigma_y}{E} - \nu \frac{\sigma_x}{E} - \nu \frac{\sigma_z}{E} + \varepsilon_{Temperature} \quad (24)$$

$$\varepsilon_z = \frac{\sigma_z}{E} - \nu \frac{\sigma_y}{E} - \nu \frac{\sigma_x}{E} + \varepsilon_{Temperature} \quad (25)$$

where

$\varepsilon_x$  is strain in the x direction,

$\varepsilon_y$  is strain in the y direction,

$\varepsilon_z$  is strain in the z direction,

$\sigma_x$  is normal stress in the x direction,

$\sigma_y$  is normal stress in the y direction,  
 $\sigma_z$  is normal stress in the z direction,  
 $\nu$  is Poisson's ratio = 0.3 for aluminum ,  
 $E$  is the modulus of elasticity of the cantilever element material,  
 and  $\varepsilon_{Temperature}$  is the strain due to the difference in coefficient of expansion between the strain gauge and the cantilever element material.

It is assumed that shear force due to flow friction ( $F_y$ ) and axial force due to solid particle impact and turbulence ( $F_x$ ) act on the surface of the wear element.

The axial bridge, shown in Figure 22 and Figure 23, measures the strain experienced by the cantilever support due to axial force while eliminating the strain contribution of the shear.

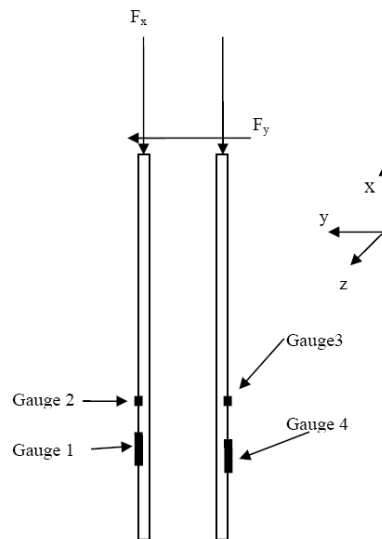


**Figure 22. Side view of axial bridge strain gauge configuration**

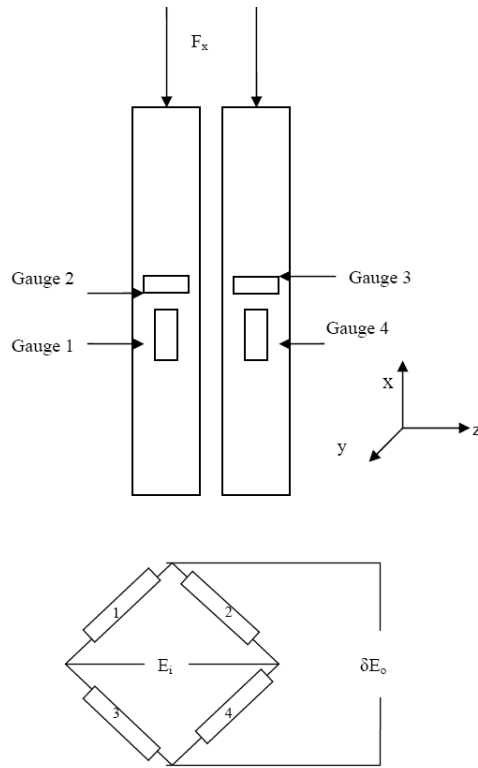


**Figure 23. Front view of axial bridge strain gauge configuration**

Axial bridge stresses at gauge is calculated as

$$\sigma_{x1} = \frac{(-F_y)(d_1)(y)}{I} + \frac{(-F_x)}{A}, \quad (26)$$

where

$\sigma_{x1}$  is the normal stress for gauge 1 in the x direction,

$F_y$  is the shear force in the y direction,

$F_x$  is the axial force in the x direction,

$I$  is the moment of inertia,

$A$  is the cross sectional area of the cantilever element,

$d_1$  is the distance between the shear force and strain gauge 1, and

$y$  is equal to half of the cantilever element thickness.

Other stresses are calculated similarly:

$$\sigma_{x4} = \frac{(F_y)(d_1)(y)}{I} + \frac{(-F_x)}{A}, \quad (27)$$

$$\sigma_{x2} = \frac{(-F_y)(d_2)(y)}{I} + \frac{(-F_x)}{A}, \quad (28)$$

$$\sigma_{x3} = \frac{(F_y)(d_2)(y)}{I} + \frac{(-F_x)}{A}, \quad (29)$$

$$\sigma_{xy1,xy4,xy2,xy3} = \frac{(F_y)}{A}, \quad (30)$$

$$\sigma_{y1,y4,y2,y3} = \sigma_{z1,z4,z2,z3} = 0. \quad (31)$$

Strain gauges 1 and 4 only measure strain in the x direction, and strain gauge 2 and 3 only measure strain in the z direction:

$$\varepsilon_{x1} = \frac{\sigma_{x1}}{E} + \varepsilon_{Temperature}, \quad (32)$$

$$\varepsilon_{z2} = -\nu \frac{(\sigma_{x2})}{E} + \varepsilon_{Temperature}, \quad (33)$$

$$\varepsilon_{z3} = -\nu \frac{(\sigma_{x3})}{E} + \varepsilon_{Temperature}, \quad (34)$$

$$\varepsilon_{x4} = \frac{\sigma_{x4}}{E} + \varepsilon_{Temperature}. \quad (35)$$

Simplifying yields the following relationships:

$$\varepsilon_{x1} - \varepsilon_{z2} + \varepsilon_{x4} - \varepsilon_{z3} = \frac{\sigma_{x1} + \nu\sigma_{x2} + \sigma_{x4} + \nu\sigma_{x3}}{E}, \quad (36)$$

$$\varepsilon_{x1} - \varepsilon_{z2} + \varepsilon_{x4} - \varepsilon_{z3} = \frac{-2F_x - 2\nu F_x}{AE}, \quad (37)$$

where  $\nu = 0.3$  for aluminum.

The Wheatstone bridge output is

$$\frac{\delta E_O}{E_i} = \frac{G.F.}{4} \left( \frac{-2.6F_x}{AE} \right), \quad (38)$$

where

$\delta E_o$  is the bridge output voltage,

$E_i$  is the bridge excitation voltage, and

$G.F.$  stands for the gauge factor.

As seen from above equation, this bridge configuration only measures axial force in the x direction.

The second bridge measures the strain experienced by the cantilever support due to the slurry friction force and eliminates the contribution of the axial forces due to pipe internal pressure. In a full bridge configuration shown in Figure 24, temperature compensation is performed automatically and sensitivity of the bridge output is maximized.

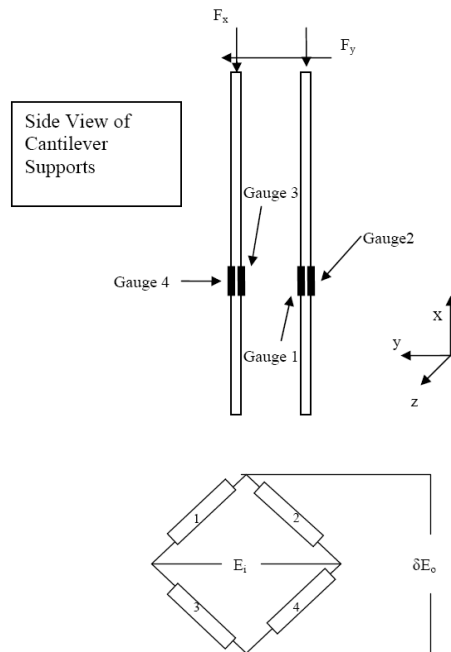


**Figure 24. Friction bridge strain gauge configuration**

Stresses at gauges 1, 2, 3 and 4 are:

$$\sigma_{x1} = \frac{(-F_y)(d_1)(y)}{I} + \frac{(-F_x)}{A}, \quad (39)$$

$$\sigma_{x4} = \frac{(-F_y)(d_2)(y)}{I} + \frac{(-F_x)}{A}, \quad (40)$$

$$\sigma_{x2} = \frac{(F_y)(d_1)(y)}{I} + \frac{(-F_x)}{A}, \quad (41)$$

$$\sigma_{x3} = \frac{(F_y)(d_2)(y)}{I} + \frac{(-F_x)}{A}, \quad (42)$$

$$\sigma_{xy1,xy4,xy2,xy3} = \frac{(F_y)}{A}, \quad (43)$$

$$\sigma_{y1,y4,y2,y3} = \sigma_{z1,z4,z2,z3} = 0. \quad (44)$$

Strain gauge 1, 2, 3 and 4 only measure strain in the x direction.

$$\varepsilon_{x1} = \frac{\sigma_{x1}}{E} + \varepsilon_{Temperature} \quad (45)$$

$$\varepsilon_{x2} = \frac{\sigma_{x2}}{E} + \varepsilon_{Temperature} \quad (46)$$

$$\varepsilon_{x3} = \frac{\sigma_{x3}}{E} + \varepsilon_{Temperature} \quad (47)$$

$$\varepsilon_{x4} = \frac{\sigma_{x4}}{E} + \varepsilon_{Temperature} \quad (48)$$

$$\varepsilon_{x1} - \varepsilon_{x2} + \varepsilon_{x4} - \varepsilon_{x3} = \frac{\sigma_{x1} - \sigma_{x2} + \sigma_{x4} - \sigma_{x3}}{E} \quad (49)$$

$$\varepsilon_{x1} - \varepsilon_{x2} + \varepsilon_{x4} - \varepsilon_{x3} = \frac{(-2F_y)(d_1)(y) + (-2F_y)(d_2)(y)}{IE} \quad (50)$$

By assuming  $d1 = d2 = d$ , we write

$$\frac{\delta E_O}{E_i} = \frac{G.F.}{4} \left( \frac{-4F_y(d)(y)}{IE} \right) \quad (51)$$

As seen from above equation, this bridge configuration only measures force due to shear in the y direction.

### 3.6. Hydrostatic Test

In order to ensure safe operation of the floating element assembly and the clear PVC pipe sections during pipe loop testing, it was decided to hydrostatically test the system. Hydrostatic testing of vessels and piping is a common way to test the integrity of the equipment before it is put online in order to detect faults in the material which may cause the equipment to fail or even explode during operation. The floating element assembly was filled with water and hydrostatically tested using nitrogen to 210 psig. The hydrostatic test pressure was chosen to be twice the operating maximum pressure which was approximated to be around 105 psig. The integrity of the assembly was examined during the hydrostatic test to ensure that the assembly is not going to fail during experimentation. The integrity of the assembly was verified since all components remained in good condition after the test. The clear PVC sections were also tested to the same pressures by following the same hydrostatic test procedure explained above.

### 3.7. Calibration

A custom built strain gauge conditioner identical to Vishay model 2100 was used to balance the axial and shear strain gauge bridges installed on the floating element cantilever supports. Bridge balancing is needed due to slight variations in the resistances of the strain gauges installed on both of the axial and friction Wheatstone full bridges. A four-wire full bridge method for connecting wires was used. The strain gauge conditioner contains two channels with separate circuits. Each channel was used to balance one of the strain gauge bridges. Each channel on the strain

gauge conditioner contains a variable resistor which is placed in parallel with one of the strain gauges. The variable resistor resistance can be varied until the bridge output is balanced. Moreover, each channel on the strain gauge conditioner contains an output voltage variable amplifier with a gain range between 0 and 2100. The output voltage of each of the strain gauge bridges was measured using a volt meter.

Since the floating element sensor deflects in response to axial and friction forces, some cross channel interference occurs between the axial bridge and the friction bridge outputs. In order to account for this interference in the results, a combination of axial and shear forces were applied to calibrate the floating element sensor.

Hydrostatic testing was done on the floating element assembly to ensure that it would not leak under the maximum pressure for the pipe loop system. Then, the floating element was calibrated using known weights applied in both shear and axial loading at the center of the floating wear sample as shown in Figure 25. A magnet was placed in the center of the wear sample top surface to ensure that force direction remained constant as the forces are varied. First, the bridge output was balanced, and then a set of weights of known masses were placed on top of the magnet for axial loading. To apply shear loads, additional weights were placed on a weight holder connected to the side of the magnet by a string parallel to the wear sample holder and passing through a pulley.

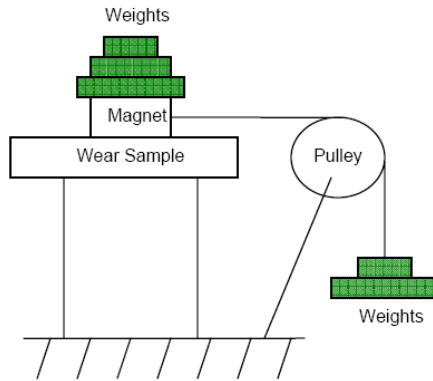


**Figure 25. Diagram showing forces applied to wear sample surface during calibration**

A table of the forces applied is shown in Table 1.

Axial force	0 N		0.491 N		0.981 N		1.472 N		1.962 N		2.943 N		3.924 N	
Shear force	shear	axial												
0 N	0.001	0.005	0.019	-0.002	0.021	-0.006	0.024	-0.013	0.027	-0.019	0.033	-0.029	0.039	-0.039
0.491 N	0.417	-0.007	0.425	-0.012	0.430	-0.016	0.434	-0.021	0.442	-0.024	0.450	-0.035	0.457	-0.044
0.981 N	0.842	-0.017	0.852	-0.021	0.860	-0.028	0.867	-0.033	0.873	-0.038	0.883	-0.049	0.895	-0.058
1.472 N	1.274	-0.036	1.284	-0.041	1.293	-0.046	1.301	-0.051	1.307	-0.057	1.322	-0.067	1.336	-0.077
1.962 N	1.705	-0.058	1.717	-0.063	1.726	-0.067	1.744	-0.075	1.756	-0.079	1.774	-0.091	1.789	-0.101
2.943 N	2.572	-0.115	2.587	-0.121	2.602	-0.126	2.620	-0.131	2.632	-0.137	2.651	-0.148	2.676	-0.160

**Table 1. Floating element sensor calibration results**

The initial gain setting of the axial Wheatstone full bridge was 1020, while the friction Wheatstone full bridge setting was set to 500.

The calibration matrix ( $C$ ) was obtained from the output voltage matrix ( $X_{OUTPUT}$ ) and the input force matrix ( $X_{INPUT}$ ) using Equation 52:

$$X_{OUTPUT} = C * X_{INPUT} \quad (52)$$

$$C = \begin{bmatrix} 0.879 & 0.0117 \\ -0.036 & -0.072 \end{bmatrix}$$

The Moore-Penrose pseudo inverse of the calibration matrix  $C'$  was used obtained which produces a matrix of the same dimensions as  $A$ . The pseudo inverse is commonly used in calibration since this method removes any singular values and treats these numbers as zeros.

$$C' = \begin{bmatrix} 1.218 & 1.974 \\ -6.055 & -147.772 \end{bmatrix}$$

A repeatability test was also conducted and 2% deviation in the axial direction and 0.2% deviation in the shear direction were obtained from five sets of data taken at the same axial and shear force of 1.962N.

The floating element was now ready for installation and testing in a flow loop.

## 4 Floating Element Output Measurements and Interpretations

### 4.1. Preliminary Test Setup

Syncrude Canada Ltd. has a 76.2 mm slurry test loop at its Edmonton Research Centre. This slurry loop was mainly used for slurry pump wear testing in the past and it is currently being utilized for other slurry flow tests. Due to delays in the commissioning of the University of Alberta pipe loop, it was decided to conduct preliminary testing of the floating element assembly on Syncrude's 76.2 mm nominal diameter pipe loop. The piping was constructed out of commercially available SA-106 Gr. B seamless carbon steel pipe, commonly used in industrial applications for pipe this size. Figure 26 shows Syncrude's slurry loop process diagram.

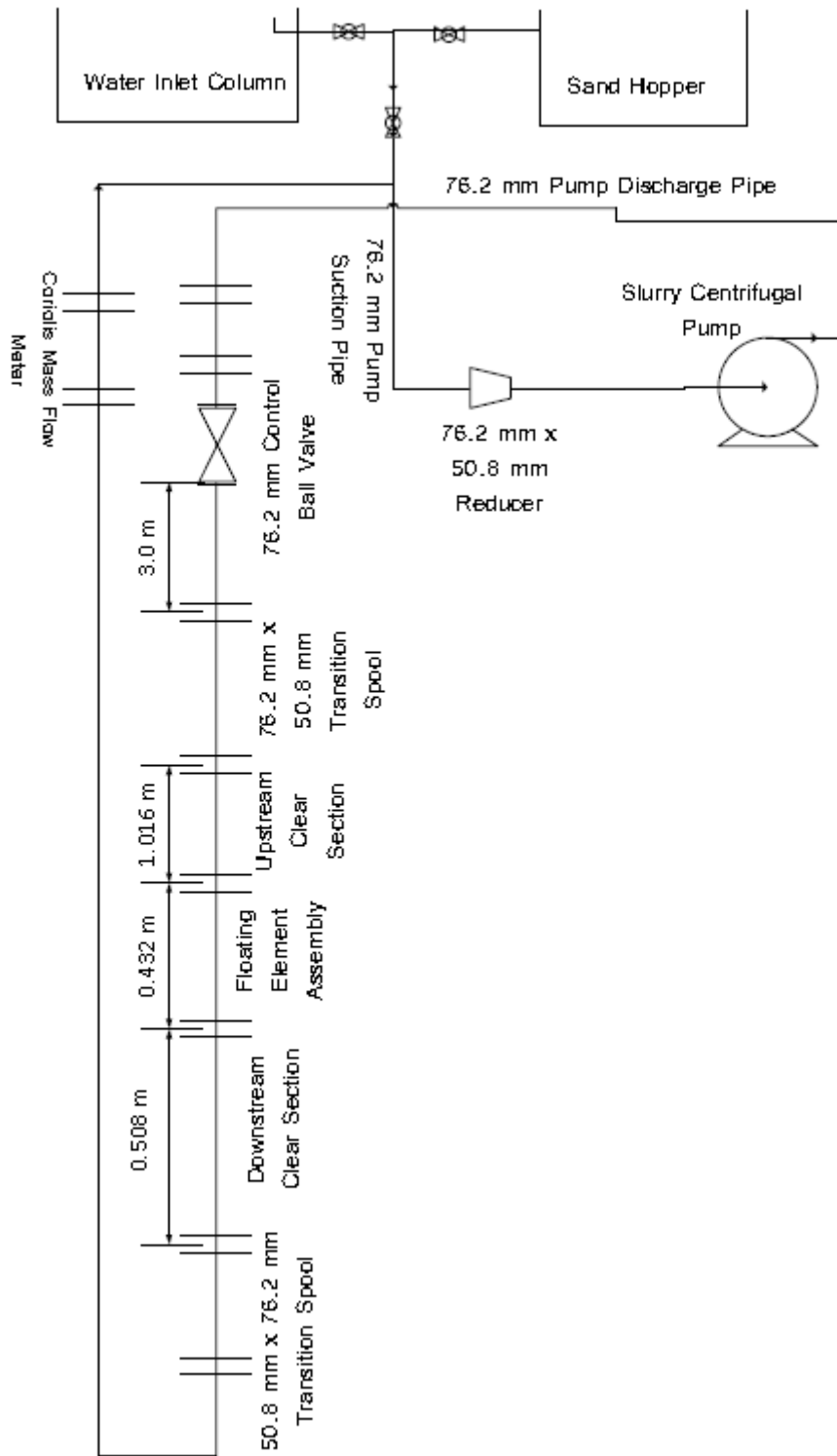


Figure 26. Syncrude slurry loop process diagram (not to scale)

The Syncrude slurry test loop consists of the following major components:

- 1) 3/2 AH Warman gland sealed belt driven centrifugal pump  
(Maximum rated rpm = 3170 rpm)
- 2) 40 HP Hyundai heavy duty AC motor equipped with variable frequency drive
- 3) 3" Sa-106 Gr. B schedule 40 process pipe c/w 3" 150# ANSI flanges
- 4) Coriolis Krohne flow meter
- 5) Venturi flow meter
- 6) Sand hopper with 2" outlet valve
- 7) Water inlet column
- 8) 3" 150# control ball valve located in the main pipe run
- 9) Pressure and temperature transducers
- 10) PLC control panel
- 11) National Instruments data acquisition system.

A photo of the main pumping system is shown in Figure 27:



**Figure 27. Photo of Syncrude research slurry loop main components**

## 4.2. Commissioning

In order to accommodate the 50.8 mm pipe of the floating element assembly, piping modifications were made to the existing 76.2 mm nominal diameter slurry loop. Since the floating element assembly nominal pipe diameter is 50.8 mm, two transition spools were designed to accommodate the change in pipe diameter. The two transition pipe spools were fabricated out of SA-106 Gr. B pipe identical to the rest of the loop pipe construction material. These transition pipe spools were installed upstream and downstream of the clear PVC sections as shown in Figure 28.

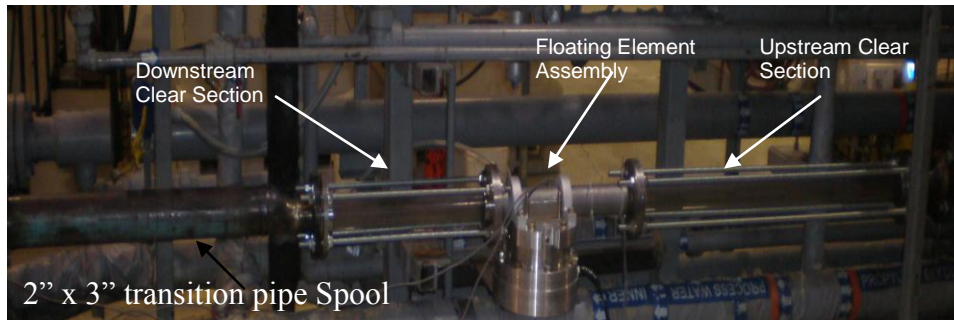


**Figure 28. Photo of floating element assembly and clear section at Syncrude Research**

Once the transition spools were fabricated, a section of the 76.2 mm pipe loop was removed and replaced with the floating element assembly along with the clear sections and the transition spools. The 76.2 mm x 50.8 mm transition spool was installed first and the 1016 mm long clear section was installed followed by the floating element assembly. The 508 mm long clear section was installed downstream of the floating element assembly followed by the 50.8 mm x 76.2 mm transition spool. Gaskets were placed in between of the flanged connections in order to prevent any leaks between the flange faces.

As all flanged connections were tightened, the piping system was filled with water from the inlet water column by opening the water inlet column valve. All small leaks were fixed by tightening the flange bolts. Once all connections were fastened tightly, the piping system vent valve was opened to remove air from the piping system and allow water to fill up the piping system faster. After the piping system was deaerated, the pump was started at low rpm with the pipe vents closed to circulate the water in the piping system. Water was also allowed to flow from the inlet water column. The piping vent was opened intermittently to permit any remaining air trapped in the piping system to escape.

Once the system was tested again for leaks and checked for any problems, the electrical wires coming out of the floating element sensor strain gauges were connected to the strain gauge conditioner input. Channel 1 on the strain gauge conditioner was used for axial bridge and channel 2 was used for the shear strain gauge conditioner. After balancing both bridge outputs, tests with water flow were conducted.

Before the introduction of sand into the piping system, the flush water valve was opened in order to prevent sand from entering through the gap between the floating element and the pipe. The optimal flush water supply rate was calculated to be around 1.3 liters/min based on the sand settling velocity. Since the gap width around the element is non-uniform, a safety factor was included in the calculations in order to minimize the amount of sand entering through the gap with minimal disturbance to the bulk slurry flow. Consequently, flush water tests were conducted and all data was recorded.

After finishing with water testing, sand was added to the sand hopper. The isolation valve between the sand hopper and the piping system was opened to allow for the sand to be sucked into the pipe loop. The sand was then mixed from water introduced in the sand hopper due to the opening of the isolation valve. Finally, slurry tests were conducted.

The mean particle size diameter was calculated and found to be 0.27 mm based on the sand supplier data sheet. The particle size distribution of the sand used can be found in the Appendix. The gap size of 0.75 mm is three times greater than the sand mean particle diameter and as a result there is little chance of sand plugging the gap between the wear sample and the pipe.

The system was commissioned successfully and with minimal problems. After testing with slurry bulk flow was completed, the slurry mixture was drained and the system was flushed several times with water to clean the piping system.

### 4.3. Preliminary Test Procedure

During first round of preliminary testing, the inlet water column was filled with water and pumped through the test loop. Air pockets present in the pipe loop were removed by constantly venting the system before data logging. The vent is located at the top of the pipe upstream of the pump suction flange. Once the air pockets in the piping system were eliminated, the vent was closed and the pump was turned off. Both the axial and shear bridge outputs were balanced using the strain gauge conditioner with no flow in the piping system. Once bridge balancing was completed for each test, the pump was turned on and data acquisition was started.

#### 4.3.1. Test #1

Test #1 was conducted with water flow and no flush water supply. The volume flow rate of water was varied by changing the rpm of the pump motor. The motor is equipped with a variable frequency drive that can be controlled from the control panel located next to the motor. The water bulk flow rate was increased from 0 USGPM to 250 USGPM and then decreased back down to 0 USGPM with known increments. At each flow rate set point, the flow was allowed to stabilize (for approximately 5 seconds) before moving to the next rpm set point while continuously logging data. It was determined that the flow has stabilized when the change in flow rate was less than +/- 0.5 USGPM. The output voltages

produced by the shear and axial full Wheatstone bridges were recorded for the total duration of the test, in addition to the volume flow rate, density, temperature, pump rpm, and pump discharge pressure.

#### 4.3.2. Test #2

Test #2 was a repeatability test to assess the variation in measured data. The measured flow rate was varied from 0 to 136 USGPM and then back to 0 USGPM again. This process was repeated one more time while continuously recording the shear and axial full Wheatstone bridges, volume flow rate, density, temperature, pump rpm, and pump discharge pressure.

#### 4.3.3. Test #3

During second round of preliminary testing, fully suspended heterogeneous sand slurry was pumped through the test loop at average flow rates between 110 and 220 USGPM. At the start of the test, the floating element assembly was removed from the piping system and inspected to ensure no sand was present in the chamber of the assembly. The assembly was cleaned and reinstalled, and both axial and shear bridge outputs were balanced at 0 USGPM bulk flow. Due to limited inventory of silica sand at Syncrude research facility, recycled sand previously used in G65 wear tests was used during test #3. The sand mean particle diameter was calculated by plotting the cumulative percent retained versus aperture opening size in mm and it was included in Appendix. The resulting calculated  $d_{50}$  of sand used was equal to 0.270 mm based on product data sheet supplied by the sand supplier (The product data sheet represents average properties of the sand).

The flushing water needle valve was set to 2 turns during test #3. This valve position was determined to be the optimum set point to reduce the amount of sand passing through the gap between the floating element and the pipe wall.

The average slurry density was estimated by recording the volume of sand added to the piping system and by measuring the effective volume of the slurry loop. The slurry volume flow rate was monitored by a Venturi flow meter since the Coriolis flow meter was not designed to measure flow densities above 1130 kg/m<sup>3</sup>. Slurry pump discharge pressure, flow temperature, pump rpm, friction and axial bridge outputs were recorded during test duration. The volume flow rate of the fully suspended sand slurry was varied between 108 and 210 USGPM with known increments. The slurry flow was then decreased to 108 USGPM at the end of the test, and then the pump was shut off.

Preventing sand particles from entering the floating element chamber is important to ensure its operation for extended periods of time. The sand settling velocity was calculated based on the particle mean diameter using dimensionless Archimedes number to eliminate the need for iteration to calculate the drag coefficient required at high Reynolds number.

Archimedes number can be calculated as follows:

$$Ar = \frac{4dp^3 \rho_l (\rho_s - \rho_l) g}{3\mu_l^2} \quad (53)$$

where,

$$dp = 0.3 \times 10^{-3} \text{ m}$$

$$\rho_l = 992 \text{ kg/m}^3 [33]$$

$$\rho_s = 2650 \text{ kg/m}^3$$

$$g = 9.81 \text{ m/s}^2$$

$$\mu = 0.653 \text{ mPa.s for flush water at 40C [33]}$$

$$Ar = 1362$$

For sand particles, a relationship was developed by Saskatchewan Research Council for calculating the sand particle drag coefficient ( $C_d$ ) as follows:

$$C_d = a_1(Ar\#)^{b_1} \quad (54)$$

where,

$$a_1 = 80.9 \text{ for } 24 < Ar < 2760$$

$$b_1 = -0.475 \text{ for } 24 < Ar < 2760$$

$$C_d = 2.62$$

An equation for calculating terminal velocity ( $V_\infty$ ) in a liquid was developed and as a result calculation of the terminal velocity is possible on the drag coefficient is calculated as follows:

$$V_\infty = \left[ \left( \frac{4gd_{50}(\rho_s - \rho_l)}{3\rho_l C_d} \right) \right]^{0.5} \quad (55)$$

$$= 0.05 \text{ m/s}$$

$$\text{Area of the gap around the element} = 1905 * 10^{-7} \text{ m}^2$$

$$\text{Required flow rate} = V_\infty * \text{Area of gap} \quad (56)$$

$$= 95 * 10^{-7} \text{ m}^3/\text{sec} = 10 \text{ gph}$$

The terminal velocity was calculated for an assumed sand particle diameter of 300  $\mu\text{m}$  since a sieve analysis was not performed on the test sand used at the time of test #3. The calculated sand terminal velocity was 0.05 m/sec and the required flush water supply flow rate was 10 gph (0.65 liters/min).

Due to small variation in the gap width around the floating element sensor and in flush water supply pressure, back pressure, and flow rate, the set point for flush supply flow rate was chosen as 20 gph ( 1.3 liters/min) giving a safety factor of 2. Flush water flow rate curves were constructed based on a flush water supply pressure of 33 psi and using a calculated needle valve flow coefficient as shown in Figure 29. Sample calculations of the needle valve flow coefficient can be found in Appendix. According to the needle valve flow curves the needle valve optimal setting is at 2 turns assuming a back pressure between 5 and 10 psi with a flush water supply pressure of 33 psi.

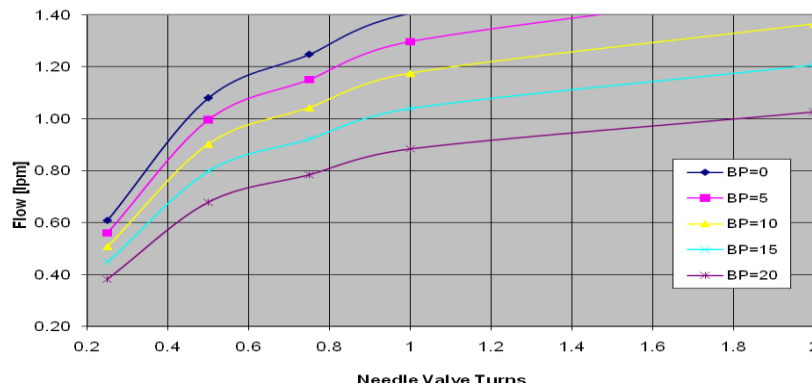


**Figure 29. Needle valve flow curves for corresponding back pressure in psig**

Test conditions were summarized in Table 2.

Test #	Description	Flow rate USGPM	Density Kg/m <sup>3</sup>	d <sub>50</sub> mm	Velocity m/s
1	Water Flow	0 to 250	1014	N/A	0 to 7.3
2	Repeatability	0 to 136	1014	N/A	0 to 4.0
3	Slurry Flow	110 to 220	1350	0.27	3.2 to 6.4

Table 2. Tests Summary

The measured bulk flow rate can be easily converted to velocity by multiplying the flow rate with the internal area of the pipe. The internal area of the 50.8 mm pipe used is 0.002165 m<sup>2</sup>.

#### 4.4. Preliminary Testing Results

##### 4.4.1. Observations and Summary of Results

During test #1, the temperature of water flow remained relatively constant and increased slightly from 21.4 to 21.6 °C due to circulation of the flow within the pipe loop from discharge back to suction through a heat exchanger. The heat exchanger cooling water supply was closed since cooling of the flow was not necessary for this test. As a result of the constant water flow temperature, water density measured by the Coriolis flow meter also remained constant at around 1014 kg/m<sup>3</sup> on average.

The water flow rate in the piping system was indirectly controlled via the variable frequency drive that controls the pump speed. Since the flow rate was controlled via the pump impeller rotational speed, transient flow conditions occurred in the pipe loop as the pump speed was varied. At constant pump speed, the flow in the loop stabilizes quickly; and, as a result, steady-state conditions exist in the pipe loop after a relatively small

time (less than 5 seconds) of keeping the pump rpm constant. The flow rate of the water flowing through the pipe loop followed the same trend as the rpm.

The water friction force was plotted for the duration of test #1 using the calibration matrix and the axial and friction output voltage as shown in Figure 30. As expected, the measured water friction force increases with increasing flow rate while the density and temperature of the fluid remain constant. During transient flow conditions the measured friction force responded quickly showing clearly the change in the force magnitude.

As the flow rate was increased from 0 to 250 USGPM, the measured friction force magnitude increased from 0 N to a maximum of about 0.43 N. The flow rate was then decreased to 0 USGPM, and the final zero point was plotted on the graph. As seen from the graph, the maximum variability in the friction force measurement at constant flow rate is 0.06 N.

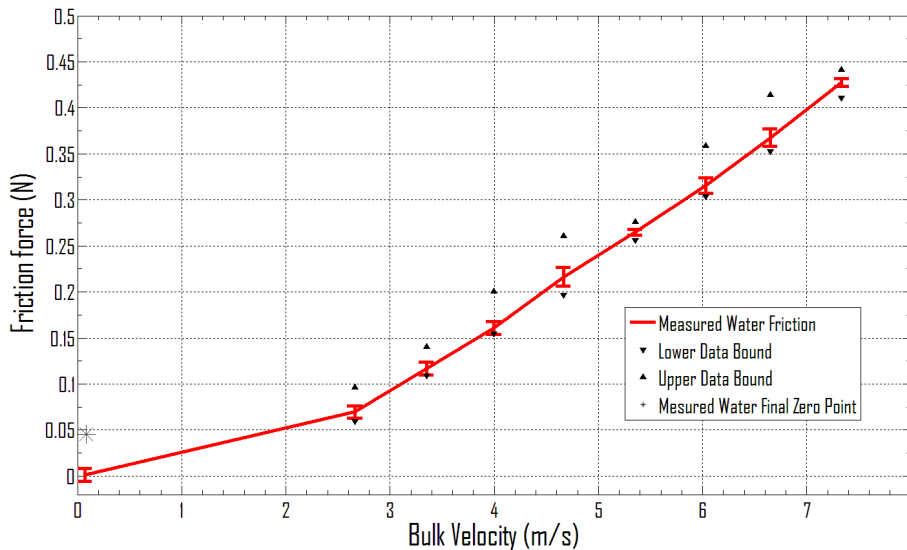


**Figure 30. Plot of measured water friction force versus bulk velocity**

Similarly, the axial force acting on the floating element wear sample was measured and plotted on Figure 31 for the duration of test #1 using the calibration matrix and the axial and friction output voltage. The axial force increased with increasing system flow rate as the pump speed was increased due to increasing magnitude of flow turbulence. The measured axial force responded quickly to transient conditions during pump speed variation. The axial force acting on the floating element was compressive force and increased from 0 N up to 10N as the flow rate was increased from 0 to 250 USGPM. Water flow rate was decreased gradually to 0 USGPM and the final zero point was also recorded and plotted on the graph. As seen from the graph in Figure 31, the maximum variability in the axial force measurement at constant flow rate is 1.5 N.

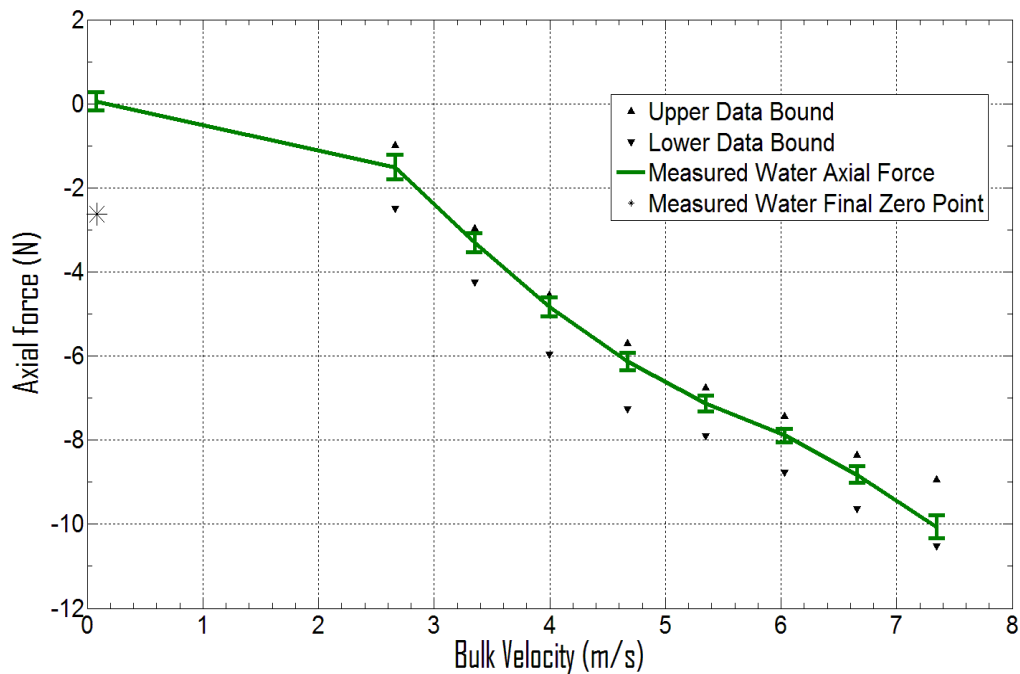


**Figure 31. Plot of measured water axial force versus bulk velocity**

The difference between the starting zero point and the final zero point is due to a small drift in both of the axial and friction bridge sensor output. The observed drift in the axial bridge was approximately 2.5 N while the drift in the friction bridge was about 0.05 N at the end of the test. The drift

in the data was reproducible and the bridge output was balanced after the test to remove the drift in the signal output.

During test #3, sand was added to the sand hopper located upstream of the pump suction. The sand was mixed with water in the sand hopper, and sand particles were introduced into the piping system. By adding 150 kg of sand to the piping system, the density of the slurry sand mixture increased to  $1350 \text{ kg/m}^3$ . No additional sand was added during the data acquisition period and the slurry density remained constant during the test duration.

Unfortunately, as the mixture density was increased above  $1130 \text{ kg/m}^3$ , the KROHNE Coriolis flow meter stopped measuring density and flow rates because it was not designed to handle high slurry densities with the current configuration. Instead of the Coriolis flow meter, slurry density was calculated based on the mass of sand added to the flow loop and the volume of water in the loop. Sample calculations of the density calculations are found in Appendix. The slurry flow rates were measured using an existing Venturi flow meter. The temperature of the slurry bulk flow increased slightly from  $26.8 \text{ }^\circ\text{C}$  at the start of the test to  $28.2 \text{ }^\circ\text{C}$  at the end.

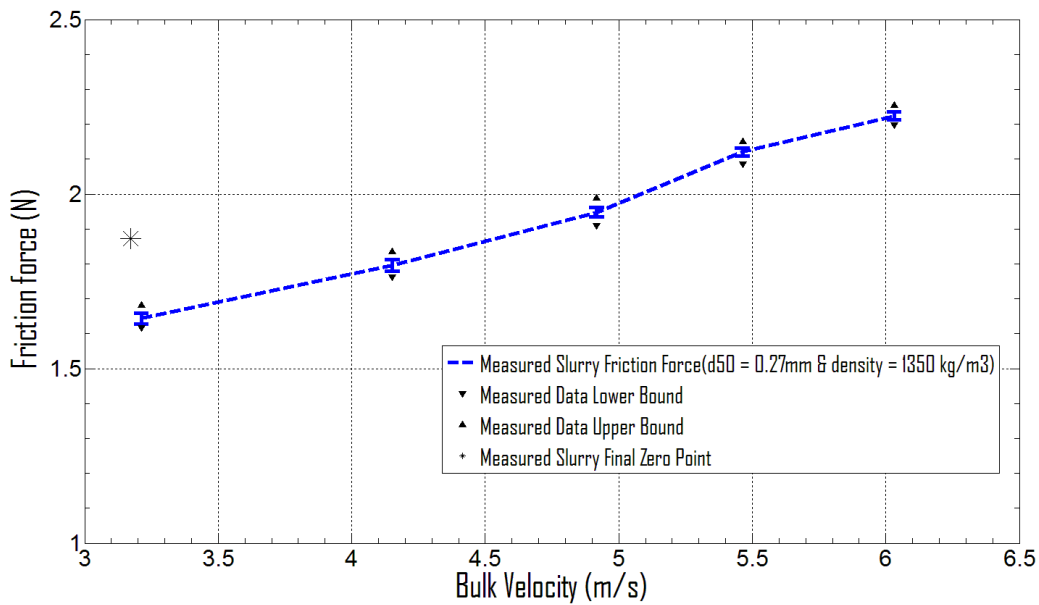


**Figure 32. Plot of measured slurry friction force versus bulk velocity**

Similar to test #1, the friction force was measured for the duration of test #3 as shown in Figure 32. It was found that the friction increases with increasing flow rate as expected. During transient flow conditions the measured friction force responded quickly showing clearly the change in the force magnitude. In order to avoid plugging of the slurry loop pipe during the testing period, the velocity of the pipe in the 3 inch section was always kept above the sand deposition velocity. The sand deposition velocity was estimated to be 1.5 m/s based on previous experience. As a result, it was decided to keep the slurry flow rate in the piping system above 110 USGPM at all times during operation. At this flow rate, the flow velocity in the 2" test section is 3.2 m/s, and bed flow conditions were not observed in this test.

The measured friction force magnitude started at 1.6 N at 110 USGPM water flow and increased to a maximum of 2.25 N at 220 USGPM. The flow rate was then decreased back to 110 USGPM, and the final zero point was plotted on the graph. The maximum variability in the friction

force measurement at constant flow rate is 0.1 N. The difference between the starting zero point and the final zero point is due to a small drift in both of the axial and friction bridge sensor output. There was a substantial increase in the measured slurry friction force compared to water flow in the same range of flow rates.

A problem encountered during this test was the fouling of the floating element assembly internal body with sand particles. Since the gap size is three times larger than the sand mean particle diameter some sand gets through the gap and settles to the bottom of the assembly over time during slurry testing. In order to ensure that fouling does not affect the axial and shear bridge output during slurry test, the pump was turned off to allow sand to settle to the bottom of the pipe and floating element assembly was removed from the pipe loop and cleaned before logging data. The amount of sand removed from the piping system during this process was considered minimal and as a result it does not affect the slurry density (less than 3 kg of sand).

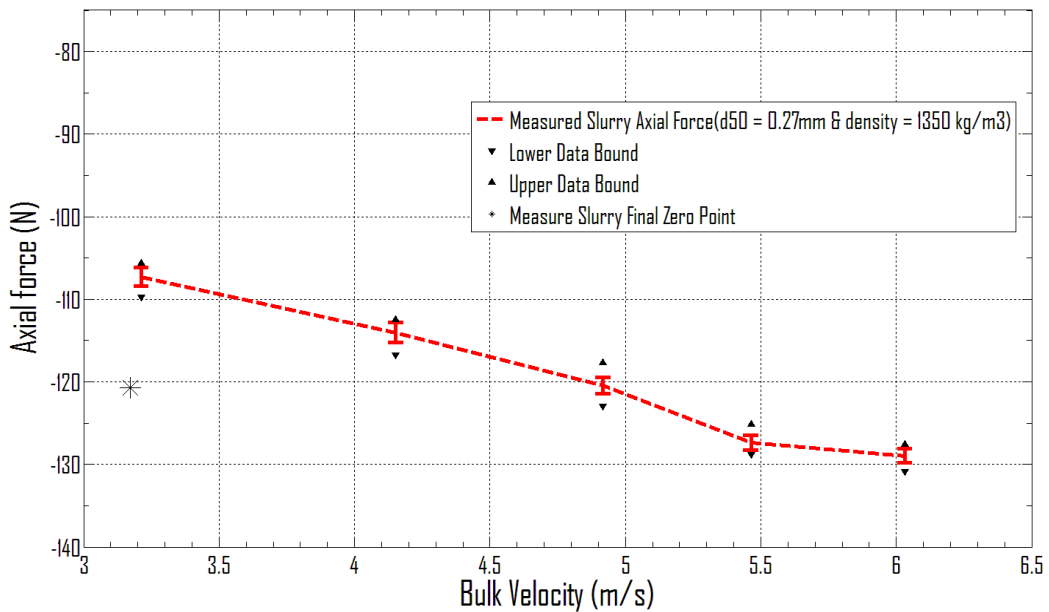


**Figure 33. Plot of measured slurry axial force versus bulk velocity**

Similarly, the axial force acting on the floating element wear sample due to slurry flow was measured and plotted on Figure 33. The compressive axial force increased with increasing system pressure as the pump speed was increased as expected similar to the water flow case. The increase in the axial force measured was more substantial compared to the water flow due to the increase in the mixing forces in the slurry flow and the number of impacts of sand particles with the pipe wall. The axial final zero point was also plotted on the same plot. The difference between the starting zero point and the final zero point is due to a small drift in both of the axial and friction bridge sensor output. The maximum variability in the slurry axial force measurement at constant flow rate is 5 N as shown in Figure 33. The axial force measured responded quickly to transient conditions during pump speed variation since the pump can be considered as a pressure source in the piping system.

Data points were connected to produce a plot of the pump discharge pressure versus bulk flow rate for water during test #1 as shown in Figure 34. The pump discharge pressure was increased during slurry testing as compared to water flow testing. The reason is that slurry density is much higher than the water density and as a result the pressure drop across the piping system is higher as predicted by the two-layer model. As a result, a higher pump discharge pressure is produced at the same water flow rates provided the motor does not run out of available power.

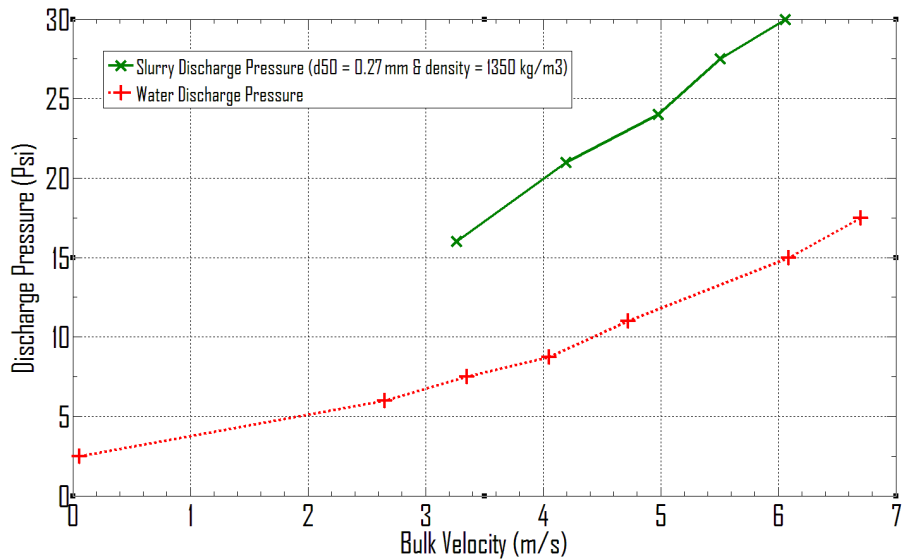


**Figure 34. Measured discharge pressure versus velocity**

#### 4.4.2. Comparison with Theoretical Results

Theoretical Kinematic stress due to water flow in the pipeline is given by Equation 57 below:

$$\tau_{kw} = 0.5\rho_w f_{fw} V^2 \quad (57)$$

where

$\rho_w$  is the density of water = 1014 kg/m<sup>3</sup>,

$f_{fw}$  is the water fanning friction factor, and

$V_w$  is the average water flow velocity.

Knowing the water density, velocity and the corresponding fanning friction factor, the kinematic stress at the pipe wall was calculated. Sample calculations of the water kinematic stress are included in Appendix. The theoretical friction force was then computed by multiplying the theoretical stress calculated by the area of the floating element wear sample in contact with the flow. The theoretical friction force and the measured friction force were plotted on the same graph in Figure 35.

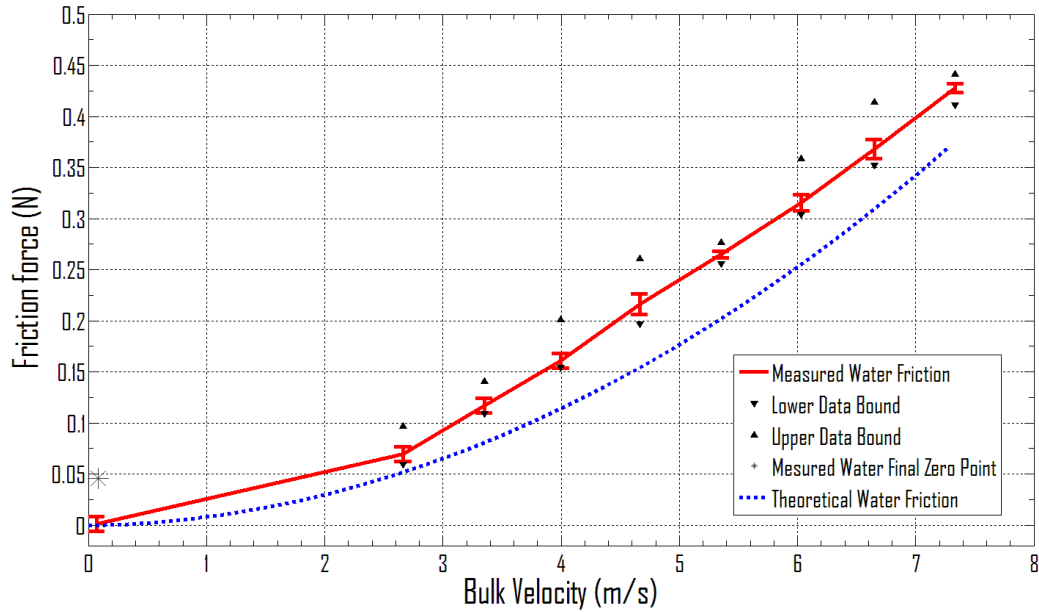


**Figure 35. Theoretical and measured water friction force versus flow rate**

The difference between the theoretical and measured water friction force can be attributed to several factors. First of all, the flow rate and density measurements made by the Coriolis flow meter might have been slightly off. Additional velocity and density measurements should be made in order to calculate the error in the Coriolis flow meter measurements. Moreover, the presence of the gap between the floating element wear sample and the pipe might have contributed to some discrepancy in the measurement. The error due to the presence of the gap was not quantified. The viscosity of water in the theoretical calculations was approximated to be 0.001 Pa.s for water at 20 °C.

Similarly, the theoretical kinematic stress due to slurry flow in the pipeline was calculated by using Equation 58 below [17]:

$$\tau_{kw} = 0.5\rho_w f_{fw} V^2 + 0.5\rho_s f_{fs} V^2 \quad (58)$$

where,

$\rho_w$  is the density of water = 1014 kg/m<sup>3</sup> at the average testing temperature

$f_{fw}$  is the water fanning friction factor

$\rho_s$  is the density of sand particles = 2650 kg/m<sup>3</sup>

$f_{fs}$  is the friction factor computed using the two-layer model

$v$  is the slurry flow velocity in the bottom layer of the flow

According to the two-layer model, the kinematic stress experienced by the flow is increased due to the presence of slurry solid particles in the mixture. The additional contribution to the kinematic stress can be computed by calculating a modified friction factor  $f_{fs}$  as shown in the Appendix. The mean diameter of sand particle size distribution used was 0.27 mm. Sample calculations of the theoretical kinematic stress due to slurry flow are given in Appendix. The slurry flow theoretical friction force was then calculated by multiplying the surface area of the floating element wear sample in contact with the flow with the computed theoretical kinematic stress. A plot showing the slurry flow theoretical and measured friction force is shown in Figure 36.

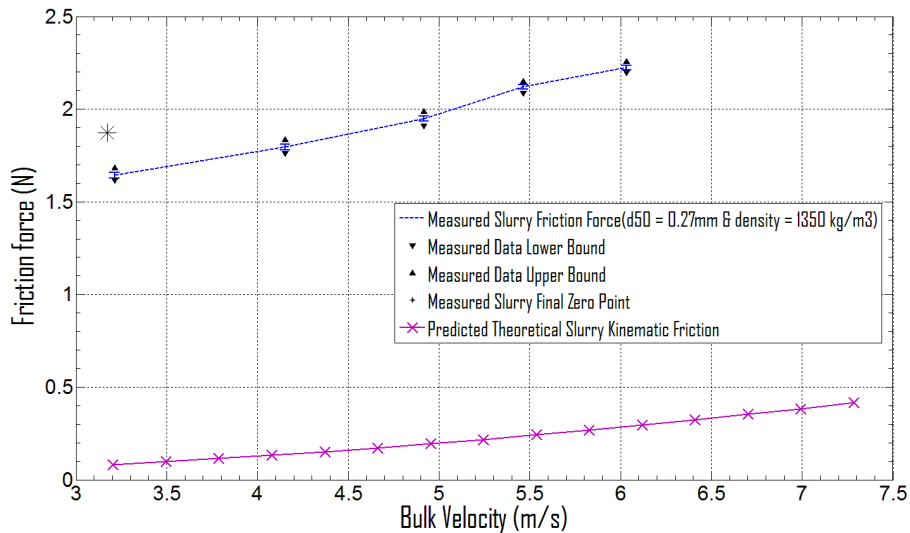


**Figure 36. Theoretical and measured slurry friction force versus flow rate**

The measured slurry friction force is high for the measured flow conditions compared to the friction force calculated from the kinematic stress based on the two-layer model. The presence of the gap between the floating element wear sample and the pipe has contributed to unaccounted discrepancy in the measurement. Fouling of the assembly and the flow of flush water through the gap have contributed to error in the measurements which was not quantified. These predicted sources of error are considered to be the main sources of error in the measurements made.

Due to Coriolis flow meter malfunctioning at higher slurry densities, flow rate was measured using a backup Venturi flow meter. The flow rate measurement of the Venturi meter was known to be slightly in error, according to the operators. The Venturi flow rate measurement was corrected for slurry flow but the measurement accuracy is questionable. First of all, the slurry flow rate was measured using a Venturi flow meter which is calibrated to measure water flows. Second, this meter was known to be giving slightly erroneous measurements compared to the Coriolis output for the same water flow rate. The measured slurry friction force was 10 times higher than the theoretical friction force. Since the area of the element is constant, the measured kinematic stress acting on the floating element is 10 times higher than the theoretical kinematic stress. The required flow rate has to be 2.23 times the measured flow rate in the pipe loop to produce the same stress level experience by the floating element sensor. This is not possible since the error in the flow measurement can not possibly be this high. The decrease in water viscosity due to test temperature increase during testing is small and as a result its affect on the kinematic stress value is also considered negligible. It was assumed that the errors in the  $f_{fs}$  and  $f_{fw}$  are negligible relative to the error in the flow rate measurement and thus can be safely neglected. Also, it was assumed that the error in the solids density and carrier fluid density is

negligible. Additional velocity and concentration profile measurements should be made during future testing in order to verify the floating element friction measurements.

On the other hand, it is important to mention that the floating element sensor measures both axial and shear forces at the same time. As a result, cross channel interference occurs between the axial and shear bridges. Errors in the axial bridge measurement get transferred due to cross-channel interference to the shear bridge output. Consequently, the design of the floating element should be modified to conduct the axial and shear force measurements separately.

Cross channel interference error can be attributed to the pressure drop across the floating element sensor which applies an axial load. The axial load applied causes errors in the axial and friction force measurement because the element was calibrated using a combination of axial and shear loads. The pressure drop across the floating element wear sample during slurry flow is estimated to be 600 Pa using the two layer model equation at 220 USGPM flow rate. This pressure drop causes an additional axial force equal to 1.8 N knowing that the surface area of the floating wear sample is  $0.003 \text{ m}^2$ . By inspection of calibration Table 1, the voltage difference due to the pressure drop is 0.019 V in the axial bridge and 0.027 V in the friction bridge which causes a maximum relative error in the bridge output equal to 3% in the axial bridge output and 15% in friction bridge output.

Post test calibration of the floating element sensor was conducted to make certain that the element was not damaged during testing. Initial visual inspection of the assembly indicated there was no visible damage done on the element since all the components were in good condition. The post calibration shear force results agreed with the pretest shear

calibration results as shown in Table 3. No axial force post test calibration was performed since it was in good condition.

Axial force	0 N	0.491 N	0.981 N	1.472 N	1.962 N	2.943 N	3.924 N
Shear force	shear	shear	shear	shear	shear	shear	shear
0 N	0.002	0.012	0.024	0.038	0.049	0.075	0.091
0.491 N	0.45	0.46	0.499	0.515	0.536	0.557	0.596
0.981 N	0.898	0.937	0.961	0.951	0.975	1.01	1.039
1.472 N	1.36	1.355	1.371	1.394	1.427	1.469	1.494
1.962 N	1.83	1.845	1.872	1.895	1.901	1.96	2
2.943 N	2.67	2.744	2.78	2.81	2.835	2.886	2.935

Table 3. Floating element sensor shear bridge post test calibration results

#### 4.4.3. Repeatability Results

During test #2, the friction force measured was repeatable with a standard deviation in the measured data equal to 4% as shown in Figure 37. The axial force output was less repeatable compared to the friction force with a calculated standard deviation equal to 5% as shown in Figure 38.

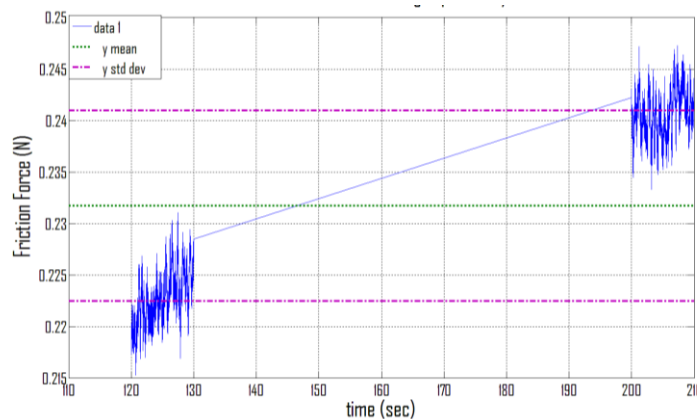
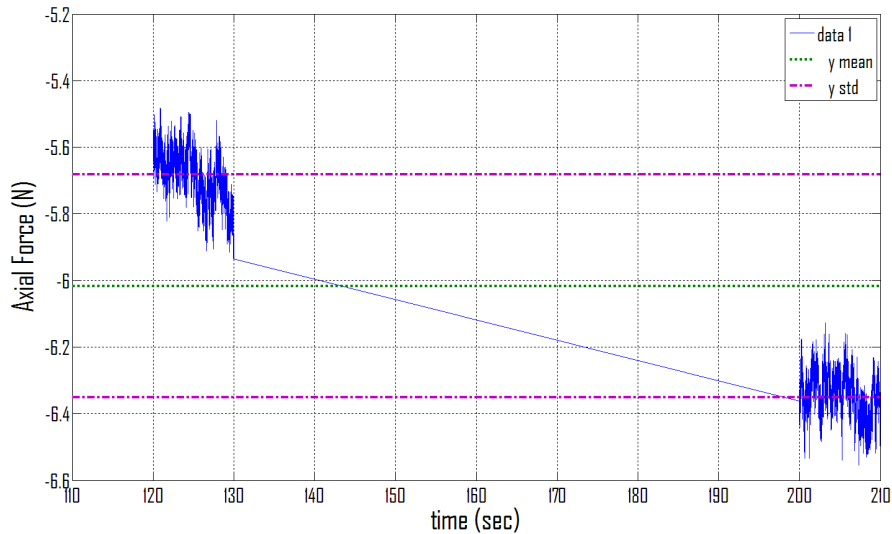


Figure 37. Friction force versus time during repeatability test #2

The high stiffness of the floating element in the axial direction causes lower repeatability in the measured axial bridge output relative to the

friction bridge output repeatability. It is important to note that the axial bridge does not respond as quickly as the friction bridge which can lead to low repeatability especially when conducting such a test with changing pump rpm relatively fast.



**Figure 38. Axial force versus time during repeatability test #2**

#### 4.4.4. Signal Processing

The floating element sensor deflects due to the action of the axial and friction forces acting on it. The strain measured at the bottom of the cantilever elements is converted to force magnitude using the force-voltage relationship obtained after calibration of the element. Both the axial and friction forces acting subject the sensor to fluctuations due to small variations in the force magnitude and directions. As a result, the floating element sensor measurements are affected by these excitations. It is important to check whether the magnitude of excitations experienced is close to the natural frequencies of the moving components inside assembly. If the magnitude of the excitations close to the lowest natural

frequency of the element is high, then oscillations can distort the signal and negatively affect the measurements. Since the element stiffness is high in the axial direction, its axial natural frequency is well above the frequency of axial fluctuations. As a result, resonance in the axial direction is not a concern. The natural frequency of the system can be calculated as shown in Equation 59 assuming the wear sample holder assembly can be represented by an undamped spring-mass system in the axial direction.

$$f_n = \frac{1}{2\pi} \sqrt{\frac{k}{m}} \quad (59)$$

where

$f_n$  is the natural frequency of the system (Hz),

$k$  is the stiffness (N/m), and

$m$  is the mass (kg).

On the other hand, the natural frequency of the element in the shear direction is potentially a concern because of the system flexibility in that direction and the large mass of the floating element itself. Consequently, the natural frequency of the moving components inside the assembly in the shear direction has to be determined in order to check for resonance. If the power of the signal at the natural frequency is relatively low, one can safely state that the output data is clean and not distorted. Alternatively, if the power of the signal is dominant at the natural frequency, then the design of the floating element sensor has to be modified in order to shift the natural frequency of the element outside of the measured range.

The natural frequency of the moving components of the floating element assembly was found by using a shaker table setup located in the Mechanical Engineering Building. The shaker table setup, as shown in Figure 39, consists of an articulating drum which vibrates a shaker table placed on a lubricated surface. The drum was rotated horizontally since

the natural frequency in the friction direction is of interest. The frequency of vibrations was varied until the first natural frequency of the element was found to be 38 Hz. Amplitude was controlled to avoid damaging the element. The power spectral density of the signal was utilized to find the magnitude of the fluctuation at the resonance frequency in the shear direction.



**Figure 39. A photo of the frequency test setup**

Both axial and shear bridge output signal were acquired at a data acquisition rate of 500 samples per second. A power spectral density (PSD) analysis of the friction bridge signal was developed in Matlab using Welch averaged spectral estimation method with several windowing functions such as Hanning, Blackman and Chebychev. The input signal was divided into segment sizes of 64 samples for all three window functions. A small sample size produces more averages resulting in smaller variances in the power spectral density plot. A default value of 50% overlap between segments in all three cases was also used. Figure

40 shows that each approach produced a slightly different plot for the signal at 190 USGPM. All plots appeared identical up to frequency of 20 Hz. After 20 Hz, the PSD plot using Chebyshev window showed the power spectrum without exhibiting apparent spectral leakage, and as a result it was chosen as the window of choice. Similar results were achieved for slurry and water flows at different flow rates.

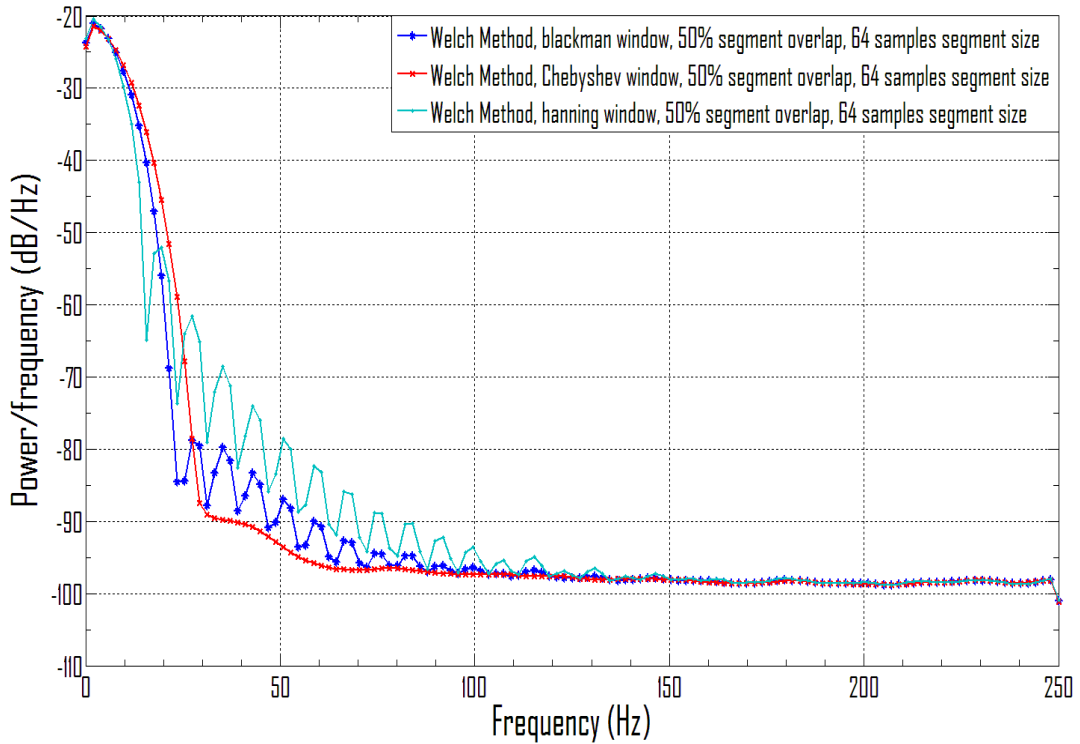


**Figure 40. Friction bridge power spectral density for slurry flow at 190 USGPM at t = 40 to 46 sec**

As shown in Figure 41, the peak of the power spectral density plot occurs at 5 Hz for the axial signal during water and slurry testing at 207 and 190 USGPM respectively. The power spectral density plot drops sharply after 10 Hz and reaches a minimum at 30 Hz as the plot flattens out. As a result, the signal dominant measurement fluctuations occur at around 5 Hz, which is well below the first natural frequency of the floating element in the axial directions as expected. Small amplitude fluctuations in the signal

occurring above 30 Hz are likely due to mechanical force fluctuations from turbulence or low angle impact of particles, or may be an artifact of the low-pass filtering.

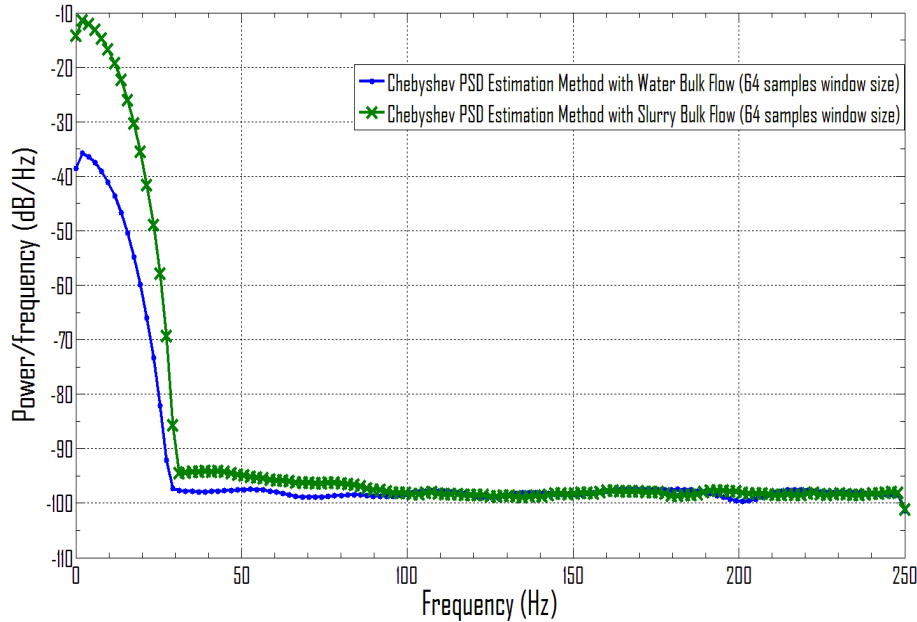


**Figure 41. Sample axial bridge power spectral density plot for both slurry and water flows at 190 USGPM and 207 USGPM respectively**

Similarly, the peak of the power spectral density plot occurs at 5 Hz for the friction signal during water and slurry testing as shown in Figure 42. The power spectral density plot drops sharply after 10 Hz and reaches a minimum at 30 Hz as the plot flattens out. Another small peak occurs at around 39 Hz due to the natural frequency of the floating element sensor. As a result, the amplitude of these fluctuations is amplified due to resonance resulting in another peak in the power spectral density. Fortunately, the magnitude of the latter peak due to resonance is very small compared to the dominant peak of fluctuation in the signal occurring at 5 Hz.

Consequently, it is safe to state that the signal measurements made in the friction direction are not distorted due to the natural frequency of the element. As a result, the signal dominant measurement fluctuations occur at around 5 Hz which is far away from the natural frequency of the floating element in the friction direction. Small amplitude fluctuations in the signal occurring above 30 Hz are likely due to mechanical force fluctuations from turbulence or low angle impact of particles.

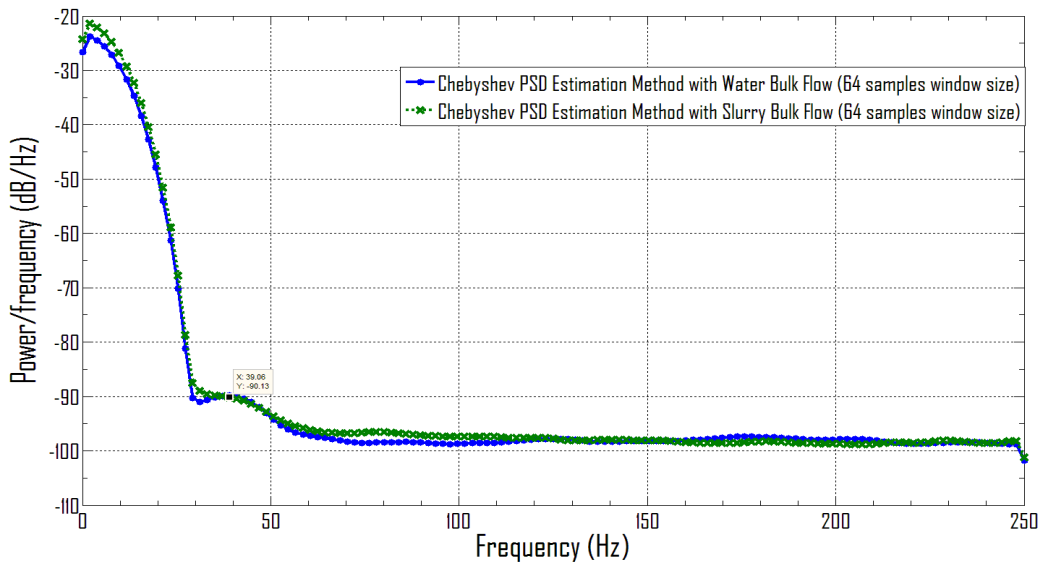


**Figure 42. Sample friction bridge power spectral density plot for both slurry and water flows at 190 USGPM and 207 USGPM respectively**

#### 4.5. Future Design Modifications

The 50.8 mm slurry wear test loop at the University of Alberta is currently being commissioned. The loop has been designed with a removable horizontal section to accommodate the floating element assembly and the clear sections. Once this loop is successfully commissioned, the floating element assembly can be installed incorporating some design

modifications to improve performance. Additional slurry testing can be performed just above sand deposition velocity and at higher slurry mixture concentrations (up to 35% by volume) with on-line wear measurements.

There are many ways to utilize the floating element sensor in future slurry wear testing. The construction material of the floating wear sample can be easily changed by making additional wear samples to replace the current SA-106 Gr. B wear sample. Soft materials such as polymers, harder materials such as titanium, and more advanced composite materials can replace the current construction of the floating element wear sample. The measured friction and axial force will be affected by the nature of the wear sample material, because each material has a unique friction factor. Moreover, the stress contribution due to random impact of particles against the floating wear sample will change depending on value of the coefficient of restitution between the impacting sand particles and the wear sample material. The contribution of random impact stress will be magnified or reduced relative to the base reference material depending on the wear sample material. The difference in the impact energy transferred to the floating wear sample can be used to identify the contribution of random impact of particles in the overall stress measurement. As a result, erosion wear due to random particle impact can be quantified and isolated from the other wear mechanisms.

The construction of the floating element assembly with flanges on both ends allows for rotation of the assembly to measure axial and friction forces at various locations around the pipe circumference. The measured axial and friction forces will change according to the circumferential location of the floating element sensor for the same slurry and flow conditions. This is due to the concentration and velocity profile across the pipe cross section unless the slurry is homogeneous. As a result, the

floating element sensor can be used to determine the contribution of each of the slurry erosion wear mechanisms around the pipe circumference. One of the challenges with the floating element design is to prevent or minimize the amount of sand that gets inside the main assembly. A good operational practice before and after each test is to drain sand trapped inside the floating element assembly by opening the drain valve while the slurry pump is off. Changing the drain size from 3/8" NPT to 1/2" NPT is recommended since sand particles can plug the drain valve. The drain connections downstream of the floating element assembly should also match the size of the drain outlet in order to prevent plugging with sand. It is also important to increase the size of the flush water inlet connections from 1/4" to 3/8" in order to allow for higher flush flow rates.

An area of improvement is to use an epoxy material to cover the strain gauges. The epoxy protective layer is more resistant to high temperatures than the wax currently used to protect the strain gauges. Wax starts to melt at flush water temperatures above 46 °C, limiting the flush water supply options. Additionally, wax can get distorted due to sand impingement. On the other hand, one of the disadvantages of using epoxy is the change in sensitivity of the strain measurement due to the added stiffness caused by using epoxy protective layer on the cantilever supports. Other options for a permanent but flexible protective covering should be considered.

#### 4.6. Considerations for Monitoring Wear

Additional flow and particle monitoring equipment can be employed to isolate the contribution of the wear mechanisms from each other. Additional equipment for estimating the velocity of particles before and after impacts, and the rate at which impacts occur may include a high-

speed camera at the clear section of the slurry loop. By using this technology to estimate change in velocity of particles after impacts, the momentum transfer to the pipe inner wall can be estimated, as well as the magnitude of energy transferred by random impact of particles. Other flow visualization techniques, such as introducing a boroscope into the flow, may give additional insight into the bulk slurry flow and particle flows near the wall. Moreover, acoustic emissions in the vicinity of the pipe wall can be recorded using a high-frequency microphone to capture the intensity of energy transferred to the pipe wall due to random impact of sand particles. Acoustic emission average power and event counts may correlate well with impact damage rate, and so this should be tested.

Online pipe thickness measurements can be conducted using an ultrasonic thickness measurement probe, which is current industrial practice. The duration of each test will vary depending on the floating wear sample material chosen and the sand particles erosive characteristics such as sharpness and hardness. The chosen ultrasonic thickness probe must have high accuracy and it must also be calibrated using a precisely machined pipe before actual pipe wear measurements to give absolute measurements as opposed to relative trends.

#### 4.7. Considerations for Scale-up to Larger Piping Systems

The amount of erosion thickness removed from the pipe is proportional to the energy transferred to the wall multiplied by the wear coefficient for each erosion wear mechanism [21]. The same approach used to predict erosion wear in a laboratory scale pipe loop can be applied to industrial scale pipeline. An industrial scale floating element assembly can be designed to be installed on larger diameter pipe; however, maintenance and operation of industrial scale floating element assembly is likely to be

expensive and impractical for long-term service. First of all, sand trapped in the assembly needs to be flushed and drained continuously before and after each measurement to ensure proper operation. Moreover, the durability of the strain gauge inside water and sand mixture is untested which may cause additional downtime.

For industrial scale implementation of the concepts presented in this work, a different and more practical approach must be taken to achieve better results. For example, strain gauges installed on the outside of the pipe wall can be used instead of the floating element assembly. Speckle interferometry technology for measuring pipe strain utilizing a reflected laser beam projected on the pipe wall should also be investigated. This will allow for measurement of stresses experienced by the pipe wall without interruptions to the operation of the pipeline. In order to measure deformation on the pipe wall, the strain gauges must also be arranged such that the axial hoop and friction shear strain can be measured separately. It is important to measure each axial and shear strain separately in order to prevent cross-channel interference if possible. Multiple strain gauge bridges can be utilized in order to reduce noise in the signal due to pipe vibration and to resolve the principle stresses at different locations to help to differentiate between loading due to impact stresses and abrasion versus normal process head loss. Additional measurements are needed to complete this work including differential pressure across the target pipe section, circumferential thickness profile of the pipe, and bulk flow rate. Temperature measurements should also be taken unless a temperature compensated method is utilized.

Once the stresses in large magnitude pipe are determined, similar relationships can be established for industrial scale applications and calibration of the strain gauges is needed. Moreover, strain gauges can be

installed on elbows and high wear locations within the pipeline in order to compare results obtained with results obtained from straight pipe sections.

Industrial scale implementation of the floating element assembly is impractical due to operational and maintenance issues. Different strain gauge configurations must be investigated and utilized instead of the floating element sensor on larger diameter pipes. Estimation of erosion wear coefficients for industrial scale pipe is required. The erosion wear model needs to be updated to account for digestion of oversized particles and bitumen conditioning flow processes which occurs in oilsands hydrotransport pipelines. As a result, tweaking of wear coefficients may be required. Operating pipe data also needs to be recorded. Monitoring of acoustic emissions in the vicinity of the pipeline should also be performed to track wear on-line. Acoustic emissions spectrum analysis can be used to determine damage signature frequencies from which pipe circumferential wear rates can be determined. Acoustic emissions will have to be recorded from multiple locations have to be done along the pipeline for data comparison. Separate monitoring for elbows, valves and pump discharge pipe spools is required since the flow conditions are altered during flow through these components. Recording of acoustic emissions needs to be performed periodically by operators along with other periodic preventative maintenance tasks. This will eliminate the need for a permanent acoustic emissions setup with dedicated instrumentation to transmit data wirelessly, a remote powering station, and a modification of the setup when the monitored pipe section needs to be replaced.

## 5 Conclusions and Recommendations for Future Work

### 5.1. Conclusions

A parametric model of erosion wear in a horizontal section of pipe under steady-state conditions for sand slurry flow has been presented. The model is established on a parametric lumped parameter representation of the physics of oilsands slurry flow in a straight section of pipe, based on the improved two-layer model. This erosion wear model can be augmented in future to embody erosion wear in oilsands straight horizontal section of pipe under steady-state conditions by including the contribution of bitumen and particle digestion to the total erosion wear. This model can also be further developed to include the effect of corrosion and corrosion-erosion wear mechanisms on the pipe wall.

In the lumped parameter erosion wear model presented, wear coefficients due to kinematic friction and random particle impact caused by slurry mixing in top and bottom flow layers can be lumped together to form one wear component in each top and bottom layer.

A floating element assembly was designed and tested to measure forces experienced by the pipe wall during slurry testing inside a straight pipe section. Two clear sections were also constructed out of PVC and they were installed upstream and downstream of the floating element assembly to observe the flow during testing. The floating element was calibrated and hydrostatically tested before commissioning and conducting tests with water and slurry flows. The results of the measured forces did not fully agree with theoretical results. The main sources of error were to fouling of the assembly, flush water flow, the presence of the gap.

The natural frequency of the floating element moving components was determined to be 38 Hz from a shaker table test, but it was determined that the main fluctuation of the floating element moving components occurs due to bulk flow at around 5 Hz, far away from the measured natural frequency.

The two main contributions in this thesis work are a formulation for a parametric model of slurry flow and modifying it for erosion wear for sand slurry in a straight section of pipe, and a prototype floating-element sensor for measuring forces on the wall of a slurry pipe. The wear model started from the physics of oilsands flow and developed a lumped parameter. The wear model can be applied for fully suspended heterogeneous slurry flow and heterogeneous slurry flow with a moving bed in a straight section of pipe. The parameters of the model have yet to be estimated, and so validation of a model remains future work. Measuring forces experienced by inner pipe wall during slurry flow is an important step towards determining the parameters of the model. Measuring wall forces also helps in better understanding the nature of the forces acting on the pipe. As a result, this work included design and development of a floating element assembly to measure the forces experienced by pipe wall, calibration of the sensor and testing of the unit in a slurry pipe flow loop, and analysis of the results from the floating element assembly bridge output, including the signal processing and the natural frequency determination test.

## 5.2. Recommendations for Future Work

In the oilsands flow model presented, bitumen conditioning occurs in the bottom layer and liberated bitumen from the oilsands matrix moves to the

top layer. Similarly, digested sand particles also transferred to the top layer. Since the system is in equilibrium, a mass balance must exist between the top layer and the bottom layer. In order for a mass balance to exist between the top layer and the bottom layer, counter flow (sand and water) from the top layer to the bottom layer may occur. Another possibility is that the size or concentration of the top layer increases due to the addition of bitumen and sand particles. This hypothesis must be tested in future work to improve the proposed oilsands flow model. The flow model should be extended to include flow representation of each species to replace current generic flow components.

Another recommended improvement to the oilsands flow model is the addition of separation flow component to represent a separation process downstream of flow component  $R_2$  due to bitumen conditioning and larger particles digestion. A mixing element should also be included to represent flow mixing downstream of flow component  $R_5$  and  $R_7$  between top layer mixing and liberated bitumen and digested particles from the bottom layer.

In the lumped parameter model, it should be investigated whether energy contributing to inner wall damage also create heat and cause an increase to the pipe wall temperature during this process. This hypothesis should also be investigated in future work and the lumped parameter erosion model revised if necessary.

Local velocity of the top layer can be obtained using an electrical resistivity probe as used by Gillies et al. [19]. Other advanced methods for measuring the velocity in the top layer of the pipe flow close to the wall should be explored and evaluated such as CiDRA SLURRYtrac to construct the velocity profile of slurry flow using sonar technology. Similarly, velocity of the bottom layer can be obtained.

In order to be able to predict wear due to Coulombic stress, the stress at the bottom of the pipe due to sliding of particles suspended by pipe wall has to be measured or estimated. The Coulombic stress is constant at the bottom of the pipe since the average concentration of particles suspended by pipe wall is assumed to be constant. This assumption has to be tested and validated. If valid, the equations obtained from Saskatchewan Research Council two-layer model can be used to estimate the Coulombic stress at the bottom of the pipe.

Future work should also investigate wear in the transition region between the top and the bottom layer. It can be assumed to be caused by the dominant wear mechanisms in both bottom and top layers of the slurry flow. For example, if slurry friction and mixing flow processes in top layer contribute more to overall wear rate than bottom layer friction and mixing, then top layer friction and mixing contribution is added to bottom layer bed sliding abrasion at the location of the transition region.

The floating element design should be modified to mitigate plugging with particulate material, and operating practice should include checks for fouling and a method to clear fouled material. The geometry of the wear sample can be modified to reduce the amount of sand that gets through the gap. Having tapered ends on the sides of the floating wear sample perpendicular to the slurry flow direction can reduce the rate of sand that gets through. Figure 43 shows an illustration of how the shape of the wear sample can be modified. Additionally, the affect of reducing the gap width on the measured data should be investigated. One of the concerns regarding changing the gap width is the possibility of sand getting stuck in the gap and preventing the floating element from moving. One advantage of decreasing the gap width is increasing the flush velocity at the gap. Another disadvantage of reducing the gap width is the reduced range of measurements in the shear direction.

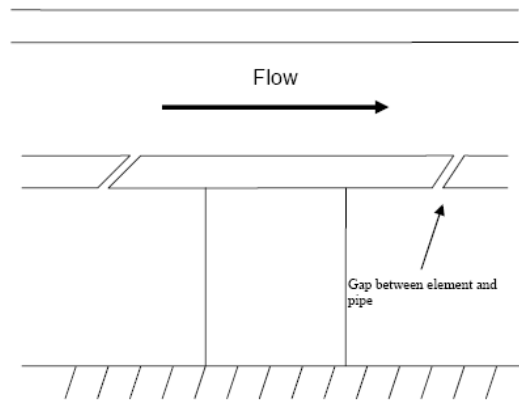


**Figure 43. Recommended floating wear sample geometry**

Currently, both of the axial and shear force measurements are performed simultaneously with the present design. The design was optimized to measure shear force while the axial force measurement was added later. One of the disadvantages of the current configurations is the cross channel interference between the axial and shear strain gauge bridges. In order to prevent cross-channel interference and optimize the axial force measurement, it is recommended that the floating element assembly be redesigned to measure the axial and shear forces separately. An additional floating element should be constructed to measure the axial forces acting on the element due to slurry flow turbulence and impacts of particles. The axial floating element can be designed with springs in the axial direction to increase its flexibility in that direction. The current assembly is only flexible in the friction direction and very stiff in the axial direction, which introduces some errors in the data collected due to reduced axial sensitivity.

Other methods to improve the design of the floating element include adding a Teflon insert around the gap of the element. The presence of the Teflon insert will eliminate the need for flush water but it will affect the

sensitivity of the measurement. Also, decreasing the length of the floating element sample will reduce the pressure drop across the element and thus increase the measurement accuracy, at the expense of measurement sensitivity. An optimal element length can be found where the pressure drop across the element is minimized while sensitivity is acceptable.

Pressure drop across the floating element is one of the sources contributing to error in the measurement [30]. In order to reduce the pressure drop across the floating element wear sample, its length can be reduced. Reducing the wear sample length reduces the bridge output sensitivity due to the reduced magnitude of forces acting.

It is also recommended that a band-stop digital filter be designed to reduce the amplitude of frequencies close to the first natural frequency (37 to 40 Hz).

A lumped-parameter corrosion wear model has to be developed to account for corrosion wear mechanisms affecting slurry pipelines. Similar to the proposed erosion wear model, the corrosion wear model has to be tested and validated. It should be noted that it is extremely difficult to isolate the contribution of corrosion since erosion-corrosion occurs simultaneously with corrosion during heterogeneous slurry flow. Similarly, a lumped parameter erosion-corrosion wear model needs to be developed for characterizing the erosion-corrosion wear mechanisms affecting slurry pipelines. The combined erosion-corrosion wear model may be somehow a combination of the erosion and corrosion lumped parameter wear models. The validity of the combined erosion-corrosion wear model has to be tested. Once validated, a complete lumped parameter wear model for slurry pipelines can be developed by combining all three individual wear models and tested in laboratory scale pipe loops.

Some considerations have been presented for measuring forces on large pipe walls, where a floating element is impractical.

A number of studies remain to be done to validate a parametric wear model for fully suspended heterogeneous slurry flow and slurry flow with moving bed in pipe, starting with studies at a reduced scale and then scale to larger systems. If an accurate wear model is developed, it would have a positive impact on estimating slurry pipeline run time length and reliability.

## BIBLIOGRAPHY

1. *Talk about oil sands* (2009). (Facts Sheet). Alberta: Government of Alberta.  
doi:April, 2009
2. Modarres, M., Kaminskiy, M., & Krivtsov, V. (1999). *Reliability engineering and risk analysis : A practical guide*. New York: Marcel Dekker.
3. *The oil sands story: The resource*. (2009). Retrieved May 04, 2009, from [http://www.oilsandsdiscovery.com/oil\\_sands\\_story/story.html/resource.html](http://www.oilsandsdiscovery.com/oil_sands_story/story.html/resource.html)
4. Schaan, J., Cook, N., & Sanders, R. S. (2007). On-line wear measurements for commercial-scale, coarse-particle slurry pipelines. *The 17th International Conference on the Hydraulic Transport of Solids*, The South African Institute of Mining and Metallurgy and the BHR Group.
5. *The oil sands story: In situ*. (2009). Retrieved May 04, 2009, from [http://www.oilsandsdiscovery.com/oil\\_sands\\_story/story.html/insitu.html](http://www.oilsandsdiscovery.com/oil_sands_story/story.html/insitu.html)
6. *The oil sands story: Mining*. (2009). Retrieved May 04, 2009, from [http://www.oilsandsdiscovery.com/oil\\_sands\\_story/story.html/mining.html](http://www.oilsandsdiscovery.com/oil_sands_story/story.html/mining.html)
7. Lipsett, M. (2008). Modeling wear damage accumulation in slurry pipeline systems. *Fifth International Conference on Condition Monitoring 2008*, Edinburgh.
8. *The oil sands story: Extraction*. (2009). Retrieved May 04, 2009, from [http://www.oilsandsdiscovery.com/oil\\_sands\\_story/story.html/extract.html](http://www.oilsandsdiscovery.com/oil_sands_story/story.html/extract.html)
9. El-Sayed, S., & Lipsett, M. (2009). A simple predictive model for slurry wear in a pipeline with bed flow. *Global Petroleum Conference*, Calgary.
10. Wilson, K. C., Addie, G. R., Sellgren, A., & Clift, R. (2006). *Slurry transport using centrifugal pumps* (3rd ed.). New York: Springer Science.
11. El-Sayed, S., & Lipsett, M. G. (2009). Monitoring wear in slurry pipelines. *Sixth International Conference on Condition Monitoring 2009*, Edinburgh.

12. Stephens, M. P. (2004). *Productivity and reliability-based maintenance management*. United States of America: Pearson Prentice Hall.
13. Dhodapkar, S., Jacob, K., Hu, S. (2006). *Fluid-Solid transport in ducts*. In a Crowe, C. T. (Eds), *Multiphase flow handbook [electronic resource]* (p.4-1 – 4-101). Boca Raton, FL: CRC.
14. Abulnaga, B.E. (2002). *Slurry systems handbook [electronic resource]*. New York: McGraw-Hill.
15. Brown, N.P. (1991). *Erosive Wear of Pipeline Systems*. In a Brown, N. P., & Heywood, N. I. (Eds.), *Slurry handling : Design of solid-liquid systems* (p. 41 – 87). London; New York: Elsevier Applied Science.
16. Gillies, R. G., Shook, C. A., & Wilson, K. C. (1991). Improved two layer model for horizontal slurry pipeline flow. *Canadian Journal of Chemical Engineering*, 69(1), 173-178.
17. Gillies, R. G., & Shook, C. A. (2000). Modelling high concentration settling slurry flows. *The Canadian Journal of Chemical Engineering*, Volume 78, 709-716.
18. Gillies, R. G., & Shook, C. A. (1994). CONCENTRATION DISTRIBUTIONS OF SAND SLURRIES IN HORIZONTAL PIPE FLOW. *Particulate Science and Technology*, , 45-69.
19. Gillies, R. G., Shook, C. A., & Xu, J. (2004). Modelling heterogeneous slurry flows at high velocities. *Canadian Journal of Chemical Engineering*, 82(5), 1060-1065
20. McKibben, M. J., Shook, C. A. (1991). *Erosive Wear of Pipeline Systems*. In a Brown, N. P., & Heywood, N. I. (Eds.), *Slurry handling : Design of solid-liquid systems* (p. 399 – 413). London; New York: Elsevier Applied Science.
21. Roco, M. C., & Addie, G. R. (1987). Erosion wear in slurry pumps and pipes. *Powder Technology*, 50(1), 35-46
22. K.C. Wilson and A. Sellgren, Interaction of particles and nearwall lift in slurry pipelines, *ASCE Journal of Hydraulic Engineering* **129** (1) (2003), pp. 73–76

23. Gupta, R., Singh, S. N., & Seshadri, V. (1995). Study on the uneven wear rate in a slurry pipeline. *Bulk Solids Handling*, 15(4), 603-607.
24. Budinski, K. G. (2007). *Guide to friction, wear and erosion testing*. West Conshohocken, PA: ASTM International.
25. Kulakowski, B.T., Gardner, J.F., Shearer, J.L. *Dynamic Modeling and Control of Engineering Systems*. Third Ed. Cambridge University Press, 2007.
26. Salama, M. M. (2000). An alternative to API 14E erosional velocity limits for sand-laden fluids. *Journal of Energy Resources Technology, Transactions of the ASME*, 122(2), 71-77.
27. Wood, R. J. K., & Jones, T. F. (2003). Investigations of sand–water induced erosive wear of AISI 304L stainless steel pipes by pilot-scale and laboratory-scale testing. *Wear*, 255(1-6), 206-218
28. Wood, R. J. K., Jones, T. F., Ganeshalingam, J., & Miles, N. J. (2004). Comparison of predicted and experimental erosion estimates in slurry ducts. *Wear*, 256(9-10), 937-947.
29. Rathakrishnan, E. (2007). *Instrumentation, measurements, and experiments in fluids*. Boca Raton, FL: CRC Press.
30. Kiewicki, J. C., Saric, W. S., Marusic, I., & Eaton, J. K. (2007). Wall bounded flows. In C. Tropea, A. Yarin & J. F. Foss (Eds.), *Springer handbook of experimental fluid mechanics* (pp. 871-902)
31. M. Lipsett, "Incorporating Damage Models in Deterministic System Models to Model Reliability in Time-Varying Systems," Sixth International Conference on Condition Monitoring 2009, Dublin, June 23 2009.
32. Jamaludin, N., & Mba, D. (2001). Monitoring low-speed rolling element bearings using acoustic emissions. *Proceeding of the 14th International Conference on Condition Monitoring and Diagnostic Engineering Management*, 37-48.

33. *Properties of distilled water*. (2010). Retrieved January/11, 2010, from [http://www.efunda.com/materials/common\\_mat/show\\_liquid.cfm?matlname=waterdistilled4c](http://www.efunda.com/materials/common_mat/show_liquid.cfm?matlname=waterdistilled4c)
34. Moss, D. R. (2004). *Pressure vessel design manual [electronic resource]: Illustrated procedures for solving major pressure vessel design problems* (3rd ed.). Amsterdam; Boston: Gulf Professional Pub.

# APPENDIX

## Kinematic Stress Sample Calculations

The kinematic stress is

$$\tau_K = 0.5\rho_f f_f V^2 + 0.5\rho_s f_s V^2$$

where

$f_f$  is the carrier fluid fanning friction factor,

$f_s$  is the solid particle friction factor (introduced by SRC),

$\rho_f$  is the carrier fluid density in  $\text{kg/m}^3 = 1014 \text{ kg/m}^3$ ,

$\rho_s$  is the solid particle density in  $\text{kg/m}^3 = 2650 \text{ kg/m}^3$ , and

$V$  is the flow velocity approximately equal to bulk velocity in fully suspended heterogeneous flow.

$$f_f = \frac{0.0625}{\left[ \log_{10} \left\{ \frac{\kappa}{3.7D} + \frac{5.74}{\text{Re}^{0.9}} \right\} \right]^2}$$

where

$\kappa$  is the roughness of the pipe wall =  $0.05 * 10^{-3} \text{ m}$ ,

$D$  is the pipe internal diameter =  $0.0525 \text{ m}$ ,

$\text{Re}$  is the pipeline Reynolds number =  $\frac{DV\rho_f}{\mu_f}$ , and

$\mu_f$  is the carrier fluid viscosity =  $10^{-3} \text{ Pa.s}$  for water at  $20 \text{ }^\circ\text{C}$ .

The solid particle friction factor is

$$f_s = 0.00033\lambda^{1.25} [0.15 + \exp(-0.1d^+)]$$

where

$$\lambda = d/L = [(C_{\max}/C)^{1/3}-1]^{-1},$$

$C_{\max}$  is the solid concentration in a settled bed which is around 0.58 to 0.63 typically used for sand,

$C$  is the volume concentration of sand in the flow = 0.214, and

$d^+$  is the dimensionless particle diameter given as:

$$d^+ = \frac{d\rho_f V \sqrt{\frac{f_f}{2}}}{\mu_f}$$

where

$d$  is the particle diameter =  $0.27 * 10^{-3}$  m

$V_{\infty}$  for 300 micron mean sand diameter

$$d_{50} = 0.3 \times 10^{-3} \text{ m}$$

$$\rho_l = 992 \frac{\text{kg}}{\text{m}^3} \text{ (Efunda.com for water at } 40 \text{ } ^\circ\text{C close to flush water temperature)}$$

$$\rho_s = 2650 \frac{\text{kg}}{\text{m}^3}$$

$$g = 9.81 \frac{\text{m}}{\text{s}^2}$$

Flush water temperature around  $40 \text{ } ^\circ\text{C}$

$$\mu = 0.653 * 10^{-3} \text{ Pa}\cdot\text{sec} \quad [33]$$

$$Ar = \frac{4dp^3 \rho_l (\rho_s - \rho_l) g}{3\mu_l^2}$$

$$Ar = 1362$$

From ChE 614 course notes,

$$a_1 = 80.9$$

$$b_1 = -0.475$$

Using  $Ar\#$ , the drag coefficient for sand of this diameter can be found based on the following equation:

$$C_d = a_1 (Ar\#)^{b_1}$$

$$C_d = 2.62$$

$$V_{\infty} = \left( \left[ \frac{4gd_{50}(\rho_s - \rho_l)}{3 * \rho_l * C_d} \right] \right)^{0.5}$$

$$= 0.05 \text{ m/s}$$

$$\text{Area of the gap around the element} = 1905 * 10^{-7} \text{ m}^2$$

$$\begin{aligned} \text{Required flow rate} &= V_{\infty} * \text{Area of gap} \\ &= 95 * 10^{-7} \text{ m}^3/\text{sec} = 10 \text{ gph} \end{aligned}$$

Since the gap around the element is non uniform and plus the water supply pressure and backpressure are not constant during test duration. It is important to apply a safety factor of 2.

Therefore, flush water supply flow rate should be around 20 gph.

## Water friction force in 2" pipe sample calculations

$$\text{Re} = \frac{\rho V D}{\mu}$$

Where,

Re = Reynolds number

$\rho$  = density

$\mu$  = dynamic viscosity

D = pipe diameter

V = flow velocity

Relative roughness =  $k/D$

Where,

k = pipe wall roughness

D = pipe diameter

$$P_f = 4f \frac{L}{D} \rho \frac{V^2}{2}$$

Where,

f = water friction factor taken from friction chart

L = pipe length

$P_f$  = pressure loss of turbulent flow in a straight section of pipe due to friction

For flow in a 2" pipe at 3 m/s we have  $Re = 2.5 * 10^5$

$$k = 0.045 \text{ mm}$$

$$\rho = 992 \text{ kg/m}^3$$

$$D = 0.055 \text{ m}$$

$$\mu = 0.653 * 10^{-3} \text{ Pa.sec}$$

f found from chart is approximately 0.0048

As a result,  $P_f = 1558.3 \text{ Pa}$  per 1 meter of pipe or  $158.3 \text{ Pa}$  for the length of the wear sample (0.102 m)

Friction force applied on the floating element due to friction is equal to the surface area of the floating wear sample = (Perimeter \* Length) of the floating wear sample \*  $P_f$

$$= (\pi D * L) * 158.3 \text{ Pa}$$

$$= (3.14 * 0.055 \text{ m} * 4 * 25.4 * 10^{-3} * 1/6)$$

$$= 0.5 \text{ N}$$

## Pipe Loop Density Calculations

Pipe dia [in]	Dia [m]	Length [m]	Volume [l]
2.067	0.0525018	2	4.33
3.068	0.0779272	49.5	236.09
4.026	0.1022604	3	24.64
Total			265.06

15.5kg average per pail of sand  
 10 pails of sand were added to the loop

kg sand	litres sand	litres water	SG	total vol	vol% sand	mass% sand
0	0.0	265.1	1.00	265.06	0.0%	0.0%
10	3.8	261.3	1.02	265.06	1.4%	3.7%
20	7.5	257.5	1.05	265.06	2.8%	7.2%
30	11.3	253.7	1.07	265.06	4.3%	10.6%
40	15.1	250.0	1.09	265.06	5.7%	13.8%
50	18.9	246.2	1.12	265.06	7.1%	16.9%
60	22.6	242.4	1.14	265.06	8.5%	19.8%
70	26.4	238.6	1.16	265.06	10.0%	22.7%
80	30.2	234.9	1.19	265.06	11.4%	25.4%
85	32.1	233.0	1.20	265.06	12.1%	26.7%
90	34.0	231.1	1.21	265.06	12.8%	28.0%
100	37.7	227.3	1.23	265.06	14.2%	30.6%
110	41.5	223.5	1.26	265.06	15.7%	33.0%
120	45.3	219.8	1.28	265.06	17.1%	35.3%
130	49.1	216.0	1.31	265.06	18.5%	37.6%
140	52.8	212.2	1.33	265.06	19.9%	39.7%
<b>150</b>	<b>56.6</b>	<b>208.5</b>	<b>1.35</b>	<b>265.06</b>	<b>21.4%</b>	<b>41.8%</b>
160	60.4	204.7	1.38	265.06	22.8%	43.9%
170	64.2	200.9	1.40	265.06	24.2%	45.8%
180	67.9	197.1	1.42	265.06	25.6%	47.7%
190	71.7	193.4	1.45	265.06	27.1%	49.6%
200	75.5	189.6	1.47	265.06	28.5%	51.3%

## Calculation of K factor for needle valve at various valve positions

$$k = \frac{(P_{\text{supply}} - P_{\text{Backpressure}})}{\text{Flow}^2}$$

Valve turns	Supply Pressure [psig]	Back Pressure [psig]	Flow [lpm]	k factor
0.25	33	0	0.61	89.3
0.5	33	0	1.08	28.2
0.75	33	0	1.25	21.2
1	33	0	1.41	16.6
2	33	0	1.64	12.3

# U.S. Silica Sand Product Data-Sheet and Particle Size Distribution

*Synonym: Size distribution*



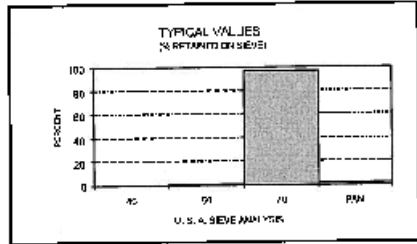
**AFS<sup>(1)</sup> 50/70**

**UNGROUND SILICA**

**PLANT: OTTAWA, ILLINOIS**

(1) AMERICAN FOUNDRYMEN'S SOCIETY

## PRODUCT DATA



USA STD SIEVE SIZE		TYPICAL VALUES		
MESH	MILLIMETERS	% RETAINED		% PASSING
		INDIVIDUAL	CUMULATIVE	CUMULATIVE
40	0.425	0.0	0.0	100.0
50	0.300	1.0	1.0	99.0
70	0.212	97.0	98.0	2.0
PAN		2.0	100.0	0.0

## TYPICAL PROPERTIES

AFS ACID DEMAND (@pH 7).....	<1	MELTING POINT (Degrees F).....	3100
AFS GRAIN FINENESS.....	50	MINERAL.....	QUARTZ
COLOR.....	WHITE	MOISTURE CONTENT (%).....	<0.05
GRAIN SHAPE.....	ROUND	pH.....	7
HARDNESS (Mohs).....	7	SPECIFIC GRAVITY.....	2.65

## TYPICAL CHEMICAL ANALYSIS, %

SiO <sub>2</sub> (Silicon Dioxide).....	99.7	MgO (Magnesium Oxide).....	<0.01
Fe <sub>2</sub> O <sub>3</sub> (Iron Oxide).....	0.020	Na <sub>2</sub> O (Sodium Oxide).....	<0.01
Al <sub>2</sub> O <sub>3</sub> (Aluminum Oxide).....	0.06	K <sub>2</sub> O (Potassium Oxide).....	<0.01
TiO <sub>2</sub> (Titanium Dioxide).....	0.01	LOI (Loss On Ignition).....	0.1
CaO (Calcium Oxide).....	<0.01		

December 16, 1997

**DISCLAIMER:** The information set forth in this Product Data Sheet represents typical properties of the product described; the information and the typical values are not specifications. U.S. Silica Company makes no representation or warranty concerning the Products, expressed or implied, by this Product Data Sheet.

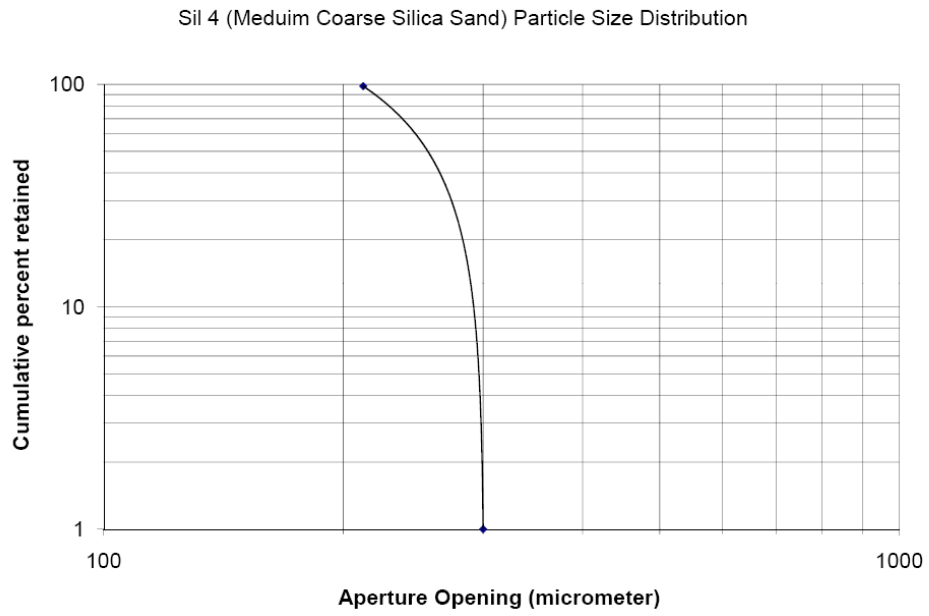
**WARNING:** The product contains crystalline silica - quartz, which can cause silicosis (an occupational lung disease) and lung cancer. For detailed information on the potential health effect of crystalline silica - quartz, see the U.S. Silica Company Material Safety Data Sheet.

U.S. Silica Company

P.O. Box 167, Berkeley Springs, WV 25411-0167

(304) 258-2500

# Particle Size Distribution



## Pressure retaining components minimum required thickness

The longitudinal stress on a shell component was calculated using the following equations [34]:

$$t = \frac{PR_i}{2SE + 0.4P}$$

where

$P$  is the design pressure,

$R_i$  is the inside radius of the shell component,

$S$  is the allowable stress level below yield point, and

$E$  is the joint efficiency.

For the outer shell,  $R_i = 88.9$  mm

$S = 15,000$  psi assumed

$E = 1$  assumed for full penetration weld

$P = 207$  psi

$t = 0.611$  mm required due to longitudinal stress

The circumferential stress on a shell component was calculated using the following equations [34]:

$$t = \frac{PR_i}{SE - 0.6P}$$

where

$P$  is the design pressure,

$R_i$  is the inside radius of the shell component,  
 $S$  is the allowable stress level below yield point, and  
 $E$  is the joint efficiency.

For the outer shell,  $R_i = 88.9$  mm

$S = 15,000$  psi assumed

$E = 1$  assumed for full penetration weld

$P = 207$  psi

$t = 0.615$  mm required due to circumferential stress

The shell thickness chosen for outer shell component is 6.35 mm which gives us a safety factor of 5 with 3.175 mm corrosion allowance.

# O-ring Seal Specifications



Software Version: 2.0.2

4/20/2009

## Customer Identification

Company:  
Contact:  
Project Name:  
Address:  
City: Zip Code:  
State:  
Telephone No.:  
Date/Time: 4-20-2009 15:16

## Ordering Specifications

Application: Industrial Static (Female)  
Compound Number: 47-071  
Size: 2-036

## Compound Information

Search Parameter:  
Material Selection Method: Fluid-Temperature  
Contained Media: Water  
Desired Temperature Range  
High: 70 °F  
Low: 70 °F

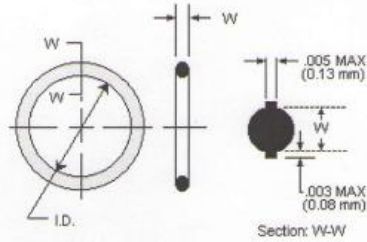
## Selected Material Information

Durometer (Shore A): 70  
Polymer: Nitrile  
Temperature  
Normal High: 180 °F  
Extended High: 180 °F  
Normal Low: -60 °F  
Color: Black  
Static Application Only: No  
Military Spec.: MIL-R-7362D Types I,II  
AMS NAS Spec.: None  
SAE/ASTM Spec.: None

## Seal Size Information

Sizing Selection Method: Known: O-ring P/N, exact gland dimensions. Calculate: Stretch, squeeze, and f  
Backup Rings: 0

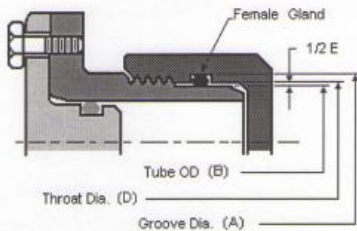
**O-Ring Diagram**



**O-Ring Dimensions**

Inside Diameter (ID):	2.364 ± 0.018 in.
Cross Section (W):	0.070 ± 0.003 in.

**Gland Diagram**

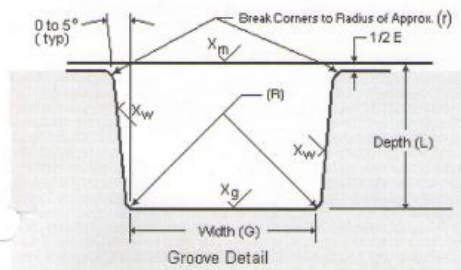


Industrial Static Gland - Female

**Gland Dimensions**

Tube OD (B):	2.375	in.
Tube OD +Tol:	0.000	in.
Tube OD -Tol:	0.003	in.
Throat Dia (D):	2.390	in.
Throat Dia +Tol:	0.002	in.
Throat Dia -Tol:	0.000	in.
Groove Dia (A):	2.490	in.
Groove Dia +Tol:	0.002	in.
Groove Dia -Tol:	0.000	in.
Diametric Clearance Max (E):	0.020	in.
Diametric Clearance Min (E):	0.015	in.

**Groove Diagram**



**Groove Dimensions**

Depth Max (L):	0.051	in.
Depth Min (L):	0.049	in.
Width Max (G):	0.087	in.
Width Min (G):	0.085	in.
Radius Max (R):	0.015	in.
Radius Min (R):	0.005	in.
Corner Radius Max (r):	0.010	in.
Corner Radius Min (r):	0.005	in.
Diametric Clearance Max (E):	0.020	in.
Diametric Clearance Min (E):	0.015	in.
Groove Surface Finish (Xg):	32	
Mating Surface Finish (Xm):	32	
Wall Surface Finish (Xw):	63	

A

**Gland/Seal Fit**

**Recommended Stretch:** 0% - 5%  
**Actual Stretch**  
**Min:** none    **Nom:** 0.5%    **Max:** 1.2%

**Recommended Squeeze:** 10% - 32%  
**Actual Squeeze**  
**Min:** 10%    **Nom:** 18%    **Max:** 21%

**Recommended Fill:** 65% - 95%  
**Actual Fill**  
**Min:** 67%    **Nom:** 79%    **Max:** 86%

**Maximum Pressure Rating:** 350 psi

**Warnings and Additional Information:**

Nominal dimensions are acceptable, but for critical usage check stretch, squeeze, and fill under worst-case tolerance conditions. (ref. table, above left)

The pressure rating is valid only to the tested limits of 160F (71C). The pressure rating does not include the effects of cylinder expansion due to pressure. One should apply a reasonable safety factor to allow for excessively sharp edges and other imperfections, as well as for higher temperatures.

**Special Considerations**

<b>Acids:</b>	No	<b>Fungus Resistant:</b>	No
<b>Auto Fuel:</b>	No	<b>High Pressure:</b>	No
<b>Contact with Plastics:</b>	No	<b>NSF:</b>	No
<b>Dynamic Applications:</b>	No	<b>Permeation:</b>	No
<b>Electrically Conductive:</b>	No	<b>Radiation:</b>	No
<b>Food (FDA):</b>	No	<b>UL:</b>	No
<b>Flex-fuels:</b>	No	<b>Vacuum:</b>	No
<b>Freon:</b>	No	<b>Water and Steam:</b>	No

**Other:**

**Customer Identification**

Company:  
Contact:  
Project Name:  
Address:  
City: Zip Code:  
State:  
Telephone No.:  
Date/Time: 4-15-2009 12:43

**Ordering Specifications**

Application: Face Seal (Internal Pressure)  
Compound Number: E0540-80  
Size: 2-041

**Compound Information**

**Search Parameter:**  
Material Selection Method: Fluid-Temperature  
Contained Media: Water  
Desired Temperature Range  
High: 122°F  
Low: 39 °F

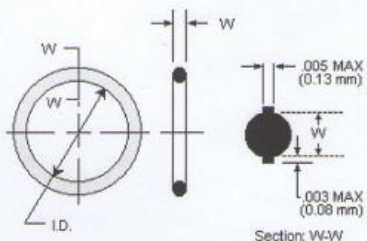
**Selected Material Information**

Durometer (Shore A): 80  
Polymer: *Nitrile*  
Temperature  
Normal High: 121 °C  
Extended High: 121 °C  
Normal Low: -57 °C  
Color: Black  
Static Application Only: No  
Military Spec.: None  
AMS NAS Spec.: None  
SAE/ASTM Spec.: None

**Seal Size Information**

Sizing Selection Method: Known: O-ring P/N. Search for: Standard gland dimensions.  
Backup Rings: 0  
Pressure: Internal

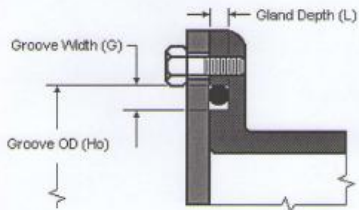
### O-Ring Diagram



### O-Ring Dimensions

Inside Diameter (ID):	2.989 ± 0.020 in.
Cross Section (W):	0.070 ± 0.003 in.

### Gland Diagram

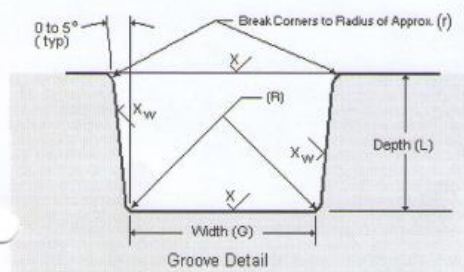


Face Seal Gland (Internal Pressure)

### Gland Dimensions

Groove OD (Ho):	3.129	in.
Groove OD + Tol:	0.000	in.
Groove OD - Tol:	0.031	in.
Groove Width Max (G):	0.107	in.
Groove Width Min (G):	0.101	in.
Gland Depth Max (L):	0.054	in.
Gland Depth Min (L):	0.050	in.

### Groove Diagram



### Groove Dimensions

Depth Max (L):	0.054	in.
Depth Min (L):	0.050	in.
Width Max (G):	0.107	in.
Width Min (G):	0.101	in.
Radius Max (R):	0.015	in.
Radius Min (R):	0.005	in.
Corner Radius Max (r):	0.010	in.
Corner Radius Min (r):	0.005	in.
Surface Finish (X):	32	
Wall Surface Finish (Xw):	32	

**Gland/Seal Fit**

Recommended Stretch: <= 0%  
 Actual Stretch  
 Min: none    Nom: none    Max: none

Recommended Squeeze: 10% - 32%  
 Actual Squeeze  
 Min: 19%    Nom: 26%    Max: 32%

Recommended Fill: 70% - 95%  
 Actual Fill  
 Min: 54%    Nom: 74%    Max: 100%

Maximum Pressure Rating: 3450 psi

**Warnings and Additional Information:**

Nominal dimensions are acceptable, but for critical usage check stretch, squeeze, and fill under worst-case tolerance conditions. (ref. table, above left)  
 A gap of 0.001 in. has been assumed for face seal mating surfaces, in the calculated pressure rating.  
 The pressure rating is valid only to the tested limits of 160F (71C). The pressure rating does not include the effects of cylinder expansion due to pressure. One should apply a reasonable safety factor to allow for excessively sharp edges and other imperfections, as well as for higher temperatures.

**Special Considerations**

Acids:	No	Fungus Resistant:	No
Auto Fuel:	No	High Pressure:	No
Contact with Plastics:	No	NSF:	No
Dynamic Applications:	No	Permeation:	No
Electrically Conductive:	No	Radiation:	No
Food (FDA):	No	UL:	No
Flex-fuels:	No	Vacuum:	No
Freon:	No	Water and Steam:	No

Other:

**Caveats:**

DANGER: FAILURE OR IMPROPER SELECTION OR IMPROPER USE OF SEALS OR RELATED ITEMS CAN CAUSE DEATH, PERSONAL INJURY AND PROPERTY DAMAGE.  
 This software provides product options for your further investigation. Before using any product, it is important that you analyze all aspects of your application and review the information concerning the product in the current product catalog. Depending on your application, further analysis and testing may be necessary before a suitable product can be selected. Parker shall not be liable for any incidental, consequential or special damages that arise from the use of any product or this software.

Note: inPHorm size calculations conform to the standard O-ring sizes per AS 568A as shown in Table B6 of the on-line REFERENCE GUIDE (Parker Catalog ORD5700).  
 The 5 dash series sizes are non-standard and have been created to special tooling specifications. The dimensions may vary due to materials with unusual shrinkage.